Experimental and Computational Studies of New Nonlinear Optical Materials

Mauro António Pereira Gonçalves

Faculdade de Ciências e Tecnologia da Universidade de Coimbra

Universidade de Coimbra

Dissertação para a obtenção do grau de

Mestre em Física

2015

Agradecimentos

Começo por agradecer a todos os que ao longo deste percurso académico me apoiaram e ajudaram permitindo o meu crescimento e formação como pessoa.

Ao Doutor Pedro Sidónio Pereira da Silva pela orientação e por todos os ensinamentos sem os quais não seria possível ter realizado este trabalho ao longo do ano.

À Professora Doutora Manuela Ramos Marques Silva, por toda a ajuda e toda a disponibilidade e pelo o incentivo constante para que todos os dias seja melhor profissional e mais organizado.

Ao Professor Doutor José António de Carvalho Paixão, pela sua disponibilidade e atenção na resolução de qualquer problema ao longo do meu percurso académico.

Quero deixar um agradecimento muito especial aos meus Pais e ao meu Irmão por tudo o que fizeram e fazem e por todos os sacrifícios por que passaram para que pudesses continuar a fazer o que gosto.

Por fim, agradeço à minha Avó por todos os ensinamentos. A ela, dedico todo este trabalho.

0. AGRADECIMENTOS

Abstract

Organic materials with nonlinear optical properties have various technological and scientific applications. This work, had as main purpose the development and structural characterization of these new substances.

Compared to dipolar molecules, the octupolar molecules proved to be substantially more advantageous for obtaining materials with high nonlinear optical response. Focusing on octopular compounds, like guanidine salts and its derivatives, and on thiocyanuric acid, some new salts were synthesized and the structural characterization was performed using the single crystal X-ray diffraction.

The salts that present noncentrosymmetric structures, were studied experimentally with the Kurtz-Perry powder method for determination of the second order susceptibility. For this materials the polarizabilities and hyperpolarizabilities of microscopic units were calculated with various computational methods (Hartree-Fock and DFT) using as starting point the geometries obtained experimentally.

It was used the oriented gas model to calculate the second-order susceptibilities from the microscopic optical properties, for crystals made of microscopic units with no special symmetry. Two different local field corrections were used in the oriented gas model. The first correction was Lorenz-Lorentz correction for spherical cavity and the other an extension of the Onsager's reaction field developed by Wortmann and Bishop. Comparing with the experimental results, the second correction describe better the nonlinear effects.

Nonlinear optical properties are intrinsically connected with the electronic distribution of each compound, so it is important to understand its behavior and the necessary conditions in order to improve the nonlinear optical response in materials and consequently their applicability.

0. ABSTRACT

The electronic density of two structures with guanidine derivatives were studied starting from the low temperature X-ray diffraction and applying a multipolar refinement. This allowed us to obtain several properties of the electronic density. This can be studied from a topological point of view, allowing us the obtention of several properties of the electronic density and of the inter and intra-molecular interactions.

Key-words: Charge density, topology, QTAIM, non-linear optics, octupolar molecules, single crystal X-ray diffraction, ab initio calculations.

Resumo

Os materiais orgânicos com propriedades de óptica não linear podem ser implementados em diversas aplicações tecnológicas e ciêntificas. Este trabalho, teve como principal objectivo o desenvolvimento e caracterização estrutural destas novas substâncias.

Quando comparadas com as moléculas dipolares, as moléculas octopolares mostram ser substancialmente mais vantajosas para a obtenção de materiais com elevada resposta de óptica não linear. Focando-nos em compostos tendencialmente octopolares, como os sais de guanidina e os seus derivados e na molécula de tiocianúrico, sintetizámos alguns novos sais dos quais fizemos a determinação estrutural recorrendo à difracção de Raios-X em cristal simples.

Os sais que apresentam estruturas cristalinas não-centrossimétricas foram estudados experimentalmente com o método de Kurtz-Perry para a determinação da susceptibilidade de segunda ordem. Para estes mesmos materiais foram estudadas as polarizabilidades e hiperpolarizabilidades das unidades microscópicas, obtidas da determinação de estrutura, através de cálculos computacionais de Hartree-Fock e de DFT.

Foi realizado um tratamento com base no modelo do gás orientado para o cálculo da susceptibilidade de segunda ordem a partir das propriedades ópticas microscópicas, para cristais feitos de unidades microscópicas sem simetria especial. Foram usadas duas correcções de campo local no modelo do gás orientado. A primeira, foi a correcção Lorenz-Lorentz para uma cavidade esférica e a segunda uma extensão do modelo do campo de reacção de Onsager desenvolvida por Wortamann e Bishop. Em comparação com os resultados experimentais, a segunda correcção apresenta uma descrição melhor dos efeitos não-lineares.

A óptica não linear está intrinsecamente ligada à distribuição electrónica de

cada composto assim, é importante perceber o seu funcionamento e quais as condições necessárias para podermos favorecer nos materiais uma maior resposta não linear e consequentemente uma maior aplicabilidade destes materiais.

A densidade electrónica das duas estruturas de derivados da guanidina, foram estudadas partindo dos resultados da difracção de Raios-X a baixa temperatura e aplicando um refinamento multipolar, o que nos permitiu obter várias propriedades da densidade electrónica. Esta pode ser estudada do ponto de vista topológico e, desta forma, podemos obter as várias propriedades da densidade electrónica e as suas interações inter e intra-moleculares.

Palavras chave: Densidade de carga, topologia, QTAIM, óptica não linear, moléculas octopolares, difracção de raios-X em cristal simples, cálculos *ab initio*.

Contents

List of Figures

LIST OF FIGURES

LIST OF FIGURES

List of Tables

Chapter 1

Introduction

The nonlinear optics is related to the interaction between an external electromagnetic field and the electric charges inside a material with generation of a new electromagnetic field with a new frequency or other physical properties. Materials with this behavior have a great importance in the development and improvement of technologies such as optical communications, optical computing, dynamic image processing and storage of data.

Within the group of materials with nonlinear optical properties three comprehensive classes of different materials can be defined. One is multilayered semiconductor structures that are composed by thin film layers, forming low dimensional systems. These layers and heterojunctions increases the quantization effect of the magnetic field and due to these quantum effects the multilayered semiconductor structures have nonlinear optical properties.

The other two classes are traditional inorganic solids and molecular based on macroscopic assemblies. The inorganic solids are used for several decades in devices and are very common on our daily life. Some examples of inorganic crystals are $LiNbO_3$, KH_2PO_4 or $BaTiO_3$, this kind of materials still presents some disadvantages because they are not easily obtained with a high quality single crystals, they are very costly and their integration in electronic devices is dificult .

The last class is the organic materials, chosen because they are most appropriated for use in NLO applications since 1980s [2]. These materials have very interesting characteristics for potential applications, such as fast response, lower

dielectric constants or best features of processability. In several cases the NLO responses are improved relatively to traditional inorganic solids and the organic materials have a large versatility in synthesis that allows the manipulation of the compounds. Usually, organic materials with second-order nonlinear properties are composed of molecules with a conjugated π-electron system between two electron donor and acceptor groups (one-dimensional charge transfer). This conformation of molecules (adopted as ideal for NLO materials) is seen in p-nitroaniline (p-NA) and 4-(N, N-dimethylamino)-4'- nitrostilbene (DANS) in Fig. 1.1 [2], for example.

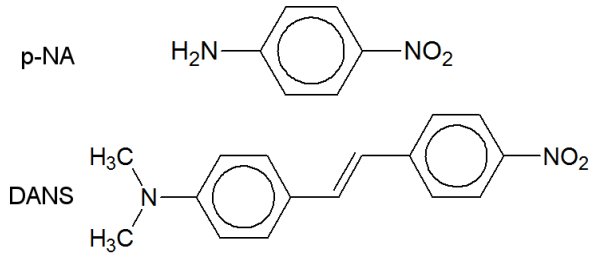

Figure 1.1: Typical molecular structures of dipolar molecules with diagram of the p-nitroaniline (p-NA) and 4-(N, N-dimethylamino)-4'- nitrostilbene (DANS)

In both molecules the nitro group acts as the acceptor, in the p-NA the amino group and in the DANS the dimethylamino group act as the donors group. The conjugated π-electron system between acceptor and donor groups in the p-NA is composed by a benzene ring and in the DANS is composed two benzene rings and the double bond.

The molecules with this conformation typically have large dipole moments associated and thus tend to crystallize in centrosymmetric space groups and to show null second-order susceptibility. However, this disadvantage characteristic of dipolar molecule can be solved by using octupolar molecules, because their three-fold rotational symmetry assure that the molecular dipole moment is canceled [3]. The advantage of these molecules is to crystallize more easily in noncentrosymmetric system. It is also verified the better ratio of off-diagonal against diagonal tensor components of the molecular hiperpolarizability leading to an better macroscopic response such as verified in the TTB (1,3,5-tricyano-2,4,6-tris(p-diethylaminostyryl) benzene) crystal [4].

The search for new chromophores start with the synthesis of the organic materials and the correspondent quantum-chemical calculations to be able to predict and understand which molecules have higher molecular hyperpolarizabilities. Therefore, the macroscopic properties of the chromophores depends not only on the molecular properties but also on their crystal packing of the new materials. Thus, it is required a thorough knowledge of the crystal structure, which can be achieved with single crystal X-ray diffraction technique. The technique used in the determination of the second harmonic generation efficiency is the Kurtz-Perry powder method. Furthermore, the experimental techniques are complemented with several theoretical calculations to predict the effects of supermolecular assemblies in the macroscope NLO response. However, the predictions of the NLO properties theoretically are extremely difficult especially in crystal structures with strong interactions between molecules or ions.

The NLO properties are intrinsically related with motion of the electrons and delocalization of the π electrons, thus the NLO studies are strongly dependent of the electronic distribution throughout the material. Therefore the knowledge of charge density distributions within the molecules and ions would help considerably the understanding of the NLO properties. Charge-density distributions can be experimentally assessed with x-ray diffraction experiments.

The X-ray scattering is dominated by interactions with electrons, thus the intensities of the scattered X-rays defines the electron distribution in a crystal. Typically the X-ray diffraction data are used to determine crystal structures from the electron distribution considering that the maxima coincide with the nuclear positions, taking into account the strong attraction of the electrons with the nuclei. This assumption demonstrates good results with the exception of the H atoms, because they have only one electron displaced towards the middle region of the chemical bond.

However the conventional methods consider electronic distribution as a sum of electron density of a spherically averaged isolated ground-state atom. So that distribution of electronic charge density allows to obtain the crystalline structure (although incorrect in neglecting interactions between atoms along the crystal). On the other hand the main objective of the X-ray charge density is the analyzes

of this interactions between atoms with a nonspherical model.

The first electron charge density distributions from the X-ray diffraction were realized in 20s and early 30s and used imprecise techniques in which it was impossible to verify the deviations of the spherical distribution of the electrons around the nucleus. Later in the 60s and 70s with the development of the new diffractometers with different geometries, the possibility of the automatic data collection and having access to great computational power, the quality of results has increased. Furthermore, the neutron diffraction has also improved providing

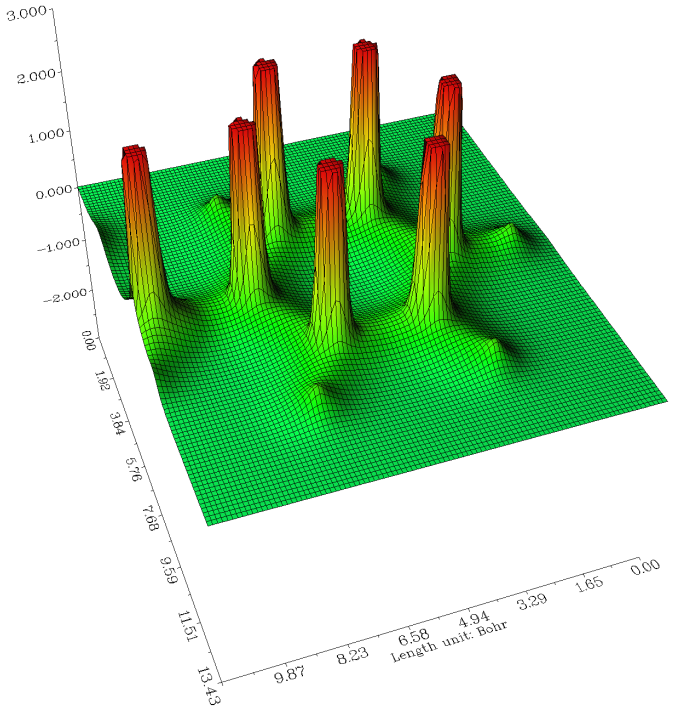

Figure 1.2: A relief map representation of the electron density in the plane of the phenyl group. Presents a set of marked maxima at the positions of the C atoms and in the N atom. Besides the H atoms has a much smaller peaks at their positions.

acurate positional and thermal parameters of atoms that can be used as a starting point in X-ray diffraction.

The various technical developments and the introduction of the deformation density allowed to obtain the first experimental electron density results that proved the overlap between atomic orbitals, lone pairs and the bending of bonds

in ring systems and in π bonding.

Nowadays, with appropriate equipment, a charge-density study can be performed from the experimental electron charge density and several properties can be discussed as deformation density, laplacian of charge density and electrostatic potential. At 1990 Bader and co-workers introduced the theory of atoms in molecules (AIM) [5], that is a powerful tool to relate the experimental and theoretical results of electron density with the chemical concepts. This analysis is founded on topological description of the electronic density concentrated in the study of the critical points and their properties, such as electron density, showed in Fig. 1.2.

Hopefully, the X-ray charge density analyses and the implementation of the AIM theory will allow the comprehension of the interactions and behavior of electrons in the molecules and crystal structures aiming the development the new materials with NLO properties.

In the sequence of this work three Posters were presented at two conferences:

Polymorphic Phases of Triphenylguanidine Derivatives: Charge-Density Studies, Mauro Gonçalves, Pedro S. Pereira Silva, Manuela Ramos Silva, JEEP2015 - Journées d'Étude des Équilibres entre Phases, 41st Conference on Phase Equilibria, 25-27 Março 2015, Universidade de Coimbra, Coimbra, Portugal.

L-histidinium thiocyanurate: Experimental and theoretical studies of a new nonlinear optical material, M. A. Pereira Gonçalves, P. S. Pereira Silva, M. Ramos Silva and J. A. Paixão, COLLOQUIUM SPECTROSCOPICUM INTERNATIONALE XXXIX, 30 de Agosto- 3 de Setembro 2015, Figueira da Foz, Portugal.

Structural and nonlinear optical studies of a salt with an octupolar chromophore: guanidinium cyclopropanecarboxylate, Pedro Sidónio Pereira Silva, M. Gonçalves, , M. Ramos Silva and J. A. Paixão, COLLOQUIUM SPECTROSCOPICUM INTERNATIONALE XXXIX, 30 de Agosto- 3 de Setembro 2015, Figueira da Foz, Portugal.

From the work presented in this thesis resulted 5 articles that are in preparation:

Structural and nonlinear optical studies of a salt with an octupolar chromophores: guanidinium cyclopropanecarboxylate, in preparation for submission to the Spectrochimica Acta Part A: Molecular and Biomolecular Spectroscopy ;

L-histidinium thiocyanurate: Experimental and theoretical studies of a new nonlinear optical material, in preparation for submission to the Spectrochimica Acta Part A: Molecular and Biomolecular Spectroscopy;

Charge-density analysis of triphenylguanidine compounds: an experimental and theoretical study of weak interactions, in preparation for submission to the Journal of Physical Chemistry A;

Two almost isostructural phenylguanidinium salts, in preparation for submission to the Journal of Chemical Crystallography;

Supramolecular structures of guanidinium carboxylates, in preparation for submission to the Journal of Molecular Structure.

Chapter 2

Nonlinear optics

2.1 Introduction

Nonlinear Optics is an important part of Optics that analyzes the processes where the response of the materials is a nonlinear function of the electromagnetic field of the light. The first experiment that showed a nonlinear response was carried out by Kerr [6] who observed that the birefringence was provoked by a static electric field in a glass. However the beginning of modern nonlinear optics is associated to the first observation of second harmonic generation performed in a quartz crystal by Franken *et al.* in 1961 [7]. This experiment was only possible after the demonstration of the first working laser by Maiman in 1960 [8].

In a optical linear regime, the polarization $\tilde{P}(t)$, is proportional to the strength $\tilde{E}(t)$ of the optical field applied:

$$\tilde{P}(t) = \epsilon_0 \chi^{(1)} \tilde{E}(t) \tag{2.1}$$

where $\chi^{(1)}$ is a constant of proportionality or linear susceptibility of the material and ϵ_0 is the permittivity of the vacuum. In Nonlinear Optics the response of the material for a more intense optical field applied can be described by an expansion of Eq. 2.1 in a power series of the strength $\tilde{E}(t)$ of the optical field applied:

$$\begin{aligned} \tilde{P}(t) &= \epsilon_0[\chi^{(1)}\tilde{E}(t) + \chi^{(2)}\tilde{E}^2(t) + \chi^{(3)}\tilde{E}^3(t) + \cdots] \\ &\equiv \tilde{P}^{(1)}(t) + \tilde{P}^{(2)}(t) + \tilde{P}^{(3)}(t) + \cdots. \end{aligned} \tag{2.2}$$

where $\chi^{(2)}$ and $\chi^{(3)}$ are know as the second and third-order nonlinear optical susceptibilities, respectively. It is necessary to take into account the tensorial nature of the susceptibilities $\chi^{(1)}$, $\chi^{(2)}$, ..., $\chi^{(n)}$ that correspond to anisotropic tensors of second, third and $n+1$ rank, respectively. In this thesis only the second-order nonlinear optical susceptibility will be studied and analyzed.

The second-order nonlinear polarization, $\tilde{P}^{(2)}(t)$ is associated to physical processes distinct from those that occur as a result of the third-order polarization $\tilde{P}^{(3)}(t)$. We should refer that the second-order nonlinear polarization can occur only in noncentrosymmetric crystals, therefore we need crystals without inversion symmetry.

Moreover, we can predict that the term $\tilde{P}^{(2)}(t)$ would be comparable to the linear response, $\tilde{P}^{(1)}(t)$, when the amplitude of the applied optical field has the same order of magnitude of the electric field strength experienced by electrons in atoms and molecules (typically of the order of $10^{10} - 10^{12} V/m$). Thus, it is expected that under conditions of nonresonant excitation the second-order nonlinear susceptibility, $\chi^{(2)}$, is of the order of $\chi^{(1)}/E_{at}$, where E_{at} is the electric field in the material. In the next section, we present brief descriptions of the nonlinear optical processes studied in the present work, namely second-harmonic generation.

2.2 Nonlinear optical processes

The nonlinear optical processes, NLO processes, are often described by Eq. 2.2 that express the nonlinear contributions to the polarization, $\tilde{P}(t)$, considering a lossless medium. The incident light in the material give rise to a time-varying polarization, dependent of the optical field strength, that can act as the source of the new components of the electromagnetic field. The wave equation in a nonlinear optical material is given by

$$\nabla^2 \tilde{E} - \frac{n^2}{c^2}\frac{\partial^2 \tilde{E}}{\partial t^2} = \frac{1}{\epsilon_0 c^2}\frac{\partial^2 \tilde{P}^{NL}}{\partial t^2} \tag{2.3}$$

where n is the linear refractive index and c is the speed of light in vacuum. This equation can be interpreted as an inhomogeneous wave equation in which

the polarization, $\tilde{P}^{NL}$, associated with the nonlinear response drives the electric field, $\tilde{E}$. The term $\frac{\partial^2 \tilde{P}^{NL}}{\partial t^2}$ is associated with the measure of the acceleration of the charges in the medium and this is consistent with Larmor's theorem of electromagnetism which states that accelerated charges generate electromagnetic radiation. The last member of Eq. 2.3 therefore acts as a source term associated with the nonlinear response of the system.

2.2.1 Second-harmonic generation

Let us consider a nonlinear material which is non-magnetic, anisotropic, non-centrosymmetric and shall we discuss a nonlinear optical interaction known as second-harmonic generation. For this it is required to analyze the interaction of an optical electric field of the form:

$$\tilde{E}(t) = E\cos\omega t = \frac{1}{2}E(e^{iwt} + e^{-iwt}) \tag{2.4}$$

where w is a frequency. In the crystal there is a static electric field, E_0, with null second-order susceptibility, $\chi^{(2)}$. Then, in the crystal the nonlinear polarization is explicitly given by:

$$\tilde{P}^{(2)}(t) = \epsilon_0\chi^{(2)}[\frac{1}{2}E^2\cos 2\omega t + 2E_0E\cos\omega t + \frac{1}{2}E^2 + E_0^2] \tag{2.5}$$

The first term in the equation oscillates at a frequency of 2ω which indicates the emission of light at that frequency and this term depends only on the presence of the optical electric field. Using the driven wave equation, Eq. 2.3, and the expression of the nonlinear polarization we can get to the generation of radiation at the second-harmonic frequency or frequency-doubling.

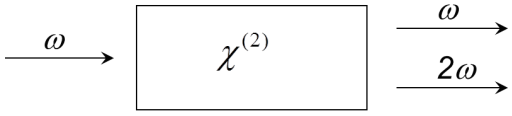

Figure 2.1: Geometry of the process of second-harmonic generation.

The second term oscillates with frequency w and is associated to the variation

of the refractive index of the crystal, this process is known as linear electro-optic-effect. Lastly, the third term correspond to a conversion of the optical electric field oscillations to a static electric field and this is called optical rectification.

These effects can be described as the mixing of electric fields of various frequencies in a nonlinear medium. So the polarization field depends of the incident fields and the effects resulting from the nonlinear susceptibilities are represented by a simplified notation dependent of the incident and resultant electric field frequencies. The second-order polarization field can be written as:

$$P_i^{(2)}(\omega_3) = \epsilon_0 \sum_{jk} \chi_{ijk}^{(2)}(-\omega_3; \omega_1, \omega_2) E_j(\omega_1) E_k(\omega_2) \tag{2.6}$$

where ω_1 and ω_2 are the frequency of the incident fields and ω_3 is the frequency of the second-order polarization field where $\omega_3 = \omega_1 + \omega_2$ and its negative sign only indicates that ω_3 is the output. The signals of the input frequencies indicate the relative phases of the two input fields. This formalism defines the effects described before in Eq. 2.5 from the nonlinear susceptibility, therefore the second-harmonic generation corresponds to $\chi_{ijk}^{(2)}(-2\omega; \omega, \omega)$, the linear electro-optic-effect is associated to $\chi_{ijk}^{(2)}(-\omega; \omega, 0)$ and the optical rectification to $\chi_{ijk}^{(2)}(0; \omega, -\omega)$.

The second-harmonic generation effect can be described by the figure below in which two photons with frequency ω are absorbed and simultaneously it is created a photon of frequency 2ω in a unique quantum-mechanical process. The solid line represents a ground state and the dashed lines represent virtual states. These levels do not correspond to the energy of eigenlevels of the free atoms but correspond to the energy levels of the atom combined with one or more photons of the radiation field.

Second-harmonic generation can be used to convert a fixed frequency laser into a different radiation with a new frequency and consequently in a different spectral region. For example, if we use the Nd: YAG laser that operates in a infrared region with a wavelength of $1064nm$ in a nonlinear material where occurs second-harmonic generation we will obtain an output radiation with $532nm$ that is a green light in the visible spectrum.

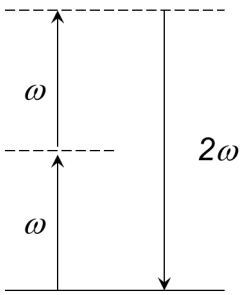

Figure 2.2: Energy-level diagram describing the process of the absorption and emission of second-harmonic generation.

2.3 Symmetries in second-order nonlinear susceptibility

In this section we analyze the most important symmetry properties of the second-order nonlinear susceptibility and use these symmetries to reduce the number of independent components of the tensor $\chi^{(2)}$.

2.3.1 Intrinsic Permutation Symmetry

Let us consider the second-order nonlinear polarization generated by two fields E_j and E_k that oscillate with frequencies ω_1 and ω_2 respectively and we obtain an output frequency ω_3 given by the Eq. 2.6. We know that the relation between the frequencies is given by

$$\omega_3 = \omega_1 + \omega_2 \tag{2.7}$$

Then the analysis of the Eq. 2.6 allows us to verify that the permutation of the order of the field amplitudes do not represent any physical change in value or sign in the ith component of the nonlinear polarization, because the indices j and k are dummy indices. We can represent this permutation with the following relation:

$$E_j(\omega_1)E_k(\omega_2) = E_k(\omega_2)E_j(\omega_1) \tag{2.8}$$

$$\chi^{(2)}_{ijk}(-\omega_3;\omega_1,\omega_2) = \chi^{(2)}_{ikj}(-\omega_3;\omega_2,\omega_1) \tag{2.9}$$

This symmetry is know as intrinsic permutation symmetry and can be applied in resonant or nonresonant systems.

2.3.2 Symmetries for lossless medium

In this section we will introduce two additional symmetries of the nonlinear susceptibility for lossless nonlinear systems. The first condition implies that all nonlinear susceptibility tensor components, $\chi^{(2)}_{ijk}$, must be real. In a lossless medium, where all frequencies applied and their sums and differences are substantially different from the resonance frequency of the material, we can see that $\chi^{(2)}_{ijk}$ is purely real.

The other condition that we present is the full permutation symmetry for which it is required that all of the frequency arguments of the nonlinear susceptibility can be freely interchanged, as long as the corresponding Cartesian indices are also interchanged simultaneously.

This permutation is applied in all frequencies of the $\chi^{(2)}$ and the corresponding Cartesian indices. In the permutations of the nonlinear susceptibility the first frequency must be equal to the sum of the other frequencies and the signs of the frequencies must be altered when the first frequency is interchanged. These rules allow to obtain the expression:

$$\chi^{(2)}_{ijk}(-\omega_3;\omega_1,\omega_2) = \chi^{(2)}_{jki}(-\omega_1;\omega_2,-\omega_3) \tag{2.10}$$

We know that to ensure that the nonlinear polarization is real the right-hand of last equation must be equal to $\chi^{(2)}_{jki}(\omega_1;-\omega_2,\omega_3)^*$, but for a lossless medium the $\chi^{(2)}$ must be real, therefore we conclude that:

$$\chi^{(2)}_{ijk}(-\omega_3;\omega_1,\omega_2) = \chi^{(2)}_{jki}(\omega_1;-\omega_2,\omega_3) \tag{2.11}$$

Similarly we can obtain:

$$\chi^{(2)}_{ijk}(-\omega_3;\omega_1,\omega_2) = \chi^{(2)}_{kij}(\omega_2;\omega_3,-\omega_1) \tag{2.12}$$

These equations for a lossless medium with $\chi^{(2)}_{ijk}$ purely real imply that the

number of photons of the high-frequency field that are created is equal to the number of photons of the low-frequency field that are annihilated. The reverse process takes place in the same way.

2.3.3 Kleinman symmetry

In nonlinear optics the interactions depend of the frequencies ω_i of the optical fields. Frequently, these frequencies are much smaller than the lowest resonance frequency of the material, ω_0, and in these conditions the second-order nonlinear susceptibility is practically independent of the applied frequencies ω_i and this allows us to use the full permutation symmetry. Therefore:

$$\chi^{(2)}_{ijk}(-\omega_3;\omega_1,\omega_2) = \chi^{(2)}_{jki}(\omega_1;-\omega_2,\omega_3) = \chi^{(2)}_{kij}(\omega_2;\omega_3,-\omega_1) = \cdots \tag{2.13}$$

Taking into account that $\chi^{(2)}$ is independent of the frequencies, we can permute the indices without permuting the frequencies, thus obtaining:

$$\chi^{(2)}_{ijk}(-\omega_3;\omega_1,\omega_2) = \chi^{(2)}_{jki}(-\omega_3;\omega_1,\omega_2) = \chi^{(2)}_{kij}(-\omega_3;\omega_1,\omega_2) = \cdots \tag{2.14}$$

So we can omit the dependence on frequencies and we obtain the Kleinman symmetry given by:

$$\chi^{(2)}_{ijk} = \chi^{(2)}_{ikj} = \chi^{(2)}_{jik} = \chi^{(2)}_{jki} = \chi^{(2)}_{kij} = \chi^{(2)}_{kji} \tag{2.15}$$

The application of Kleinman symmetry relations reduce the number of independent components of $\chi^{(2)}$ from the 27 to 10.

2.3.4 Contracted notation

In nonlinear optics it is used a notation where the frequency arguments don't appear and the susceptibility tensor is usually presented as d_{ijk}

$$d_{ijk} = \frac{1}{2}\chi^{(2)}_{ijk} \tag{2.16}$$

where the factor $\frac{1}{2}$ comes from an historical convention. Moreover, we can contract the last indices of the tensor using the intrinsic permutation symmetry. So we rewrite the indices in the following form:

$$\begin{array}{lcccccc} jk: & 11 & 22 & 33 & 23,32 & 31,13 & 12,21 \\ l: & 1 & 2 & 3 & 4 & 5 & 6 \end{array} \tag{2.17}$$

When we use this contracted notation the susceptibility tensor can be represented as a 3×6 matrix, therefore we stand with 18 components. We can use now the Kleinman symmetry condition and the contracted tensor shows new relations between the components of the form:

$$\begin{aligned} d_{12} \equiv d_{122} = d_{212} \equiv d_{26} \\ d_{14} \equiv d_{123} = d_{213} \equiv d_{25} \end{aligned} \tag{2.18}$$

In the same manner we can obtain the relations:

$$\begin{aligned} d_{13} &= d_{35} & \qquad d_{14} &= d_{36} \\ d_{15} &= d_{31} & \qquad d_{16} &= d_{21} \\ d_{23} &= d_{34} & \qquad d_{24} &= d_{32} \end{aligned} \tag{2.19}$$

After we apply the Kleinman symmetry to the matrix d_{il} we get only 10 different elements. So the matrix is given by:

$$d_{il} = \begin{pmatrix} d_{11} & d_{12} & d_{13} & d_{14} & d_{15} & d_{16} \\ d_{16} & d_{22} & d_{23} & d_{24} & d_{14} & d_{12} \\ d_{15} & d_{24} & d_{33} & d_{23} & d_{13} & d_{14} \end{pmatrix} \tag{2.20}$$

So, the use of intrinsic permutation symmetry and the Kleinman symmetry in the nonlinear susceptibility allows us to reduce the number of independent elements of the matrix d_{il} from 18 to 10 in a lossless medium.

2.3.5 Effect of inversion symmetry on the second-order susceptibility

Previously we mentioned that in crystals with inversion symmetry or centrosymmetry the nonlinear susceptibility $\chi^{(2)}$ is zero. With this argument 11 of the 32 crystal classes that have an inversion symmetry are automatically ruled out as possible materials with second-order nonlinear optical interactions. Let us demonstrate why this happens. For this we begin by considering a medium in which the response to a optical field is instantaneous. So let's consider the simplest situation with the following expression for nonlinear polarization

$$\tilde{P}(t) = \epsilon_0 \chi^{(2)} \tilde{E}^2(t) \tag{2.21}$$

and applying the optical field of the form of Eq. 2.4. Therefore if we introduce an electric field with a change of the sign, the field applied is $-\tilde{E}(t)$ and consequently the sign of the nonlinear polarization must also change, because we consider a centrosymmetric crystal. Thus we obtain the following equation:

$$-\tilde{P}(t) = \epsilon_0 \chi^{(2)} [-\tilde{E}(t)]^2 = \epsilon_0 \chi^{(2)} \tilde{E}^2(t) \tag{2.22}$$

Through the analysis of the Eq. 2.21 and Eq. 2.22, we see that $\tilde{P}(t)$ must be equal to $-\tilde{P}(t)$ and the only way to verify this condition is $\chi^{(2)} = 0$. Thus we have demonstrated that for a centrosymmetric crystal the second-order susceptibility vanishes.

2.3.6 Influence of spatial symmetry on the second-order susceptibility

In the last section we studied the nonlinear susceptibility for centrosymmetric crystals. However, there are several symmetry properties, beyond the centrosymmetry, that come from the nonlinear optical medium and can impose additional restrictions on the form of the nonlinear susceptibility tensor. This comes from Neumann's principle which says that the macroscopic physical properties of a crystal must be invariant with respect to the same symmetry operations of the

crystal. These symmetries of the nonlinear optical medium allow an important reduction in the number of nonzero independent components of the nonlinear susceptibility tensor. The derivation of the simplifications for the second-order

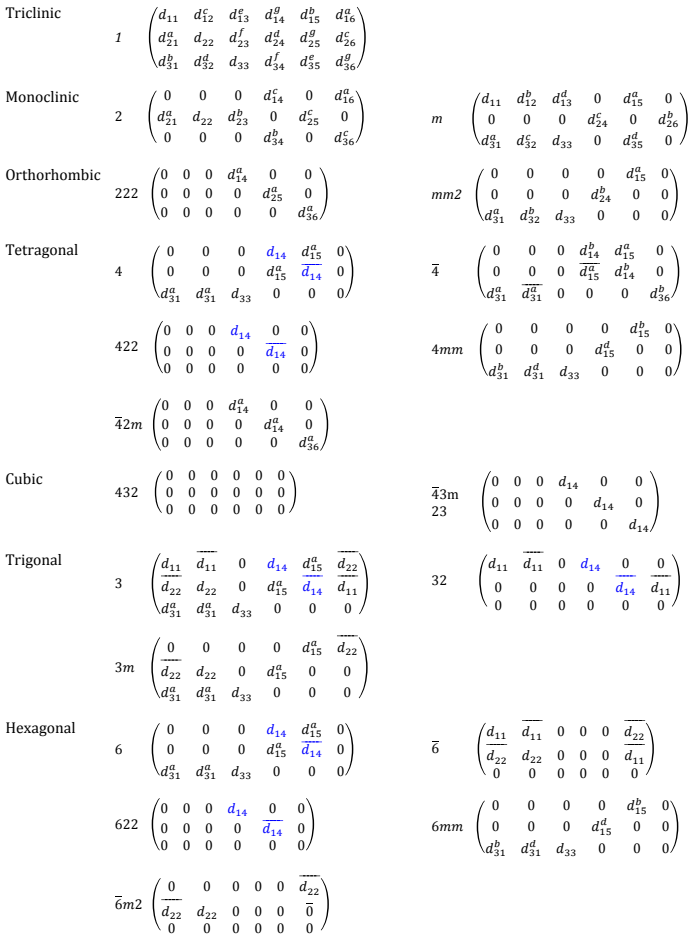

Figure 2.3: Form of the d_{il} tensor for the 21 classes without inversion symmetry. The elements with same component of the tensor d_{ij} have equal value; the bar indicates the opposite sign; blue coefficients correspond to the elements that are zero when the Kleinman symmetry condition is valid; the letters a,.., g, denotes components that are equal only if Kleinman symmetry condition is valid.

susceptibility tensor, were performed originally by Butcher in 1965 [9] and can be found in appropriate tables [10]. Later on the second-order susceptibility was describe using the contracted notation and adapted by Zernike and Midwinter in 1973 [11]. The form of the d_{il} tensor for the 21 classes without inversion symmetry

is shown in Fig. 2.3.

2.4 Molecular nonlinear optical properties

Let us focus now on the molecular side of nonlinear optics and understand how molecular structure can influence the nonlinear response. We have to consider the relation between the dipole moment of the molecule and the external optical electric field that is given by:

$$p_i = \mu_{o,i} + \epsilon_0 \alpha_{ij} E_j \tag{2.23}$$

where $\mu_{o,i}$ is the permanent dipole moment and α_{ij} is the linear polarizability tensor. In the expression above it is implicit the use of the Einstein summation convention. When the electric field applied is strong the previous expression is expanded and is no longer linear:

$$p_i = \mu_{o,i} + \epsilon_0(\alpha_{ij} E_j + \beta_{ijk} E_j E_k + \gamma_{ijkl} E_j E_k E_l + \ldots) \tag{2.24}$$

This expression defines the static molecular polarizability tensors, α, β, and γ. The tensors β and γ are, respectively, the second- and third-order polarizability or first and second hyperpolarizabilities. These are polar tensors fully symmetric in the permutation of cartesian indices.

The evaluation of the macroscopic response of the crystal must be analyzed starting from the molecular response and adding the effects of the microscopic surroundings.

We will now study the formal aspects of the molecules and ions to understand the origins of the second-order nonlinear response.

2.4.1 Effect of the structure of molecules for nonlinear response

We focus mainly on understanding the second-order polarizability, β, and how this is affected by the structure of the molecules taking into account the length

of the conjugated π electrons, the effect of the planarity of the molecules and the effect of the presence of donor/acceptor substituents.

Organic molecules are characterized by the capacity of the carbon atoms to form a large variety of stable bonds. This bonding is primarily of two types, the σ bond where the electrons are confined along the intermolecular axis. The other type is the π bond with regions of delocalized electronic charge density above and below the interatomic axis.

This way the π bonds are more susceptible to the applied external field due to the delocalization and large mobility of the electrons. Beyond the delocalization there are other factors that can improve the nonlinear response such as the inclusion of electron acceptor and donor groups in the ends of a molecule, with these groups linked by a π bridge. Usually these molecules are called "push-pull" molecules, see in Fig. 2.4. In these molecules when it is applied an external elec-

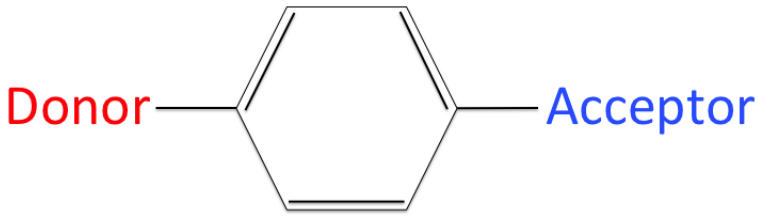

Figure 2.4: Typical organic molecule with donor and acceptor groups and electron π ring system.

tric field the π electrons flow from the donor to the acceptor group. The optical nonlinearity of push-pull molecules can be increased dramatically by adding conjugated bonds or by using strong donor and acceptor groups. But the increase in the hiperpolarizability with the increase of conjugation length inevitably leads to loss of transparency in the crystal. That is a consequence of the increase of conjugation that leads to a shift of the absorption for longer wavelengths.

The last effect that we have to analyze is the planarity of the molecules (mainly systems with two or more rings). The extent of the planarity has influence in the size of the π electron system and the mobility of the delocalized electrons. The twist angles in the molecule can be the cause of the decrease of the charge transfer contribution and consequently the decrease of the hiperpolarizability [12].

One molecular property that has a significant importance in the hiperpolar-

izability is the permanent moment of the molecule. In the "push-pull" molecules we consider a two-level system suggested by Oudar and Chemla [13], with the ground state (g) and the first excited state (e) of the molecule. The dipole moment of these molecules depend on the difference between these two levels and consequently the hiperpolarizability can be given as:

$$\beta \propto \Delta\mu_{ge}\frac{\mu_{ge}^2}{E_{ge}^2} \tag{2.25}$$

where μ_{ge} and E_{ge} are the dipole matrix element and energy transition, respectively, between the two levels previously referred and the $\Delta\mu_{ge}$ is the difference of the dipole moment of these levels.

2.4.2 Dipolar and octupolar molecules

The "push-pull" molecules have an electronic asymmetry that leads to a charge transfer and a large permanent dipole moment in the ground state which is positive for the hiperpolarizability of the molecule. However this polarity is a disadvantage because it leads to the dipole-dipole interaction between the molecules in the crystal, giving rise to centrosymmetric crystals and consequently, to a material without second-order nonlinear optical properties.

The octupolar molecules were proposed by Zyss and co-workers [3; 14; 15; 16] from the experimental evidence and based on general tensorial considerations. These are nonpolar molecules that have nonlinear optical properties, but the structure of these molecules leads to the cancelation of all vector-like observables, so does not make sense to apply the two-level model because the difference between the ground and excited state dipole moments is zero. However we can apply a model with a minimum of three states, two excited states defined as e and e' and the ground state, g.

Thus the hiperpolarizability must be proportional to the product of the transitions dipole moments of these three states. Therefore we obtain:

$$\beta \propto \frac{\mu_{ge}\mu_{ee'}\mu_{ge'}}{E_{ge}E_{ge'}} \tag{2.26}$$

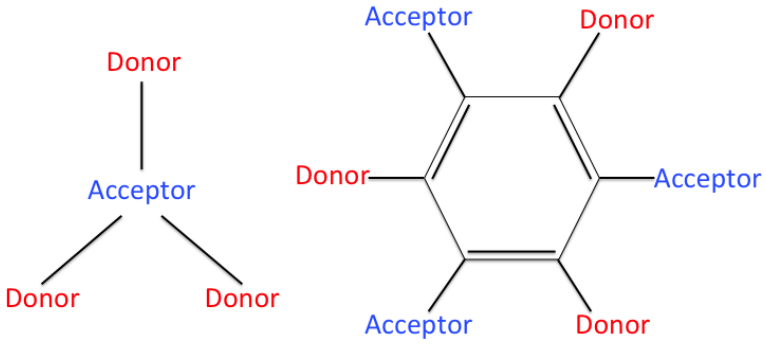

Figure 2.5: The two possible octupolar molecules that optimize the β tensor of octupolar molecules. On the left the Guanidinium route and on the right the TATB route. In these cases, the donors can be permuted with the acceptors.

The hiperpolarizability as referred previously is a fully symmetric third-rank tensor when the Kleinman symmetry is valid. So this tensor can be decomposed in a sum of the irreducible tensorial components applying the reduction spectrum equation of the tensor $T^{(n)}$:

$$T^{(n)} = \sum_{J=0,\tau_J}^{n} T_J^{(n),\tau_J} \tag{2.27}$$

where $T^{(n)}$ is a general tensor of rank n and the τ_J is the superscript that distinguishes the different linearly dependent components of rank J.

The hiperpolarizability tensor can be decomposed only in two components with $J = 1$ for the dipolar or vector part and $J = 3$ that correspond to the octupolar or septor part :

$$\beta = \beta_{J=1} \oplus \beta_{J=3}. \tag{2.28}$$

where each component has $2J+1$ independent coefficients. We can show that for molecules belonging to a multipolar symmetry group of order J, only the components of the higher orders of J remain and the others vanish due to symmetry requirements. Therefore all dipolar components with $J = 1$ vanish and only octupolar components with $J = 3$ will stay in the hiperpolarizability tensor. Then the comparison of the magnitudes of dipolar and octupolar components of the molecular quadratic hyperpolarizability is obtained with the parameter ρ given

by:

$$\rho = \frac{\|\beta_{J=3}\|}{\|\beta_{J=1}\|} \tag{2.29}$$

where $\|\beta_{J=3}\|$ and $\|\beta_{J=1}\|$ are the scalar invariants of the septor and the vector parts [3] of the β tensor.

The cancelation of dipolar moments in octupolar molecules promote the formation of noncentrosymmetric crystals contrary to what happens with dipolar molecules. Other difference between dipolar and octupolar molecules is the nonlinearity-transparency trade-off. This is due to the different selection rules for transitions in octupolar molecules. The selection rules in dipolar systems allow the transitions between ground state end low-lying states and these transitions lead to the decrease of the hiperpolarizability. But for octupolar molecules these transitions are forbidden because of the increase in the symmetry constraints for this systems.

Chapter 3

Charge density

3.1 Introduction

The knowledge of the charge density of the molecular and crystal structures is fundamental to understand all interactions and the physical and chemical macroscopic properties of the materials. The study of the charge density began with the description of the behavior of electrons in the first quantum model of the atom. In molecules we have to take into account the interactions between the atoms which will shape the distribution of electrons and for this it is required the calculation of the probability density of the electrons.

The experimental determination of the charge density was only possible after the discovery of the X-ray diffraction in 1912 [17] and the subsequent development of quantum mechanics. Shortly after in 1915, Debye stated "It seems to me that experimental study of scattered radiation, in particular from light atoms, should get more attention, since along this way it should be possible to determine the arrangement of electrons in the atoms" [18].

Let us consider a molecular system with N electrons and M nuclei. The probability of finding any of N electrons at $\mathbf{r}_1$ independently of the positions of all the other electrons is given by $\rho(\mathbf{r}_1)d\mathbf{r}_1$. In the same way we can obtain the *position electron density* defined by:

$$\rho(\mathbf{r}) = N \int \Psi_{el}(\mathbf{r}, \mathbf{r}_2, \ldots \mathbf{r}_N; \mathbf{R}) \cdot \Psi^*_{el}(\mathbf{r}, \mathbf{r}_2, \ldots \mathbf{r}_N; \mathbf{R}) d\mathbf{r}_2, \ldots d\mathbf{r}_N \tag{3.1}$$

where Ψ_{el} is the stationary wavefunction for fixed nuclear space coordinates defined by $\mathbf{R}$ that denote all M nuclear coordinates.

We have to emphasize that the charge density is given by the sum of electron and nuclear density in a point of space. But in literature "charge density" and "electron density" are often used interchangeably. Typically the term charge density is used for the cases where the determination of the distribution of both positive (nuclear) and negative (electronic) charge has taken place simultaneously, as it happens with X-ray diffraction experiments.

The electron density may be obtained either from experiment or from *ab initio* calculations.

3.2 Independent atom model

Initially, let us consider the more simple model wherein the electron density is described as a superposition of the independent spherical atomic densities. This model does not describe any deformation on the charge density. In other words the independent atom model does not describe chemical bonds or lone-pairs.

Neglecting these chemical elements of the molecule the promolecular density for the independent atom model is given by:

$$\rho_{pro}(\mathbf{r}) = \sum_i \rho_i^{at}(\mathbf{r}_i) \tag{3.2}$$

where ρ^{at} is the charge density of each isolated atom. The model only need the positional parameters of all atoms and the parameters that describe thermal motion of the atoms.

The independent atom model is a very good approximation for the heavier atoms, because for these atoms the valence electrons are a small percentage of the total electron density and consequently the core electrons must have a higher weight. On the other hand for light atoms the outer shells of electrons and their directional characteristics have an important impact on the electron density and consequently the description achieved with the independent atom model is not good. This effect is more relevant for hydrogen atoms because its whole electronic cloud is shifted towards the bonded X atom, ending up in a position much too

close to this atom, resulting in a too short X−H bond.

3.3 Aspherical density model

Previously we discussed the independent atom model where we considered an atomic spherical density that works well as a first approximation for heavy atoms. We can consider now a model based on atomic aspherical densities centered in the atomic nuclei that describe in a better way the atoms in a molecular environment.

The aspherical density model like the independent atom model, considers that the promolecular density is obtained by Eq. 3.2. The difference between these models comes from the different form used for defining each of the atomic electron densities.

$$\rho^{at}(\mathbf{r}) = \rho_{core}(r) + \rho_{valence}(r) + \rho_{deformation}(r, \theta, \phi) \tag{3.3}$$

where the first two components are the spherical core and valence densities, respectively, and the third term $\rho_{deformation}$ is the deformation of the atomic electron density that give a good approximation to describe the effect of interactions between atoms in the electron density of the molecule.

There are many refinements of the experimental electron density where it is applied the aspherical density model to obtain a more realistic description of interactions such as different types of bonds in the electron density.

3.4 Properties from the charge density distribution

The charge density distribution allows to obtain several physical properties that establish relationships between the atoms and provide important information on the crystalline environment.

These properties of the molecules or crystals are obtained using the aspherical density model or comparing the aspherical and spherical density models to analyze the interactions and their features.

3.4.1 Deformation density

Since the total density is dominated by the core electrons and only slightly affected by interactions between atoms, difference densities relative to a reference density are often used to illustrate bonding features. A commonly used function is the deformation density $\Delta\rho(\mathbf{r})$, defined as the difference between the total density $\rho(\mathbf{r})$ and the density corresponding to the independent atom model. Usually the static deformation density is given by:

$$\Delta\rho_{static}(\mathbf{r}) = \rho(\mathbf{r}) - \sum_i \rho_i^{at}(\mathbf{r}_i) \tag{3.4}$$

The deformation density shows the accumulation of density in the bonding and lone-pair regions of a molecule. Deformation density maps are widely used and an important tool in the analysis of bonds.

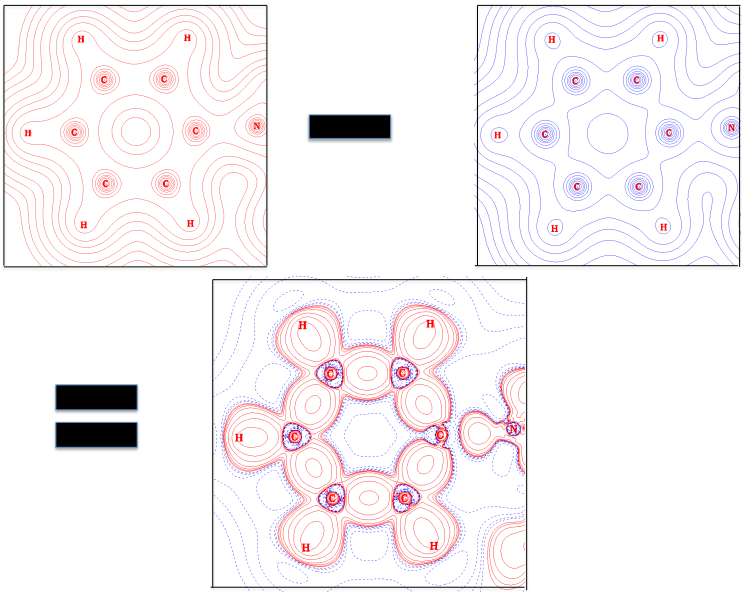

Figure 3.1: Deformation density of the phenyl group.

3.4.2 Electrostatic potential

The charge density can be seen as a distribution of the positive charges of nuclei and negative charges of the electron distribution which give rise to physical

properties such as the electrostatic potential and consequently allows to obtain the electric field and the gradient of the electric field.

The electrostatic potential at one point define the energy required to bring a positive charge from the infinite to that point, an important physical property of the molecules that allows to understand the interactions in crystals especially interactions between charge acceptors and receptors. The electrostatic potential can be defined through the Coulomb equation for the point $\mathbf{r}'$, due to a charge Q at $\mathbf{r}$ that is given by:

$$\Phi(\mathbf{r}') = \frac{Q}{4\pi\epsilon_0|\mathbf{r} - \mathbf{r}'|} \tag{3.5}$$

The factor $4\pi\epsilon_0$ is omitted when we use atomic units. The electrostatic potential between two points correspond to the work required to bring a charge from the first point to the other, so the choice of zero is arbitrary.

Thus we can divide the total charge density in positive charge distribution that is a punctual distribution that can be calculated trough the sum of the contributions of all nuclei, but the electrons leads to a continuous negative distribution of charge given by electron density, this component of potential energy is obtained from the integration over space. Therefore, the electrostatic potential is of the form:

$$\Phi(\mathbf{r}') = \sum_M \frac{Z_M}{|\mathbf{R}_M - \mathbf{r}'|} - \int \frac{\rho(\mathbf{r})}{|\mathbf{r} - \mathbf{r}'|} d\mathbf{r} \tag{3.6}$$

where Z_M is the charge of nucleus M at the point given by $\mathbf{R}_M$.

This property is an important tool to analyze the energy of the interactions. In the crystal the evaluation of the electrostatic potential allows to analyze the lattice energy.

3.5 Quantum Theory of Atoms in Molecules

Electronic charge density, $\rho(\mathbf{r})$, is a scalar field in three dimensions which has a definite value in each point of space and can be described through the quantum theory of atoms in molecules (QTAIM) developed by Professor Richard F. W. Bader and his coworkers [5].

The topological analysis of the total density, leads to a scheme of natural

partitioning of the molecular space into separate mononuclear regions identified as atoms in molecules. Within this theory, an atom in a molecule is a region in real space, containing one nucleus, bound to other atoms by surfaces, called "zero flux surfaces", defined by $\boldsymbol{\nabla}\rho = 0$. The atoms can exchange charge and momentum across this interaction surface.

The QTAIM theory leads to a completely new idea of atoms in the field of chemistry because atoms of the same element are no longer identical since they depend on the chemical environment within the molecule.

3.5.1 Topological properties of the electron density

The topology of the charge density distribution is dominated by forces between atoms in the molecules. The attractive force exerted by fixed nucleus leads to a concentration of electrons closer to the atoms. The same forces are responsible for depletion of electron density between the atoms, defining their boundaries.

The points of the charge density in which the first derivative, $\rho(\mathbf{r})$, vanishes are defined as Critical Points (CP):

$$\nabla\rho(\mathbf{r}) = \hat{i}\frac{\partial\rho}{\partial x} + \hat{j}\frac{\partial\rho}{\partial y} + \hat{k}\frac{\partial\rho}{\partial z} = \mathbf{0} \tag{3.7}$$

where $\hat{i}$, $\hat{j}$ and $\hat{k}$ are the unit vectors in cartesian coordinates. Where the zero vector indicate that each individual partial derivative in the gradient is zero and not just their sum.

Therefore from the Eq. 3.7 we find the critical points in the charge density, but cannot discriminate between a local minimum, a local maximum or a saddle point. In order to make this distinction we must use the second derivatives, $\nabla\nabla\rho$, in the critical point with coordinates $\mathbf{r}_c$. The nine second derivatives of $\rho(\mathbf{r})$ can be organized in a so-called Hessian matrix:

$$\mathbf{H}(\mathbf{r}_c) = \begin{pmatrix} \frac{\partial^2\rho}{\partial x^2} & \frac{\partial^2\rho}{\partial x\partial y} & \frac{\partial^2\rho}{\partial x\partial z} \\ \frac{\partial^2\rho}{\partial y\partial x} & \frac{\partial^2\rho}{\partial y^2} & \frac{\partial^2\rho}{\partial y\partial z} \\ \frac{\partial^2\rho}{\partial z\partial x} & \frac{\partial^2\rho}{\partial z\partial y} & \frac{\partial^2\rho}{\partial z^2} \end{pmatrix}_{\mathbf{r}=\mathbf{r}_c} \tag{3.8}$$

The Hessian matrix is obtained from the charge density and can be diagonal-

ized since it is real and symmetric. This operation of diagonalization is equivalent to a rotation of the coordinate system and the new axes are x', y', z' that are also the principal curvature axes of the critical point. To obtain the diagonalized Hessian matrix we must apply the three eigenvalue equations $\mathbf{H}\mathbf{u}_i = \lambda_i \mathbf{u}_i$ where $\mathbf{u}_i$ is the ith column vector. Then the diagonalized Hessian matrix is given by:

$$\mathbf{\Lambda} = \begin{pmatrix} \frac{\partial^2 \rho}{\partial x'^2} & 0 & 0 \\ 0 & \frac{\partial^2 \rho}{\partial y'^2} & 0 \\ 0 & 0 & \frac{\partial^2 \rho}{\partial z'^2} \end{pmatrix}_{\mathbf{r}'=\mathbf{r}_c} = \begin{pmatrix} \lambda_1 & 0 & 0 \\ 0 & \lambda_2 & 0 \\ 0 & 0 & \lambda_3 \end{pmatrix} \tag{3.9}$$

where λ_1, λ_2 and λ_3 correspond to the principal curvatures of the charge density in the critical point.

The critical points are found in charge density distribution with the Eq. 3.7 and they are distinguished using the Hessian matrix. The critical point are classified according to their rank (ω) and signature (σ), therefore each type of critical point is symbolized by (ω, σ).

The rank is the number of non-zero curvatures of the charge density in the critical point. If we consider a rank less than three, $\omega < 3$, we will verify that the critical point is mathematically unstable and will vanish or bifurcate under small perturbations with the motion of the atoms in the structure. Thus we can conclude that the rank of critical points in the charge density is usually $\omega = 3$.

The signature is the algebraic sum of the signs of the curvatures, so each of the curvatures contributes with ± 1 depending on whether it is a positive or negative curvature. There are four different types of critical points classified by their rank and signature, each type corresponding to an element of chemical structure like (nuclear critical point, bond critical point, ring critical point or cage critical point).

The critical points $(3, -3)$ are local maxima in ρ, thus corresponding to atoms in the charge density. For a bond critical point or saddle point the charge density is found between all pairs of atoms which are considered linked by a chemical bond and has a maximum in the plane defined by the corresponding eigenvectors but is a minimum along an axis perpendicular to this plane. In the ring critical points the density have a local minimum in the plane of the ring and is a maximum in the

Table 3.1: Types of critical points, (ω, σ), with the topological description and their chemical structural meaning in the molecule.

CP type	Curvatures of ρ	Chemical entity
$(3, -3)$	Local maximum of ρ	Nuclear critical point (NCP)
$(3, -1)$	Local maximum of ρ in a plane and a minimum along the third axis	Bond critical point (BCP)
$(3, +1)$	Local minimum of ρ in a plane and a maximum along the third axis	Ring critical point (RCP)
$(3, +3)$	Local minimum of ρ	Cage critical point (CCP)

axis perpendicular to the ring plane. Lastly the cage critical point is a minimum in the charge density, therefore in these critical points there is a depletion of charge.

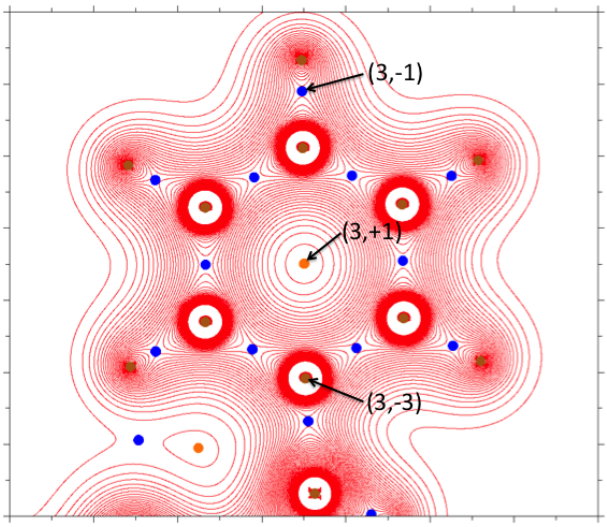

Figure 3.2: Critical points in the electron density of the phenyl group.

The number and type of critical points that can coexist in a molecule or crystal depend of the following topological relationship:

$$n_{NCP} - n_{BCP} + n_{RCP} - n_{CCP} = \begin{cases} 1 & \text{Isolated molecules} \\ 0 & \text{Infinite crystals} \end{cases} \tag{3.10}$$

where n is the number of critical points of each type. The first equation is applied in finite systems like molecules and is known as Poincaré-Hopf theorem and the

second equation is for infinite and periodic systems like crystals and is called the Morse equation. The violation of these relations implies that the set of critical points determined is not complete. On the other hand Eq. 3.10 cannot be used to prove that the analysis of the system is correct because it is easy to obtain an apparently correct result due to a cancelation of errors.

3.5.2 Atoms in molecules from the gradient vector field of the charge density

The pronounced maxima in the electron density at the positions of the nuclei give rise to a natural partitioning of the molecular space into separate mononuclear regions, Ω, that can be identified as atoms in molecules. The surface that bounds an atom in a molecule is characterized as a zero flux surface in a gradient vector field of the electron density. So mathematically we can define this surface with the following equation:

$$\nabla\rho(\mathbf{r}) \cdot \mathbf{n}(\mathbf{r}) = 0 \tag{3.11}$$

where $\mathbf{r}$ is the position vector and $\mathbf{n}$ is the unit vector normal to the surface, $S(\Omega)$. This surface of zero flux is not crossed by any line of the gradient vectors at any point and the volume inside the surface is known as atomic basin. Gradient vector field lines belonging to an atomic basin converge all to one nucleus that acts as an attractor to these gradient vector field lines. So, these gradient vector field lines sweep a portion of space associated with one nucleus that is identified as the basin of an atom in a molecule.

The topological definition of an atom results from the boundary condition expressed in Eq. 3.11 and which applies to every point on the surface. This real space partitioning of the electron density has been shown to be based in quantum mechanics bringing into coincidence the topological definition of an atom in a molecule with that of a proper open quantum system.

3.5.3 The bond paths and the molecular graphs

The zero flux surfaces between bonded atoms in a molecule have an important topological element associated called “bond path” that is a single line of locally

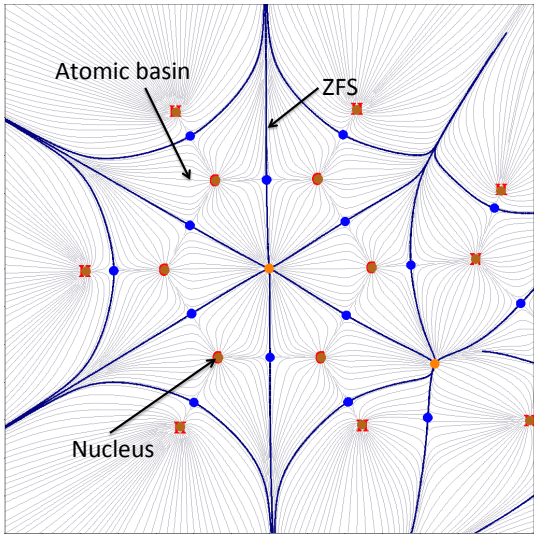

Figure 3.3: The gradient of the electron density with the respective critical points and surface of zero flux in the phenyl group.

maximum density linking two nucleus. The bond path is an indicator of chemical bonding for all types of interactions such as weak, strong, closed-shell and open shell. The point on the bond path with minimum electron density is the bond critical point (BCP) and it is also the point where the bond path intersects the zero-flux surface between the two bonded atoms.

The set of all bond paths that link the nuclei of bonded atoms in an equilibrium geometry, including the associated critical points, is known as the molecular graph. In a optimized geometry the molecular graph gives a unique definition of the molecular structure that can thus be used to locate structural changes along a reaction path.

3.5.4 Laplacian of electron density

One important function of the electron density is the Laplacian, given by

$$\nabla^2\rho(\mathbf{r}) = \frac{\partial^2\rho}{\partial x'^2} + \frac{\partial^2\rho}{\partial y'^2} + \frac{\partial^2\rho}{\partial z'^2} = \lambda_1 + \lambda_2 + \lambda_3 \tag{3.12}$$

The Laplacian is equal to the trace of the Hessian and is invariant under a rotation of the coordinate system.

The Laplacian of the electron density, $\nabla^2\rho(\mathbf{r})$, indicates the regions of concentration or depletion of electronic charge. So, when $\nabla^2\rho(\mathbf{r}) > 0$ the electron density is locally depleted and expanded relative to its average distribution, but if $\nabla^2\rho(\mathbf{r}) < 0$ the density is locally concentrated and is compressed relative to its average.

For an isolated atom the Laplacian reproduces the spherical shell structure in terms of alternating shells of charge concentration followed by shells of charge depletion. The spherical nodes in the Laplacian are envelopes surrounding regions of density depletion or concentration. The outer shell of charge concentration, which is followed by a shell of charge depletion that extends to infinity, is called the valence shell charge concentration (VSCC). This is valid for an isolated atom but in a molecule or crystal, where the atom is involved in bonding, the spherical symmetry of the VSCC is broken.

The Laplacian is a fundamental tool for finding and characterizing regions of charge concentration or depletion and, since it is a second-derivative function, is very sensitive to subtle changes in the charge density.

3.5.5 The atomic partitioning of molecular properties

Previously, we defined the topological partitioning of the molecules into atomic basins and this concept is essential for the development of the quantum mechanics of open system. The atomic basin is a volume defined by a zero-flux surface and this surface is a necessary constraint for the application of Schwinger's principle of stationary action for each atomic basin.

The partitioning of the molecular space into atomic basins allows the consistent partitioning of electronic properties into atomic contributions. Then the properties of the molecules are given by the sum of the electronic properties of each atomic basin. Therefore, the expectation value of a quantum operator averaged over all space is given by the sum of the expectation values of the operator

over all atom basins of the molecule:

$$\begin{aligned}\langle \hat{O} \rangle = \sum_{i}^{\text{all atoms}} \left(N \int_{\Omega_i} \left\{ \int \frac{1}{2} [\Psi^* \hat{O} \Psi + (\hat{O}\Psi)^* \Psi] d\tau' \right\} d\mathbf{r} \right) \\ = \sum_{i}^{\text{all atoms}} \left(\int_{\Omega_i} \rho_O d\mathbf{r} \right) = \sum_{i}^{\text{all atoms}} O(\Omega_i)\end{aligned} \tag{3.13}$$

where $\langle \hat{O} \rangle$ is the molecular expectation value of the operator $\hat{O}$, the integration $\int d\tau'$ correspond to the integration over all electrons less one and the summation over all spins, and $O(\Omega_i)$ is the average of this operator over an atomic basin Ω_i, and where the sum are performed over all the atoms in the molecule or crystal.

The Eq. 3.13 implies that any property O that can be expressed in terms of a corresponding property density in space $\rho_O(\mathbf{r})$ can be written as a sum of atomic contributions obtained by averaging the appropriate operator over the volume of the atom, so that property has atomic additivity.

3.5.6 Bond properties

A zero-flux surface is defined by a particular set of $\nabla\rho(\mathbf{r})$ trajectories that terminate at a single point, the bond critical point, where $\nabla\rho(\mathbf{r}) = 0$. There is one BCP between each pair of bonded atoms, that are defined topologically as atoms linked by a bond path and that share a common interatomic zero-flux surface. Besides the set of trajectories which terminate at the BCP and define an interatomic surface, a pair of trajectories originates at the BCP and terminate at the nuclei of the chemically bonded atoms thus defining the bond path between the two atoms. Chemical bonding interactions are characterized and classified according to the properties of the electron and energy densities at the BCP, that are called collectively "bond properties" [5; 19; 20]

3.5.6.1 Electron density at the bond critical point

The amount of electron density at the bond critical point, $\rho(\mathbf{r}_{BCP}) = \rho_{bcp}$, defines the strength of the chemical bond which consequently defines the bond order.

$$\text{Bond Order} = exp[A(\rho_{bcp} - B)] \tag{3.14}$$

where A and B are constants that only depend of the nature of the two bonded atoms. Generally, ρ_{bcp} is larger than 0.20 au in covalent bonds and less than 0.10 au in closed-shell interactions like ionic and van der Waals bonding.

3.5.6.2 The bonded radius of an atom

The "bonded radius" of an atom A relative to a bond critical point of an interaction is the distance between the nucleus of atom A and the BCP and is designated as $r_{BCP}(A)$. The sum of the two associated bond radii of the same bond path is known as bond path length. If the bond path is coincident with the internuclear axis the bond path length is equal to the bond length. But when bond paths are curved the bond path length will exceed the bond length. This situation is found frequently in hydrogen-bonded interactions or in cyclic molecules as in rings.

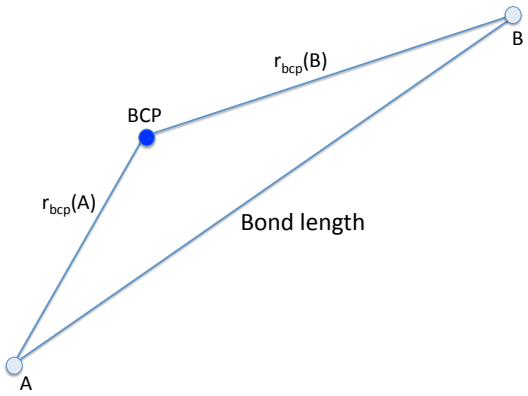

Figure 3.4: Scheme that relates the bond path and distances of atoms A and B to BCP with the bond length.

3.5.6.3 The Laplacian of the electron density at the bond critical point

The Laplacian of the electron density at the BCP is the sum of the three curvatures of the density in the critical point (see Eq. 3.12). The two curvatures perpendicular to the bond path, λ_1 and λ_2, are negative and by convention $|\lambda_1| > |\lambda_2|$. The third curvature, λ_3, is along the bond path and is positive. The negative curvatures measure to what extent the density is concentrated along the bond path and the positive curvature measures the depletion in the region of the interatomic surface and the concentration in the individual atomic basins.

In covalent bonds the two negative curvatures are dominant and $\nabla^2\rho_{bcp} < 0$. On the other hand, in close-shell interactions, like ionic, hydrogen-bonding or van der Walls interactions, the fundamental characteristic is the depletion of the electron density in the critical point and $\nabla^2\rho_{bcp} > 0$.

Lastly, in strong polar bonds there is a significant accumulation of the electron density between the nuclei, as happens in all shared interactions, but it's not possible to use the sign of the Laplacian to distinguish this type of bond since it can have either sign.

3.5.6.4 The bond ellipticity

The ellipticity is an important quantity in the analysis of bonds and it measures the amount of electron density accumulated in the plane that contains the bond path. The ellipticity is given by:

$$\varepsilon = \frac{\lambda_1}{\lambda_2} - 1 \tag{3.15}$$

From the analysis of this expression we can easily see that when $\lambda_1 = \lambda_2$ the ellipticity is zero and for this case the bond is cylindrically symmetrical. The ellipticity is a measure of the π-character of the bonding up to the limit of the "double bond" in which case the ellipticity reaches a maximum. Going from a double to a triple bond, the tendency is reversed and the ellipticity decreases with the increase of the bond order, because at the limit of "triple bond" the bonding regains its cylindrical symmetry (two π-bonding interactions in two orthogonal planes and one cylindrically symmetric σ-bonding interaction). The ellipticity

of an aromatic bond is around 0.23 in benzene and for a formal double bond is approximately 0.45 in ethylene.

Chapter 4

Experimental methods

4.1 Introduction

In this thesis a detailed structural analysis of the new compounds synthesized, using the single crystal X-ray diffraction technique, was performed in order to obtain the molecular structure of the compounds. Moreover in the specific case of noncentrosymmetric crystal structures, beyond the structural analysis, the nonlinear optical properties were also studied for each new compound.

For this reason in this chapter we describe some experimental methods such as X-ray diffraction and the Kurtz and Perry technique.

4.2 Synthesis and crystal growth

4.2.1 Synthesis

In this thesis several new salts were synthesized by acid-base reactions. Several solvents were used like water (for most acids, for L-histidine and for guanidinium carbonate and phenylguanidinium carbonate), ethanol (for triphenylguanidine) and acetone (for thiocyanuric acid) and the reactions were performed under ambient conditions of temperature and pressure.

4.2.2 Crystal growth

The quality of the crystals used in diffraction experiments is very important to determine structures with quality. The effects of a low quality crystal will affect the quality of the final structure. The single crystals used in data collections usually have dimensions of $0.1 - 0.4$ mm. To obtain single crystals with good quality they should grow slowly, taking from hours to months, depending on the material. In this thesis the crystals were grown by slow evaporation of the solutions.

4.3 Single-crystal X-ray crystallography

The single-crystal X-ray diffraction is the more common technique used to determine the molecular structure of the crystals at the atomic level. The X-ray diffraction was first performed in 1912 by W. H. and W. L. Bragg and it has been used to determine the structure of conventional small molecules with extraordinary success in the last 100 years.

In a crystal structure the X-rays are scattered by the electrons of the atoms, and for this reason it is possible to determine the electron-density distribution, averaged over time and over the vibrations of the atoms. As the crystal structure is periodic, it is only needed to determine the constitution of one unit cell and the existence of other symmetries besides pure translation reduces this even more, to the asymmetric unit of the crystal structure, which is a fraction of the unit cell for all cases except for the space group $P1$.

Within a unit cell, each atom is a source of scattered X-rays and the waves sum in a constructive or destructive way depending on the direction of the diffracted beam and on the atomic positions.

The geometrical conditions under which a diffracted beam is observed is given by Bragg's law:

$$n\lambda = 2d_{hkl}\sin\theta \tag{4.1}$$

where λ is the wavelength of the X-ray, θ is the Bragg's angle and d_{hkl} is the interplanar distance between planes of a family of planes. These geometrical conditions determine that there is constructive interference when the path difference

is a whole number of wavelengths.

The diffraction pattern obtained is the Fourier transform of the crystal structure and the mathematical relationship for this is given by:

$$F(hkl) = \sum_{j=1}^{N} f_j \exp[2\pi i(hx_j + ky_j + lz_j)] \tag{4.2}$$

where f_j is the atomic scattering factor for the jth atom of the unit cell with coordinates x_j, y_j and z_j and $F(hkl)$ is the structure factor for one particular reflection defined by the Miller indices h,k and l.

This structure factor can be expressed as a diffracted beam with an amplitude, $|F(hkl)|$, and its relative phase, $\phi(hkl)$. Thus, the structure factor also can expressed as:

$$F(hkl) = |F(hkl)| \exp[i\phi(hkl)] \tag{4.3}$$

The intensity is proportional to $|F(hkl)|^2$ and the experimental measurements allow the determination, after application of the correction factors, of the quantities h, k, l, $|F(hkl)|$.

From the X-ray diffraction pattern the electron density at every point of the unit cell can be obtained. The electron density is expressed through the structure factor by:

$$\rho(xyz) = \frac{1}{V} \sum_{hkl} F(hkl) \exp[-2\pi i(hx + ky + lz)] \tag{4.4}$$

where V is the volume of the unit cell and the summation is over all structure factors measured. This expression allows to obtain the electron density of a single unit cell from the X-ray diffraction performed over the entire crystal, therefore the electron density of the unit cell obtained correspond to an average over the whole crystal.

There is a phase problem associated with the complete determination of the structure factors since the measured X-ray intensities give only the amplitudes of the structure factors but not their phases. The determination of the electron density cannot be performed directly from the experimental measurements and the phases must be obtained by other processes. The most common way of solving this problem is using methods, so-called direct, that attempt to derive

the structure factor phases from the X-ray intensities by using mathematical relations.

The direct methods are only possible because the structure factor amplitudes and phases are dependent and are linked by the knowledge of the electron density. This way, if the amplitudes are known, the phases can be calculated according to the information of electron density and vice versa. Therefore, the mathematical constraints on the electron density function will impose corresponding constraints on the structure factors. Since the amplitudes of the structure factors are known, most constraints restrict the values of structure factor phases and are sufficient to determine the phase values directly in most of the cases.

In this thesis all the structures were solved through these direct methods implemented in the SHELXS-97 program [21] and refined on F^2s by full-matrix least-squares with SHELXL-97 program [21].

The new compounds in this thesis were determined through the X-ray diffraction experiments performed with the four circle diffractometer with κ geometry Bruker-Nonius Kappa Apex II. The radiation used in diffractometer APEX II is Mo Kα with a wavelength $\lambda = 0.71073$ Å and the detection is made with a Charge-Coupled Device (CCD) with 4096×4096 pixels, each pixel with a dimension 15μm$\times 15\mu$m.

The low temperature X-ray diffraction data used in this thesis was obtained in diffraction experiments using a dual flow nitrogen and helium cooler, the N-HeliX from Oxford Cryosystems, which allows to perform diffraction experiments with the APEX II diffractometer at temperatures between 28-300K.

4.4 Experimental methods for NLO

4.4.1 Kurtz and Perry powder method

Kurtz and Perry devised an experimental technique which allows a fast and efficient way of testing candidate NLO materials [22]. This method requires that the nonlinear optical material is a powder, which is usually easy to obtain. The Kurtz and Perry powder method can give some qualitative measure of the second-harmonic efficiency to check if a material can be useful for nonlinear optics [23].

Now we will describe the experimental set-up used to perform measurements by Kurtz and Perry method. The crystalline powder material is placed in a sample holder and it is irradiated by an high-power pulsed laser beam with a wavelength of 1064 nm that is expanded before reaching the sample.

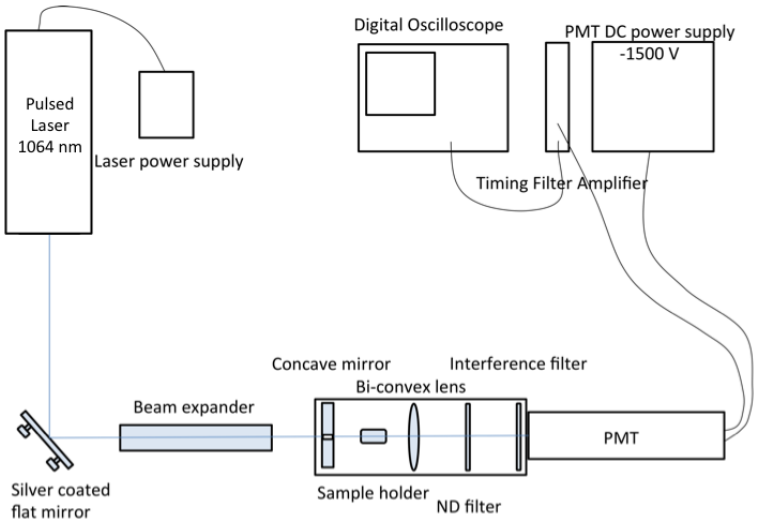

Figure 4.1: Experimental set-up for Second-harmonic generation measurements with the Kurtz and Perry powder method

In the sample the intensity of the second-harmonic, $I^{2\omega}$, generated in all directions, is limited only by the sample holder geometry, then this SHG light coming from the sample is focused on a concave mirror that collimate this light. The collimated beam is focused on the photomultiplier (PMT) by a bi-convex lens. The light go through a Neutral Density filter (ND) that reduces the intensity

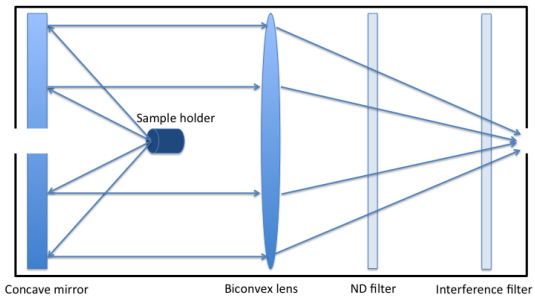

Figure 4.2: Optics paths in the set-up after the beam expander.

of SHG light hitting the photomultiplier. Before the photomultiplier there is an

interference filter that only allows the passage of light with a wavelength around the intended wavelength of the SHG light. The photomultiplier voltage and previous filters are optimized to get a good signal-to-noise relation and avoid the saturation of the photomultiplier. This voltage is measured with a digital oscilloscope which is triggered by the signal itself. The signals are exported to a computer and integrated with a script written with the software Mathematica® version 8.0. The result of the integral of the signal is proportional to the SHG intensity generated by the tested material, but the real result of SHG efficiency is obtained by comparison with a signal generated by a reference material, that in this thesis will be urea, under the same experimental conditions.

In this thesis all measurements were performed with a fundamental wavelength of 1064 nm and the laser pulses were produced by a Nd:YAG laser at low power, 11 mJ per pulse, with a duration of 10 ns and a frequency of 10 Hz.

Chapter 5

Multipole Refinement

5.1 Introduction

The electron density, ρ, was obtained from X-ray diffraction experiments performed at low temperatures which was discussed earlier. Usually, the structures obtained from X-ray diffraction experiments are solved applying the independent atom model, where the electron density of a crystal is given by a sum of the isolated atomic densities. As discussed above, this model is a good approximation for the heavier atoms because most of their electrons are in the core of the atom. On the other hand, for the lighter atoms, we cannot consider a spherical electron density because this is not a good description of these atoms in a crystal.

It should be noted that an important assumption of the IAM model is that the atoms in a crystal are neutral, which contradicts the fact that molecules have dipole and higher electrostatic moments. In part, the dipole moments arise from the nonspherical distribution of the atomic densities but a large part is due to the charge transfer between atoms of different electronegativity in a molecule. A better description of atoms in crystal is obtained using an aspherical model that allows a good description of all atoms, with the exception of hydrogen atoms, so the application of this model provide a more complex electron density.

A commonly applied model for an aspherical description of electron density is the atom-centered finite multipole expansion, initially developed by Stewart [24] and later changed by Hansen and Coppens [25]. The multipole model has emerged

as one of the most popular models of aspherical atom refinement, which considered functions that resemble atomic orbitals to describe the electron density, so this model consider that atomic orbitals are an appropriate description of the electron density in the crystal.

The description of an atom using this formalism is given by three components in the following form:

$$\rho_{at} = \rho_c(r) + \rho_v(\kappa r) + \rho_d(\kappa' \mathbf{r}) \tag{5.1}$$

where $\rho_c(r)$ and $\rho_v(r)$ are the spherical core and valence densities, respectively, and $\rho_d(\mathbf{r})$ is the aspherical deformation density, κ and κ' are the expansion and contraction parameters associated to spherical valence density and aspherical deformation density.

Let us now understand how to describe the electron density and introduce several improvements in the interactions between atoms in a crystal.

5.2 Improvement of scattering models

5.2.1 Kappa formalism

The first improvement is a simple modification in the IAM that allows a charge transfer between atoms. The scattering of the valence electrons are separated from that of the core shell, what makes possible to adjust the valence population and the radial extension of the valence shell. In addiction to the conventional parameters of the structure analysis, it is introduced the valence shell population parameter, P_v, that is dependent of the number of electrons in the valence shell, and κ, a variable that control the expansion or contraction of the valence shell. In the κ-formalism, the atomic electron density is given by:

$$\rho_{at} = \rho_c + \rho'_v(\kappa r) = \rho_c + P_v \kappa^3 \rho_v(\kappa r) \tag{5.2}$$

The scale parameter, which is used to constrain the radial coordinate, is the κ variable. So, $\rho_v(\kappa r)$ is shaped in such manner that for $\kappa > 1$ the density is contracted and for $\kappa < 1$ the valence density is expanded. The κ^3 factor, in

equation 5.2, is a normalization factor that satisfies the condition:

$$N4\pi \int \rho_v(\kappa r) r^2 dr = 1 \tag{5.3}$$

From the new density form with κ factor, the structure factor can be rewritten, dividing this in two components. The component correspondent to the scattering factor of valence is affected by κ this way:

$$f'_v(S) = f_v(S/\kappa) \tag{5.4}$$

The structure factor is given by:

$$F(\mathbf{H}) = \sum_j [\{P_{j,c} f_{j,c}(H) + P_{j,v} f_{j,v}(H/\kappa)\} exp(2\pi i \mathbf{H} \cdot \mathbf{r}_j) T_j(\mathbf{H})] \tag{5.5}$$

where $P_{j,c}$ and $P_{j,v}$ are the core and valence electron populations associated to the respective scattering factors.

The kappa formalism allows to verify that the valence shell of the more positive atoms are contracted and this is justified by the decrease of the electron-electron repulsion.

5.2.2 The multipole description of the charge density

The most successful model based on atom-centered multipolar functions, is that in which the electron density contains aspherical density functions. Later, it was used spherical harmonic density functions centered on each of the atomic nuclei, in a generalized X-ray scattering formalism.

There are several atom-centered multipole models available. We can distinguish between valence-density models, where the density functions represent all valence electrons and the deformation-density models, in which the aspherical functions describe the deviation from the independent atom model and consequently the bonds, lone-pair and other interactions. In the atom-centered multipole models, the aspherical density is added to the unperturbed core density, as in the $\kappa - formalism$, while in deformation-density models the aspherical density is superimposed on the IAM density, but the expansion and contraction of the

valence density is not treated in an explicit form.

5.2.2.1 Multipolar density functions

The multipolar density functions are usually expressed in three coordinates r, θ and ϕ. This way, it is possible to express the multipolar density functions as the product of radial functions, which depend only on the r component, with the angular function, which depends on the θ and ϕ.

So, the angular functions are represented by real spherical harmonic functions, $y_{lm\pm}$ that are given by a linear combination of the complex spherical harmonic functions Y_{lm}. This relation is given by:

$$y_{l0} = Y_{l0} \tag{5.6}$$

for $m \geq 0$ is:

$$y_{lm+} = (-1)^m (Y_{lm} + Y_{l,-m})/2^{1/2} \tag{5.7}$$

$$y_{lm-} = (-1)^m (Y_{lm} - Y_{l,-m})/(2^{1/2} i) \tag{5.8}$$

And these functions can be given in other form, by:

$$y_{lm+}(\theta, \phi) = N_{lm} P_l^m(\cos\theta) \cos m\phi \tag{5.9}$$

$$y_{lm-}(\theta, \phi) = N_{lm} P_l^m(\cos\theta) \sin m\phi \tag{5.10}$$

where $P_l^m(\cos\theta)$ are the associated Legendre functions and N_{lm} is the normalization factor dependent of l and m.

The symmetry properties of these functions are analyzed for different values of l and m. For $l = 0$ and consequently $m = 0$ the function is spherically symmetric. When $l \neq 0$ and $m = 0$ the functions present a cylindrical symmetry along the z axis, because the ϕ dependence disappears. The l even functions have a symmetric inversion in relation to the atomic site, in contrast the odd functions are antisymmetric. Then, for a particular site in a molecule it is possible to restrict the values of l and m for a better description of the local symmetries of the molecule.

The functions y_{lmp}, where $p = \pm$, are the atomic orbitals and y^2_{lmp} is the probability distribution, then their integral should be equal to 1. Therefore,

$$\int y^2_{lmp} d\Omega = 1 \tag{5.11}$$

where $d\Omega$ is the volume element in $\theta - \phi$ space. This normalization expression is appropriate for wave functions, however for charge density the normalization equations are different because the charge is given by the integral over the first power of the function. This way, we generally use the density functions, d_{lmp}, that are equal to y_{lmp} but with a different normalization factor, N'_{lm}. The new normalization condition is given by:

$$\begin{cases} \int |d_{lmp}| d\Omega = 2 & \text{if } l > 0 \\ \int |d_{lmp}| d\Omega = 1 & \text{if } l = 0 \end{cases} \tag{5.12}$$

So this normalization conditions denote that the population parameter is equal to 1 when there is a population of one electron in the spherically symmetric function, d_{00}. On the other hand the nonspherical functions for $l > 0$ have positive and negative lobes with equal number of electrons.

Finally, the function d_{lmp} can be expressed in a system of cartesian coordinates using c_{lmp}, but it is necessary to reformulate the normalization factor for L_{lm} in this new system of coordinates,

$$d_{lmp} = L_{lm} c_{lmp}. \tag{5.13}$$

The l index is associated to the multipoles, where $l = 0, 1, 2, ...$ correspond to the monopole, dipole, quadrupole and so on, moments of the atomic charge distribution in the system.

Such as previously defined, the valence and core density are spherical and only the valence is redefined using the κ parameter, but the deformation density has a different radial dependence to describe the interaction between atoms, in the bond regions where the radial dependence should be more diffuse.

The electron density is a sum over the product of the atomic orbitals and the radial dependence is related directly with Slater-type radial functions, then the

normalized radial density functions is given by:

$$R_l(r) = \kappa'^3 \frac{\zeta^{n_l+3}}{(n_l+2)!}(\kappa' r)^{n_l} exp(-\kappa'\zeta_l r) \tag{5.14}$$

The κ' parameter describe the expansion and contraction of the deformation density and is independent of the κ parameter of spherical valence density. The single-Slater ζ values are obtained for the electron sub-shells of isolated atoms, in energy optimized system, by the calculations of Clementi and Raimondi [26]. In electron density this functions are multiplied by a factor of 2. Finally, the coefficient n_l is limited by condition $n_l \geq l$, imposed by Poisson's electrostatic equation.

5.2.2.2 The multipole density formalism

The description of the electron density of each atom by applying the multipole formalism includes in the deformation valence density the angular and radial functions previously analyzed. Thus the atomic density can be presented with the multipolar density formalism expressed by:

$$\rho_{at}(\mathbf{r}) = P_c\rho_c(r) + P_v\kappa^3\rho_v(\kappa r) + \sum_{l=0}^{l_{max}} \kappa'^3 R_l(\kappa' r) \sum_{m=0}^{l} P_{lm\pm} d_{lm\pm}(\theta,\phi) \tag{5.15}$$

The multipole formalism describes the initial density form obtained from the IAM, with the expansion or contraction of the valence shell parameter, to which is added the sum term of multipolar functions with a description of the deformation density using the Slater-type radial, the spherical harmonic functions and the associated κ' parameter of the expansion or contraction.

This formalism is usually applied using local atomic coordinates system and their local symmetries, which allows the introduction of the chemical constraints of the crystal.

Chapter 6

Computational methods

6.1 Introduction

The Schrödinger equation is the fundamental basis of the *ab initio* computational methods. Applying the principles of quantum mechanics it is possible to obtain several properties of the molecular system such as total energy, electronic structure, nonlinear optical response and others. The Schrödinger equation for an isolated molecule is

$$\hat{H}\Psi = i\frac{\partial\Psi}{\partial t} \tag{6.1}$$

where $\hat{H}$ and Ψ are the Hamiltonian and the time-dependent many particle wave function, respectively.

The Hamiltonian of the system with M nuclei and N electrons is given by,

$$\begin{aligned}\hat{H} = &-\sum_{A=1}^{M}\frac{1}{2M_A}\nabla_A^2 + \sum_{A=1}^{M-1}\sum_{B>A}^{M}\frac{Z_A Z_B}{R_{AB}} \\ &-\sum_{i=1}^{N}\frac{1}{2}\nabla_i^2 - \sum_{i=1}^{N}\sum_{A=1}^{M}\frac{Z_A}{r_{iA}} + \sum_{j>1}^{N-1}\sum_{i=1}^{N}\frac{1}{r_{ij}}\end{aligned} \tag{6.2}$$

where, the nucleus A is defined by a mass, M_A, and charge, Z_A and R_{AB}, r_{iA} and r_{ij} are the distances between the nuclei (A and B), between the electron i and nucleus and between electrons i and j, respectively.

When the calculations with quantum chemical methods are performed without

using empirical or semi-empirical parameters they are designated as *ab initio* methods.

6.2 *Ab initio* calculations

6.2.1 Born-Oppenheimer approximation

In the *ab initio* calculations it is possible to perform the separation of the electronic and nuclear wave functions, this is the Born-Oppenheimer approximation (BO). Separation is achieved knowing that nucleus are much heavier than electrons and assuming that electrons are moving between frozen nucleus. Then the total wave function can be expressed by,

$$\Psi(\mathbf{R}, \mathbf{r}) = \Psi^{el}(\mathbf{r}, \mathbf{R})\Psi^{nuc}(\mathbf{R}) \tag{6.3}$$

where the electronic wave function depend on the nuclear positions $\mathbf{R}$ parametrically. Then, the Schrödinger equation can be solved only for an electronic wave function, obtaining the electronic energy for a set of nuclear coordinates that defines the structure. The electronic energy and the nuclear repulsion energy can then summed and the result is used as a potential energy surface in the equation of the nuclear wave function.

6.2.2 Hartree-Fock

The Hartree-Fock (HF) method assumes a non-relativistic many-electron system where it is applied the BO approximation. This method converts the many-electron molecular Schrödinger equation into a set of one-electron Schrödinger equations with the application of the mean field approximation where the electron-electron interaction is replaced by an averaged effective potential.

$$\hat{H}_e = \sum_{i=1}^{N} \hat{h}(i), \hat{h}(i) = -\sum_{i=1}^{N} \frac{1}{2}\nabla_i^2 - \sum_{i=1}^{N}\sum_{A=1}^{M} \frac{Z_a}{r_{iA}} + v_{eff}(\mathbf{r}_i) \tag{6.4}$$

where $\hat{h}(i)$ is an one-electron Hamiltonian for the ith electron. The average effective potential, $v_{eff}(\mathbf{r}_i)$, is caused by all other $N-1$ electrons of the system. This Hamiltonian can be called the Fock operator, $\hat{F}(i)$, where the effective potential is replaced by summation of the Coulomb operator, $\hat{J}_i$ that gives the electron-electron repulsion and $\hat{K}_i$ is the operator that defines the exchange energy. Then, the Fock operator is given by

$$\hat{F}(i) = -\sum_{i=1}^{N} \frac{1}{2}\nabla_i^2 - \sum_{i=1}^{N}\sum_{A=1}^{M} \frac{Z_a}{r_{iA}} + \sum_{i=1}^{N}(\hat{J}_i - \hat{K}_i) \tag{6.5}$$

The electronic wave function depends of the spacial and spin coordinates of all atoms and these functions are antisymmetric in respect to interchange of two electrons. This requirement is satisfied by the Slater determinant built from the one-electron wave functions for all N electrons:

$$\Psi(\mathbf{r}_1, \cdots, \mathbf{r}_N) = \frac{1}{\sqrt{N!}} \begin{vmatrix} \psi_1(\mathbf{r}_1) & \psi_2(\mathbf{r}_1) & \cdots & \psi_N(\mathbf{r}_1) \\ \psi_1(\mathbf{r}_2) & \psi_2(\mathbf{r}_2) & \cdots & \psi_N(\mathbf{r}_2) \\ \vdots & \vdots & \ddots & \vdots \\ \psi_1(\mathbf{r}_N) & \psi_2(\mathbf{r}_N) & \cdots & \psi_N(\mathbf{r}_N) \end{vmatrix} \tag{6.6}$$

These one-electron wave functions satisfy the Hartree-Fock equations:

$$\hat{F}(i)\psi_k(\mathbf{r}_i) = \epsilon_k \psi_k(\mathbf{r}_i) \tag{6.7}$$

each of these functions are called Hartree-Fock molecular orbitals and their eigenvalues are orbital energies. Then, according to the variational theorem, using a trial wave function can only lead to a value of energy larger than or equal to the true energy of the ground state of system.

So, starting from a set of initial guessed orbitals appropriately chosen one can solve the Hartree-Fock equations to obtain an approximation of the molecular ground state and this is repeated in a self-consistent manner until a certain threshold is reached.

6.2.3 Density Functional Theory

The Density Functional Theory (DFT) does not depend on a large number of variables as HF methods. In the HF it is required the use of $3N$ variables for electron, even after applying the BO approximation. In DFT the number of variables is reduced with the introduction of the electron density, $\rho(\mathbf{r})$, with the advantage of only depending on the three spacial coordinates and allowing the determination of the molecular energy from the electron density instead of a wave function.

The modern DFT is based on two fundamental theorems of P. Hohenberg and W. Kohn [27] where the first says *The ground-state energy from Schrödinger's equation is a unique functional of the electron density*, then the electron density allows to determine unequivocally all properties of the system. The other theorem stating that *The electron density that minimizes the energy of the overall functional is the true electron density corresponding to the full solution of the Schrödinger equation*. Thus, having the correct functional we can vary the electron density and when this is minimized we say that we have obtained the relevant electronic density.

A way of implementation of DFT was performed by Kohn and Sham [28] and proves that solving a set of equations that only involves single electrons, we can find the correct electron density. Then the energy functional of isolated molecule is given by:

$$E[\rho] = V_{Ne}[\rho] + T[\rho] + V_{ee}[\rho] \tag{6.8}$$

where all terms of the equation are functionals, with V_{Ne}, T and V_{ee} the nuclear-electron attraction, kinetic energy and electron-electron interaction, respectively.

The Kohn-Sham method use the effective potential in a non-interacting system with a functional energy,

$$E_s[\rho] = T_s[\rho] + V_{eff}[\rho] \tag{6.9}$$

where index s denote the system considered non-interacting. The only way of non-interacting electron density, $\rho_s(\mathbf{r})$, to be equal to the real electron density, $\rho(\mathbf{r})$, is when $V_{eff}[\rho] = V_{Ne}[\rho] + (T[\rho] - T_s[\rho]) + V_{ee}[\rho]$.

The Kohn-Sham equations is given by:

$$[-\frac{1}{2}\nabla_i^2 + V_{Ne}(\mathbf{r}) + \int \frac{\rho(\mathbf{r}')}{|\mathbf{r}-\mathbf{r}'|}d\mathbf{r}' + V_{xc}[\rho(\mathbf{r})]\psi_i(\mathbf{r}) = \epsilon_i\psi_i(\mathbf{r}) \tag{6.10}$$

where the term $V_{xc}[\rho(\mathbf{r})]$ describe the exchange correlation functional. The integral in equation describe the electron-electron Coulomb repulsion.

This equation is solved iteratively in a SCF which allows to obtain orbitals, $\psi_i(\mathbf{r})$, that gives the electron density of the real system studied by the expression

$$\rho(\mathbf{r}) \equiv \rho_s(\mathbf{r}) = \sum_{i=1}^{N} |\psi_i(\mathbf{r})|^2. \tag{6.11}$$

But the density functional is not exact because the exchange-correlation part does not have a known explicit form. In most functionals the exchange-correlation part is divided in a pure exchange contribution, $E_x[\rho]$, and in a pure correlation contribution, $E_c[\rho]$. Each functional has a different contribution of exchange and correlation that are well defined. The choose of the functional applied in system leads to different performances in the calculations and can be adapted to the properties that we want to obtain.

6.3 Calculation of Optical Properties

6.3.1 Microscopic Optical Properties

While the molecules are described with quantum mechanical theory, the electromagnetic field is treated classically. Thus, from these treatments we introduce the methods used in this thesis for computing the electronic linear and nonlinear polarizabilities.

6.3.1.1 Finite Field method

The Finite Field (FF) method uses numerical differentiation to calculate the static limit of the linear and nonlinear polarizabilities. In uniform electrostatic fields, the total molecular energy E can be expanded into a Taylor series over the

electric field strength F,

$$E(F) = E(0) - \mu_i F_i - \frac{1}{2!}\alpha_{ij}F_iF_j - \frac{1}{3!}\beta_{ijk}F_iF_jF_k - \frac{1}{4!}\gamma_{ijkl}F_iF_jF_kF_l - \dots \quad (6.12)$$

where $E(0)$ is the energy of a molecule without the presence of a field. F_i is the component in the i direction of the external uniform electrostatic field and μ_i is the i component of the molecular dipole moment vector.

In this method the total energy of the molecular system is calculated for different applied Finite Fields at certain directions. So, by means of polynomial fitting, it is possible to obtain the corresponding components of the coefficients in expansion equation 6.12, μ, α, β and so on.

The advantage of the Finite Field method is that it is simple and easy to implement in software. But it has some disadvantages like long time of computation and it is appropriate only for static fields. In this thesis the molecular nonlinear properties were calculated with the Finite Field method. This method is implemented in the software package and GAMESS US [29].

The GAMESS US calculations of this thesis were performed in the Navigator Cluster of the Laboratory for Advanced Computing at University of Coimbra.

6.3.2 Macroscopic Optical Properties

In most organic molecular crystals the energy of intermolecular interactions is much smaller than that of intramolecular chemical bonds. Molecules remain distinguishable entities and the macroscopic nonlinear response of the materials can be described by a simple summation scheme, following the oriented gas model, where the macroscopic second-order susceptibility tensor d_{IJK} originates essentially from the molecular quadratic tensor β_{ijk} expressed in molecular coordinates i, j, k [30]. The susceptibility coefficients depend on the crystal symmetry, the precise orientation of the molecule with respect to the crystal axes and the molecular conformation. This form, the relation between microscopic and macroscopic parameters is:

$$d_{IJK}(-\omega;\omega_1,\omega_2) = \frac{N}{V} f_I(\omega) f_J(\omega_1) f_K(\omega_2) b_{IJK} \quad (6.13)$$

where I ,J ,K are the crystal axes, N is the number of molecules in a volume of unit cell, V and $f(\omega)$ is the local field factors associated each crystal axis. The term b_{IJK} is given by expression:

$$b_{IJK} = \frac{1}{N_g} \sum_s \sum_{ijk} \cos\theta_{Ii}^{(s)} \cos\theta_{Jj}^{(s)} \cos\theta_{Kk}^{(s)} \times \beta_{ijk}^{(s)}(-\omega; \omega_1, \omega_2) \tag{6.14}$$

where N_g is the number of equivalent positions in the unit cell and the product of cosines correspond to the rotation of the molecule defined by index s in relation to the molecular reference in crystal.

The fundamental correction consists in the application of local field factors for reproduce the effect of the local field in the material. Thus, the first approximation for the local field factors, is to consider that these are equal to 1, so the system is isotropic and the local field correction is null. However, an anisotropic system is more realistic one and of these the simplest is the Lorenz-Lorentz spherical cavity model where the local field factors are expressed by:

$$f_I(\omega) = \frac{(n_I(\omega)^2 + 2)}{3} = \frac{1}{1 - \frac{4}{3}\pi\frac{N}{V}a_{II}} \tag{6.15}$$

where, $n_I(\omega)$ is the refractive indices in the I axis and the components of a_{II} are a set of refractive indices of the three principal axes that represents a tensor of average polarizability of the unit cell.

Other model by Wortmann and Bishop (W-B) [31] solved the problem of the local field factors with a extension of Onsager's reaction field model [32]. According to this model we consider the molecule as a point to which is associated the dipole moment in a cavity immersed in a homogeneous dielectric continuum with dielectric constant, ϵ. The dipole of the molecule gives rise to a reaction field, even when the external field is zero, and the reaction field acts on the molecule itself. However, when it is applied an external field, $\mathbf{E}$, in an empty cavity, it arises a cavity field, $\mathbf{E}^C$. Then, by the superposition principle the local field, $\mathbf{E}^L$, the field acting in the cavity with the molecule is obtained by the sum of the field, but generalizing the W-B model for a nonlinear response we can decompose

it into components with amplitudes $\mathbf{E}^{L\Omega}$, $\mathbf{E}^{C\Omega}$, and $\mathbf{E}^{R\Omega}$, therefore:

$$\mathbf{E}^{L\Omega} = \mathbf{E}^{C\Omega} + \mathbf{E}^{R\Omega} \tag{6.16}$$

when the electric field applied is uniform as the response of the medium. Taking into account the continuous and induced components, we can relate the cavity field with the macroscopic field and the reaction field with the dipole moment, p^{Ω}, and these relations can be expressed by:

$$\begin{aligned} \mathbf{E}^{C\Omega} &= \mathbf{f}^{C\Omega} \cdot \mathbf{E}^{\Omega} \\ \mathbf{E}^{R\Omega} &= \mathbf{f}^{R\Omega} \cdot \mathbf{p}^{\Omega} \end{aligned} \tag{6.17}$$

where $\mathbf{f}^{C\Omega}$ and $\mathbf{f}^{R\Omega}$ are the cavity and reaction field tensors at frequency Ω. From this tensor it can be obtained the effective first-order hiperpolarizability of the molecule in W-B model given by:

$$\begin{aligned} \beta^{eff}_{rst}(-2\omega;\omega,\omega) = F^{R2\omega}_{rr}(F^{R\omega}_{ss} f^{C\omega}_{ss})(F^{R\omega}_{tt} f^{C\omega}_{tt}) \\ \times \beta^{sol}_{rst}(-2\omega;\omega,\omega) \end{aligned} \tag{6.18}$$

Where the $\beta^{sol}_{rst}(-2\omega;\omega,\omega)$ is the hyperpolarizability obtained in the first approximation without local field. This treatment based on the W-B model is fully described in an article by Silva *et al.* [33] and is implemented using the computational software package Mathematica® version 8.0.

Chapter 7

Guanidine salts

Guanidine a small molecule with 3-fold symmetry and formula CH_5N_3 has great interest from the physical point of view, mainly in research of compounds with potential nonlinear optical properties, such as demonstrated by Zyss *et al.* [34]. Within crystalline structures, guanidine promotes formation of hydrogen-bonding interactions with organic acids, since this cation is a strong base, with $pK_a = 13.5$, and has six potential H-donor to participate in hydrogen-bonding interactions. Some examples of the guanidinium salts structures are with the aromatic mono-

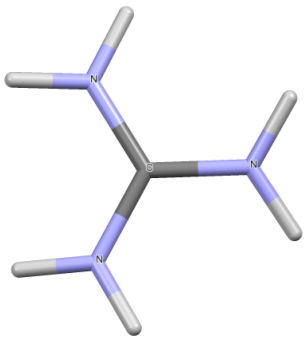

Figure 7.1: Geometry of the guanidinium cation after optimization.

carboxylic acids [35; 36], in the hydrated form and with 3-nitrobenzoic acid [37], 4-amino-3,5,6-trichloropicolinic acid, [38], and guanidinium 4-aminobenzoate [39], in the anhydrous form. These structures are dominated by hydrogen-bonding interactions, where the guanidinium cation forms several H-bonds with acceptor groups of other molecules.

The guanidinium cation is completely planar and the symmetry is trigonal, D_{3h}, as shown in Fig. 7.1. This symmetry corresponds of an equilateral triangle with one 3-fold axis, 3 horizontal twofold axes, one horizontal plane and 3 vertical planes containing the horizontal axes [40]. The guanidinium ion has three C-N bonds for central carbon atom with bond lengths between 1.313 and 1.329 Å and the bond order of 1.33. Therefore, if guanidinium cation would have a perfect trigonal symmetry, the hyperpolarizability would be given only by the octupolar component ($\beta = \beta_{J=3}$), as was analyzed in section 2.4.2 (molecules with strong octupolar component has several advantages). After geometry optimization calculations show a dipole component of 0.05au and an octupolar component of 157.37au. Using these values Expression 2.28 yields $\rho = 3383.84$ that shows a strong octupolar character of guanidinium cation.

7.1 Guanidinium nicotinate

The salt guanidinium nicotinate (**g1**) is monoclinic with the centrosymmetric space group $P2_1/c$ and the asymmetric unit contains one guanidinium cation and a nicotinate anion (Fig. 7.2).

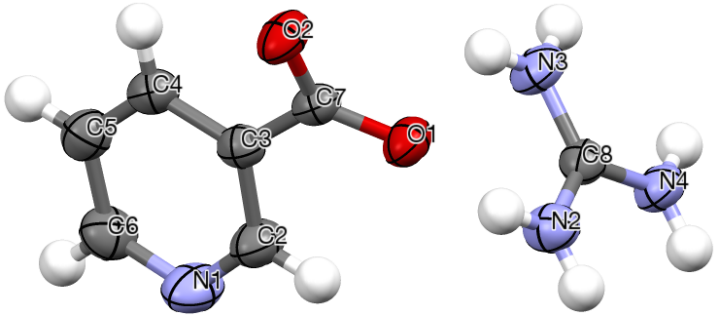

Figure 7.2: A plot of the asymmetric unit of **g1**. Displacement ellipsoids are drawn at the 50% probability level.

Regarding the anion, as usual, the O−C−O angle of the carboxylate group is larger than 120° [125.1(1)°] because of the steric effect of lone-pair electrons on both O atoms. The bond lengths in the deprotonated carboxyl group [1.2572(13) and 1.2439(13) Å] indicate delocalization of the charge over both O atoms. The carboxylate group is rotated 22.6° around the C7−C3 bond.

Table 7.1: Hydrogen-bonding geometry (Å,°) of guanidinium nicotinate.

D−H$\cdots A$	D−H	H$\cdots A$	$D\cdots A$	D−H$\cdots A$
N2−H2A$\cdots$O1	0.86	1.98	2.8245(13)	165.8
N2−H2B$\cdots$N1^{ii}	0.86	2.16	2.9897(16)	161.3
N3−H3A$\cdots$O2^{iii}	0.86	2.09	2.8206(13)	142.2
N3−H3B$\cdots$O1^{i}	0.86	1.96	2.8132(14)	173.9
N4−H4A$\cdots$O2^{i}	0.86	2.02	2.8767(13)	172.3
N4−H4B$\cdots$N1^{ii}	0.86	2.69	3.3896(16)	139.5

symmetry codes $i: -x+1, y+1/2, -z+1/2; ii: -x, -y, -z$; $iii: -x+1, -y, -z+1$.

The structure has an extensive 3D network with six distinct hydrogen-bond interactions (see Table 7.1 and Fig. 7.3) with all the H atoms of the guanidinium cation participating in N−H$\cdots$O and N−H$\cdots$N interactions with the anion.

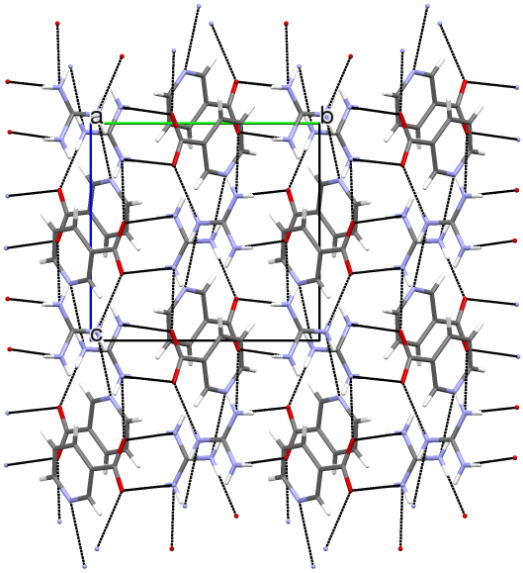

Figure 7.3: A packing diagram for **g1**, viewed down the a axis, with the hydrogen bonds depicted by dashed lines.

The finite graphs of descriptor D are the dominant hydrogen-bonding motifs, at the first level. In the hydrogen-bond network, there are also second order rings with descriptors $R_2^2(8)$ and $R_4^4(16)$ and chains with the graph-sets $C_2^2(10)$, $C_2^2(8)$ and $C_2^2(6)$.

7.2 Guanidinium isonicotinate

Guanidinium isonicotinate, **g2**, (Fig. 7.4) crystallizes in the monoclinic and centrosymmetric space group $P2_1/c$ with four positive ions and four negative ions per unit cell.

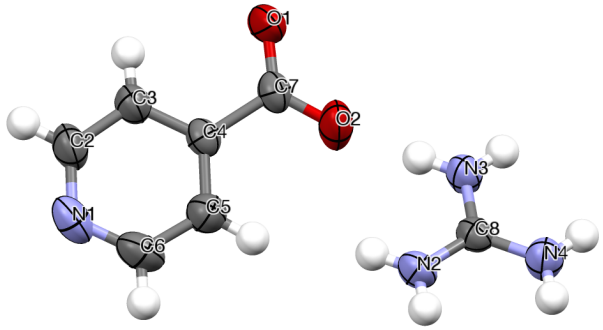

Figure 7.4: A plot of the asymmetric unit of **g2**. Displacement ellipsoids are drawn at the 50% probability level.

The negative ion, the deprotonated isonicotinic moiety has the carboxylic group slightly rotated from the aromatic ring plane as seen by the torsion angle, C3−C4−C7−O1 -2.8(2)°. The C−O distances are characteristic of a deprotonated carboxylic group with a delocalized character, 1.245(2) (O1−C7) and 1.239(2) Å (O2−C7). The C−N distances within the ring are 1.325(2) (N1−C2) and 1.328(2) Å (N1−C6).

The structure is stabilized by a three-dimensional network of N−H$\cdots$O and N−H$\cdots$N hydrogen bonds between the anions and cations (Fig. 7.5, Table 7.2).

Table 7.2: Hydrogen-bonding geometry (Å,°) of guanidinium isonicotinate.

D−H$\cdots A$	D−H	H$\cdots A$	$D\cdots A$	D−H$\cdots A$
N2−H2A$\cdots$N1^{i}	0.86	2.12	2.9425(19)	159.6
N2−H2B$\cdots$O1^{ii}	0.86	2.07	2.8177(18)	145.7
N3−H3A$\cdots$O2	0.86	2.17	2.9192(17)	146.2
N3−H3B$\cdots$O2^{ii}	0.86	2.05	2.8959(16)	167.0
N4−H4B$\cdots$O1^{ii}	0.86	1.97	2.8264(17)	171.4

symmetry codes $i: -x+2, y-1/2, -z-1/2$;
$ii: x, -y+1/2, z-1/2; iii: -x+1, -y, -z$.

Each guanidinium cation is linked to four anions but one hydrogen atom does not participate in any hydrogen bond.

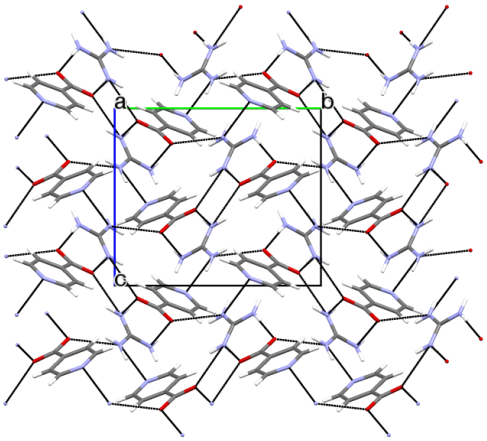

Figure 7.5: A packing diagram for **g2**, viewed down the *a* axis, with the hydrogen bonds depicted by dashed lines.

The only first-order hydrogen-bond motifs are noncyclic dimers with graph-set $D_1^1(2)$. At the second level, there are chains with the graph-sets $C_2^2(8)$ and $C_2^1(6)$, rings of descriptor $R_2^2(8)$ formed by anion/cation pairs and rings formed by two anions and two cations with graph-sets $R_4^4(16)$ and $R_4^4(18)$.

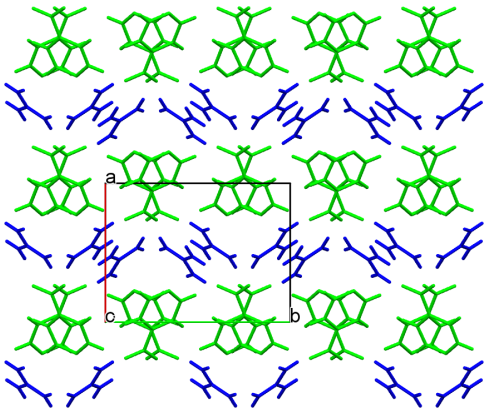

Figure 7.6: A packing diagram for **g2**, viewed down the *c* axis, showing the layer formation. Alternate layers are colored blue (cations) and green (anions).

The cations and the anions in the **g2** are packed in alternate layers parallel to the *bc* plane (see Fig. 7.6).

7.3 Guanidinium 2,5-dihydroxyterephtalate

The salt Guanidinium 2,5-dihydroxyterephtalate, (**g3**) (Fig. 7.7),is monoclinic with the centrosymmetric space group $P2_1/c$ and the asymmetric unit consists of one guanidinium cation and a 2,5-dihydroxyterephtalate anion.

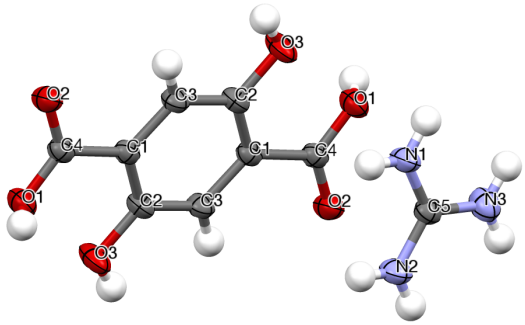

Figure 7.7: A plot of the asymmetric unit of **g3**. Displacement ellipsoids are drawn at the 50% probability level.

In the anion, due to the presence of an inversion at the center of the ring, there is disorder in the carboxylic groups, each one having an hydrogen atom with 0.5 occupancy.

The anion is almost in a planar conformation, with a dihedral angle of 5.55(36)° between the aromatic ring and the carboxylate groups. The hydroxyl groups are also in the plane of the phenyl ring.

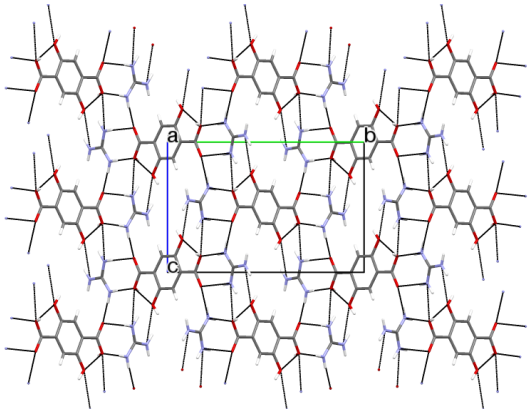

Figure 7.8: A packing diagram for **g3**, viewed down the a axis, with the hydrogen bonds depicted by dashed lines.

There are six N−H···O hydrogen bonds and one O−H···O hydrogen bond in this structure (see Fig. 7.8, Table 7.3) forming a 3D network. Each cation is linked to four anions.

Table 7.3: Hydrogen-bonding geometry (Å,°) of Guanidinium 2,5-dihydroxyterephtalate.

D−H···A	D−H	H···A	D···A	D−H···A
O3−H3···N3^{i}	0.86	2.43	3.0168(19)	125.6
N1−H1A···O1^{ii}	0.86	1.93	2.7867(17)	175.8
N1−H1B···O2^{i}	0.86	1.99	2.8334(18)	166.2
N2−H2A···O2 ^{ii}	0.86	2.12	2.9611(18)	166.4
N2−H2B···O3^{iii}	0.86	2.40	3.138(2)	144.6
N2−H2B···O1^{iv}	0.86	2.42	2.9242(18)	117.7
N3−H3C···O3^{iii}	0.86	2.24	3.0168(19)	150.4

symmetry codes $i : x, -y + 1/2, z - 1/2$;;
$ii : x + 1, y, z, z - 1/2; iii : x, -y + 1/2, z + 1/2z$;
$iv : x + 1, -y + 1/2, z + 1/2$.

7.4 Guanidinium 2,5-dihydroxyterephtalate monohydrate

The crystals of guanidinium 2,5-dihydroxyterephtalate monohydrate (**g4**) are monoclinic with the space group $P2_1/m$.

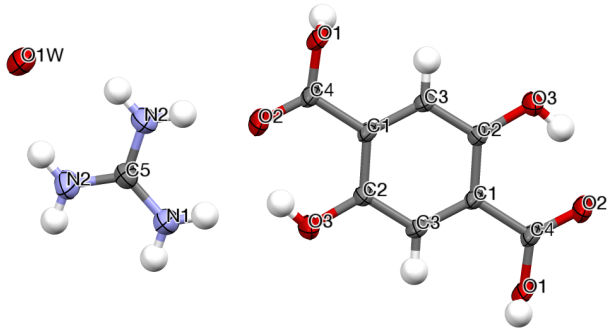

Figure 7.9: A plot of the asymmetric unit of **g4**. Displacement ellipsoids are drawn at the 50% probability level.

The asymmetric unit has one guanidinium cation, one 2,5-dihydroxyterephtalate anion and one water molecule (see Fig. 7.9). As in the previous structure, the anion has disordered carboxylic groups due to the inversion symmetry. Each carboxylic group has one hydrogen atom with 0.5 occupancy. The oxygen atom of the water molecule lies on a crystallographic mirror and it was impossible to refine the hydrogen atoms positions in a meaningful way.

The anion is almost planar, with a dihedral angle of 4.22(18)° between the least-squares planes of the aromatic ring and the carboxylate groups. The hydroxyl groups lie in the plane of the ring. Comparing the anion in this structure with that in **g3** it is evident the different orientations of the hydroxyl groups and of the carboxylic groups.

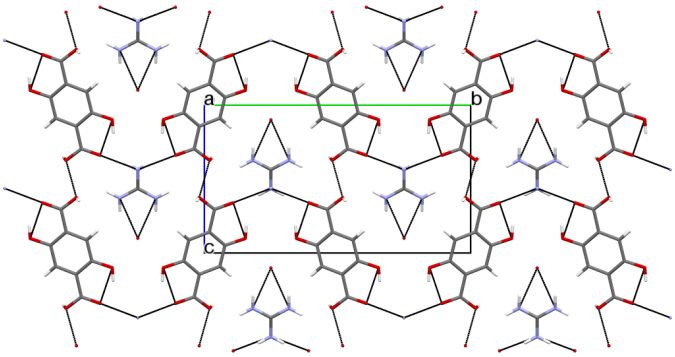

Figure 7.10: A packing diagram for **g4**, viewed down the *a* axis, with the hydrogen bonds depicted by dashed lines.

Table 7.4: Hydrogen-bonding geometry (Å,°) of Guanidinium 2,5-dihydroxyterephtalate monohydrate.

D−H$\cdots A$	D−H	H$\cdots A$	$D\cdots A$	D−H$\cdots A$
O3−H3$\cdots$N3^{i}	0.86	2.43	3.0168(19)	125.6
O3−H3$\cdots$O2	0.82	1.84	2.5664(16)	146.2
N1−H1A$\cdots$O2^{i}	0.86	2.19	2.9754(18)	152.5
N2−H2A$\cdots$O1^{ii}	0.86	2.37	3.086(2)	140.7
N2−H2B$\cdots$O1W	0.86	2.17	2.941(2)	148.6

symmetry codes $i : x+1, y, z$;
$ii - x+1, -y, -z+1$.

The structure is stabilized by N−H$\cdots$O hydrogen bonds (see Fig. 7.10, Ta-

ble 7.4). There is an intramolecular hydrogen bond (graph-set $S_1^1(6)$) involving the hydroxyl group and one of the carboxylic oxygen atoms.

7.5 Guanidinium cyclopropanecarboxylate

The crystal structure of the salt guanidinium cyclopropanecarboxylate (**g5**) (Fig. 7.11), is orthorhombic with the noncentrosymmetric space group $P2_12_12_1$, thus allowing second harmonic generation. The asymmetric unit consists of one guanidinium cation and a cyclopropanecarboxylate anion.

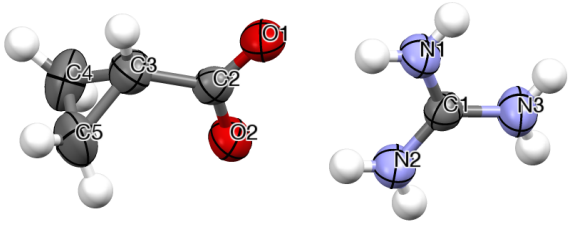

Figure 7.11: A plot of the asymmetric unit of guanidinium cyclopropanecarboxylate. Displacement ellipsoids are drawn at the 50% probability level.

The asymmetric unit consists of one guanidinium cation and a cyclopropanecarboxylate anion. In the anion the 3-member ring is almost perpendicular to the carboxylate group, with a dihedral angle of 86.8(2)° between the least-squares planes. The O−C−O angle of the carboxylate group is larger than 120° [123.7(2)°] because of the steric effect of lone-pair electrons on both O atoms. The bond lengths in the carboxylate group [1.239(3) and 1.240(3) Å] are intermediate between the single C_{sp^2}−O (1.308-1.320 Å) and double C_{sp^2}=O bond lengths (1.214-1.224 Å) [41], indicating delocalization of the charge over both O atoms of the COO^- group.

All the H atoms on the guanidinium cation participate in N−H$\cdots$O interactions with the anion (Fig. 7.12, Table 7.5) and each carboxylate O atom accepts three hydrogens. forming infinite layers propagating in the *ab* plane (Fig. 7.13). In each layer the cation is bonded to three anions, two approximately perpendicular and one approximately coplanar. The dominant first-order hydrogen-bond motifs are noncyclic dimers with graph set D, according to Etter's graph-set

Table 7.5: Hydrogen-bonding geometry (Å,°) of guanidinium cyclopropanecarboxylate.

D−H$\cdots A$	D−H	H$\cdots A$	$D\cdots A$	D−H$\cdots A$
N1−H1A$\cdots$O1	0.86	1.93	2.783(2)	169.9
N1−H1B$\cdots$O1^{i}	0.86	2.13	2.922(2)	153.9
N2−H2A$\cdots$O2	0.86	2.06	2.901(2)	164.0
N2−H2B$\cdots$O2^{ii}	0.86	2.12	2.907(2)	151.4
N3−H3A$\cdots$O2^{ii}	0.86	2.27	3.018(2)	144.8
N3−H3B$\cdots$O1^{i}	0.86	2.33	3.072(2)	144.8

symmetry codes $i : x-1/2, -y+3/2, -z+1$;
$ii : x-1/2, -y+1/2, -z+1$.

theory [42]. In the hydrogen-bond network, there are also second order rings of descriptor $R_2^2(8)$ and several chains with the graph-sets $C_2^2(8)$ and $C_2^2(6)$.

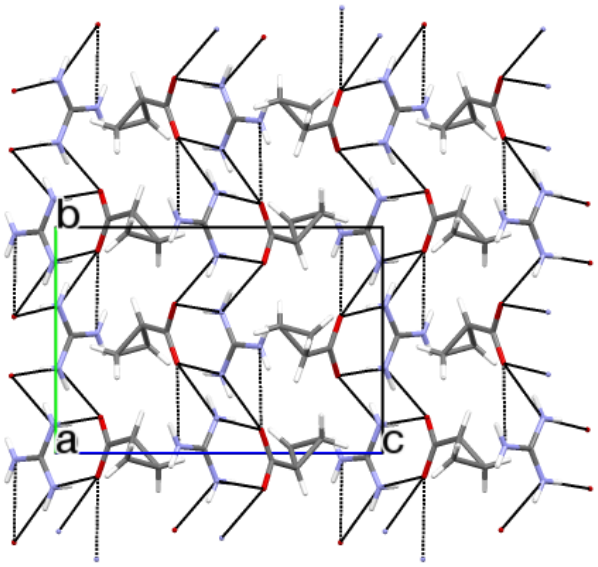

Figure 7.12: A packing diagram for **g5**, viewed down the a axis, with the hydrogen bonds depicted by dashed lines.

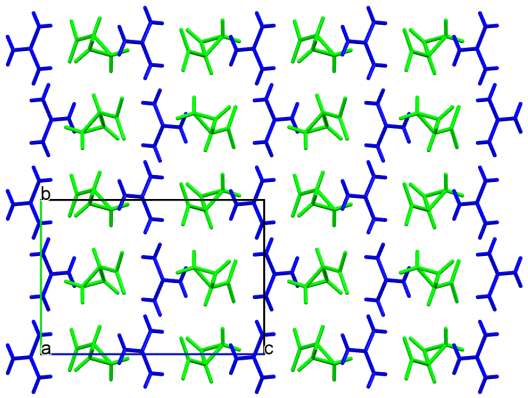

Figure 7.13: A packing diagram for **g5**, viewed down the *a* axis, showing the layer formation. Alternate layers are colored blue (cations) and green (anions).

7.6 Bis(guanidinium) 2,2'-bipyridine-3,3'- dicarboxylate

The crystal structure of the salt bis(guanidinium) 2,2'-bipyridine-3,3'-dicarboxylate, **g6**, is orthorhombic with the noncentrosymmetric space group $Pna2_1$.

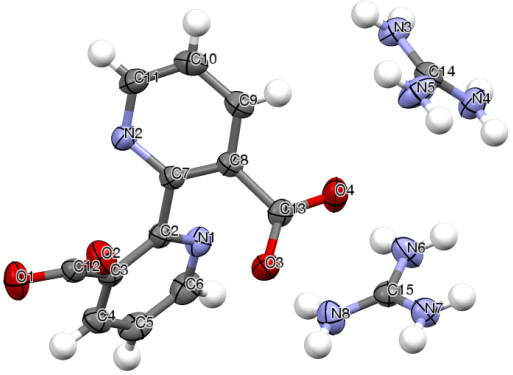

Figure 7.14: A plot of the asymmetric unit of **g6**. Displacement ellipsoids are drawn at the 50% probability level.

The asymmetric unit consists of two guanidinium cations and one doubly deprotonated anion, 2,2'-bipyridine-3,3'-dicarboxylate (Fig. 7.14). In the anion, the carboxylate groups are rotated out of the planes of the respective bipyridine rings (37.5° for O1−C12−O2 and 40.0° for O3−C13−O4). The angle between the least-squares planes of the aromatic rings is 59.3°.

Table 7.6: Hydrogen-bonding geometry (Å,°) of **g6**.

D−H$\cdots A$	D−H	H$\cdots A$	$D\cdots A$	D−H$\cdots A$
N3−H3A$\cdots$O3^{i}	0.86	2.17	3.018(3)	167.4
N3−H3B$\cdots$O1^{ii}	0.86	2.04	2.886(2)	168.0
N4−H4A$\cdots$N2^{iii}	0.86	2.37	3.165(3)	154.4
N4−H4B$\cdots$O2^{ii}	0.86	2.04	2.888(2)	170.4
N5−H5A$\cdots$O4^{i}	0.86	2.60	3.188(3)	126.1
N5−H5B$\cdots$O1^{iii}	0.86	1.98	2.805(3)	160.6
N6−H6A$\cdots$O4^{vi}	0.86	2.03	2.873(2)	167.6
N6−H6B$\cdots$N2^{ii}	0.86	2.66	3.373(3)	141.3
N7−H7A$\cdots$O2^{ii}	0.86	2.13	2.985(3)	171.8
N7−H7B$\cdots$O4	0.86	1.98	2.815(2)	164.1
N8−H8A$\cdots$O3^{vi}	0.86	2.05	2.902(2)	169.7
N8−H8B$\cdots$N1	0.86	2.34	3.120(3)	150.6

symmetry codes $i: x+1/2, -y+1/2, z$;
$ii: -x-3/2, y-1/2, z+1/2; iii: -x-3/2, y+1/2, z+1/2$;
$vi: x, y-1, z$.

The structure is stabilized by an extensive 3D network of 12 distinct hydrogen-bond interactions (see Table 7.6 and Fig. 7.15).

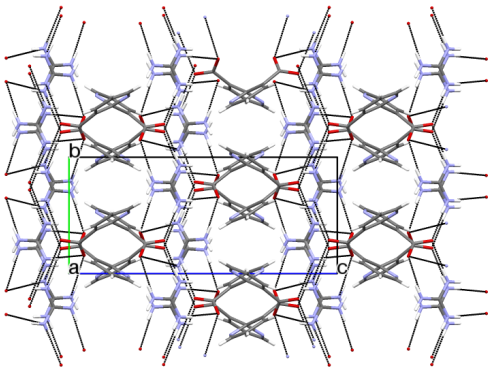

Figure 7.15: A packing diagram for **g6**, viewed down the a axis, with the hydrogen bonds depicted by dashed lines.

The finite graphs of descriptor D are the dominant hydrogen-bonding motifs, at the first level. In the hydrogen-bond network, there are also second order rings with descriptors $R_2^2(8)$, associated with H-bonds involving the carboxylate groups, and chains with the graph-sets $C_2^2(11)$ and $C_2^2(13)$ just to mention the

most relevant motifs.

In this structure the guanidinium cations are parallel to the plane (605) or to the plane ($\overline{6}05$). The cations and the anions are packed in alternate layers parallel to the *ab* plane (see Fig. 7.16).

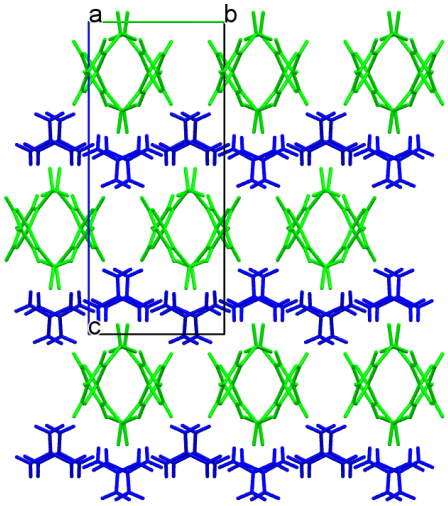

Figure 7.16: A packing diagram for **g6**, viewed down the *a* axis, showing the layer formation. Alternate layers are colored blue (cations) and green (anions).

7.7 NLO properties of guanidine salts

Of the guanidine compounds previously described only the guanidinium cyclopropanecarboxylate and guanidinium 2,2'-bipyridine-3,3'-dicarboxylic crystallize in noncentrosymmetric space groups.

The guanidinium cyclopropanecarboxylate compound crystallizes with a space group $P2_12_12_1$ and belongs to the crystal class of 222. Consequently, the second-order susceptibility tensor for this crystal is given by:

$$\begin{pmatrix} 0 & 0 & 0 & d_{14} & 0 & 0 \\ 0 & 0 & 0 & 0 & d_{25} & 0 \\ 0 & 0 & 0 & 0 & 0 & d_{36} \end{pmatrix} \tag{7.1}$$

Considering that the Kleinman permutation symmetry is valid, $d_{14} = d_{25} =$

d_{36}, such as showed by Eq. 2.18 and Eq. 2.19.

On the other hand the guanidinium 2,2'-bipyridine-3,3'-dicarboxylic compound has a space group $Pna2_1$ where the class is $mm2$. Therefore the matrix d_{ij} is given by:

$$\begin{pmatrix} 0 & 0 & 0 & 0 & d_{15} & 0 \\ 0 & 0 & 0 & d_{24} & 0 & 0 \\ d_{31} & d_{32} & d_{33} & 0 & 0 & 0 \end{pmatrix} \tag{7.2}$$

Then, if the Kleinman symmetry is valid for this system we can reduce the number of the independent components so that $d_{31} = d_{15}$ and $d_{32} = d_{24}$. Therefore we stand with just the components d_{31}, d_{32} and d_{33}.

7.7.1 Experimental Kurtz and Perry powder results

The results are obtained from the Kurtz and Perry powder method for guanidine salts and are presented in the Table 7.7 for **g5** and **g6**.

Table 7.7: The guanidine salts **g5** and **g6** SHG efficiencies compared to the urea standard.

Salt	**g5**	**g6**
SHG efficiency	0.29	0.30

These results are conditioned by several factors of the experimental arrangement like particle size and other conditions of the experimental setup. Comparison to the urea standard is necessary in several steps of the experiment and the uncertainty error is estimated around the 10% value.

7.7.2 Computational nonlinear optical properties

The computational calculations of the macroscopic NLO coefficients, d_{IJK}, were performed from the molecular hiperpolarizability tensor, βijk, of the asymmetric units of the guanidine salts **g5** and **g6** using several methods.

The Table 7.8 shows the results obtained for some elements of the β_{ijk} tensor obtained with distinct methods as HF and DFT with different functionals like LYP, BHHLYP, B3LYP and BLYP. The calculations shows a better agreement between results obtained with HF methods and DFT with LYP functional. There

Table 7.8: The β_{ijk} components of the isolated molecules of guanidinium cyclopropanecarboxylate and guanidinium 2,2'-bipyridine-3,3'-dicarboxylic, calculated with HF method and with some functionals of the DFT method.

	g5		**g6**		
	β_{XXX}	β_{XXZ}	β_{XXX}	β_{YYY}	β_{ZZZ}
HF	29.8	-45.5	-161.5	144.8	-152.9
LYP	31.1	-44.6	-160.9	141.1	-150.8
BHHLYP	94.4	-95.5	-384.5	290.6	-434.9
B3LYP	227.7	-204.8	541.0	6393.7	-4822.4
BLYP	600.6	-508.8	699.0	11250.0	-5518.7

is a large discrepancy between the functional LYP and the hybrid functionals B3LYP and BHHLYP, and a large discrepancy with BLYP. The deficiency in the description of the molecular hyperpolarizability tensor is due to the treatment of the electron exchange with these functionals [43]. The percentage of HF exchange in these functionals is well defined and is showed in Table 7.9.

Table 7.9: The percentage of the HF exchange in different DFT functionals and in HF method.

Methods	% HF exchange
HF	100
LYP	100
BHHLYP	50
B3LYP	20
BLYP	0

Looking at the values for the asymmetric unit in Table 7.8 where are the results of the two structures, it is evident the increase of the calculated values of the molecular hiperpolarizability with the decrease of percentage of HF exchange.

The calculations performed with DFT method and with LYP functional provide the best results in the description of the β_{ijk} these values were then used to calculate the macroscopic NLO coefficients, d_{IJK} and the angular average of the NLO susceptibility, $\langle d^{2\omega} \rangle$, from the expression deduced by Kurtz and Perry [22]:

$$\langle d^{2\omega}\rangle = [\frac{19}{105}\sum_{i}(d_{iii}^{2\omega})^2 + \frac{13}{105}\sum_{i\neq j} d_{iii}^{2\omega} d_{ijj}^{2\omega} + \frac{44}{105}\sum_{i\neq j}(d_{iij}^{2\omega})^2 + \frac{13}{105}\sum_{ijk,cyclic} d_{iij}^{2\omega} d_{jkk}^{2\omega} + \frac{5}{7}(d_{ijk}^{2\omega})^2]^{1/2}. \quad (7.3)$$

Results are shown in Table 7.10, using two different local field factors (Lorenz-Lorentz and Wortmann-Bishop as explained in section 6.3.2).

Table 7.10: Theoretical susceptibility components (pm/V) for **g5** and **g6**, calculated from the β_{ijk} components of the isolated molecule using the LYP functional, with Lorenz-Lorentz (L-L) and Wortmann-Bishop (W-B) local-field factors.

	g5		**g6**			
	d_{XYZ}	$\langle d\rangle$	d_{ZXX}	d_{ZYY}	d_{ZZZ}	$\langle d\rangle$
L-L	0.12	0.10	-2.07	-1.20	-3.34	2.53
W-B	0.11	0.09	-1.60	-1.02	-2.52	1.97

The components which were calculated with the Lorenz-Lorentz factors tend to be large than the values obtained with Wortmann-Bishop local-field factors. A result already expected since the Wortmann-Bishop correction does not assumes the nonlinear contribution of the local field as negligible. Calculating the SHG efficiencies, (with a Wortmann-Bishop local-field correction factors) one obtain for **g5** 0.04 per urea which is much smaller than 0.29 obtained from the Kurtz and Perry powder method. For **g6** the SHG efficiency is 0.74, that is about the double as obtained experimentally. Possibly, intermolecular interactions within the crystal account for the experimental/calculated discrepancies.

7.7.3 Scalar invariants of the hyperpolarizability

The best way verify the dipolar/octupolar character of the molecules is to compare the vector and sector irreducible components and to evaluate the ρ parameter, see Table 7.11.

In this table is evident the octupolar character of the molecule of guanidinium in the two compounds which favors NLO properties as mentioned earlier. The two anions shows a behavior almost entirely dipolar (as expected).

Table 7.11: The values of the dipolar and octupolar components and the parameter ρ for asymmetric units of compounds **g5**, **g6** and the corresponding anions and cations that are represented by **compound**$^-$ and **compound**$^+$, respectively.

Fragments	invariant vector	invariant septor	ρ
g5	79.28	90.23	1.14
g5$^+$	1.83	117.73	64.10
g5$^-$	149.71	33.48	0.22
g6	492.92	205.79	0.42
g6$^+$	2.07	117.74	56.83
g6$^-$	219.30	133.41	0.61

The results obtained for the asymmetric unit show a greater octupolar component for **g5** and this fact can be justified by a stronger octupolar component in the guanidinium cation of asymmetric unit of the **g5**. The crystals with a point group 222 like the case of **g5** with space group $P2_12_12_1$ the tensor,d_{ij} is composed only by octupolar components and in this way solely the octupolar part of the second hyperpolarizabilities calculated will contribute for the total crystalline d tensor.

7.8 Experimental and computational methods

7.8.1 Single crystal X-ray diffraction

The diffraction measurements were performed with a $MoK\alpha$ radiation on a Bruker APEX II diffractometer [44]. The Lorenz and polarization corrections were applied on the diffraction data and the structures were solved using SHELXS-97 and SHELXL-97 programs [21] (the direct methods and implementation of the refinement of the F^2s by full-matrix least-squares, respectively). In the refinement process, non H-atoms were assigned anisotropic displacement parameters. The H-atoms were placed at calculated positions, refined using the riding model with isotropic displacement parameters.

The crystal details of the structure refinement and the data collected are shown in the Table 7.12 and Table 7.13.

Table 7.12: The crystal details of the structure refinement and the data collected of the Guanidinium nicotinate, **g1**, Guanidinium isonicotinate, **g2**, Guanidinium 2,5-dihyterephtalic, **g3**, and Guanidinium 2,5-dihyterephtalic monohydrate, **g4**.

Salt	**g1**	**g2**	**g3**	**g4**
Emp. formula	$C_7H_{10}N_4O_2$	$C_7H_{10}N_4O_2$	$C_{10}H_{16}N_6O_6$	$C_{42}H_{40}N_6O_5$
Formula weight	182.19	182.19	316.29	708.80
Temperature (K)	293(2)	293(2)	293(2)	293(2)
Wavelength (Å)	0.71073	0.71073	0.71073	0.71073
Crystal system	Monoclinic	Monoclinic	Monoclinic	Triclinic
Space group	$P2_1/c$	$P2_1/c$	$P2_1/c$	$P1$
a (Å)	9.2432(3)	8.6708(3)	4.80680(10)	11.9846(2)
b (Å)	9.9748(3)	10.9357(3)	14.4861(2)	12.7020(2)
c (Å)	10.6214(3)	9.9012(3)	9.90500(10)	13.1431(3)
$\alpha(^\circ)$	90	90	90	96.6840(10)
$\beta(^\circ)$	117.000(2)	108.492(2)	104.5820(10)	103.1680(10)
$\gamma(^\circ)$	90	90	90	91.6080(10)
Volume (Å^3)	872.55(5)	890.37(5)	667.486(18)	1931.82(6)
Z	4	4	4	2
Calc. dens.(g/cm^3)	1.387	1.359	1.574	1.219
Abs. coef. (mm^{-1})	0.106	0.103	0.131	0.082
$F(000)$	384	384	332	748
data collec. range	2.47-27.91°	2.48-27.18°	2.55-27.95°	2.08-28.38°
Index ranges:	$-12 < h < 12$, $-12 < k < 13$, $-13 < l < 13$,	$-11 < h < 10$, $-14 < k < 14$, $-12 < l < 11$,	$-6 < h < 6$, $-18 < k < 19$, $-12 < l < 12$,	$-15 < h < 16$, $-16 < k < 16$, $-17 < l < 17$
Reflections collected/unique	15350 / 2061	14434 / 1966	14189 / 1596	31894
R(int)	0.0216	0.0210	0.0265	0.0241
Completeness (θ=25.00°)	99.1 %	99.8%	99.7%	99.9%
Refin. method	Full-matrix least-squares on F^2			
Data/restraints/parameters	2061/0/118	1966/0/118	1596/0/101	17920/3/957
F^2 Goodness-of-fit	1.016	1.049	1.071	0.988
R indices:				
final [$I > 2\sigma(I)$]	0.0363	0.0421	0.0424	0.0504
wR_2	0.0990	0.1165	0.1330	0.1375
all data	0.0463	0.0539	0.0502	0.1057
wR_2	0.1077	0.1260	0.1558	0.1953
Largest diff. peak and hole (eÅ^{-3})	0.152 / -0.216	0.197 / -0.187	0.440 / -0.562	0.485

Table 7.13: The crystal details of the structure refinement and the data collected of the noncentrosymmetric structures of the Guanidinium cyclopropanecarboxylate, **g5**, and Guanidinium 2,2'-bipyridine-3,3'-dicarboxylic, **g6**.

Salt	**g5**	**g6**
Emp. formula	$C_{10}H_{22}N_6O_4$	$C_{14}H_{20}N_8O_4$
Formula weight	290.32	344.22
Temperature (K)	293(2)	293(2)
Wavelength (Å)	0.71073	0.71073
Crystal system	Orthorhombic	Orthorhombic
Space group	$P2_12_12_1$	Cc
a (Å)	7.8245(11)	12.7749(6)
b (Å)	8.2030(12)	7.5364(3)
c (Å)	11.8751(17)	17.3605(8)
$\alpha(^\circ)$	90	90
$\beta(^\circ)$	90	90
$\gamma(^\circ)$	90	90
Volume (Å^3)	762.20(19)	1671.41(13)
Z	4	4
Calc. dens.(g/cm^3)	1.265	1.368
Abs. coef. (mm^{-1})	0.099	0.107
$F(000)$	312	688
data collec. range	3.02-27.11°	2.35-27.15°
Index ranges:	$-10 < h < 9$, $-10 < k < 10$, $-15 < l < 14$	$-16 < h < 16$, $-9 < k < 9$, $-22 < l < 22$
Reflections collected /unique:	8486 / 1686	29521 / 3724
R(int)	0.0169	0.0320
Completeness (θ=25.00°)	100%	100%
Refin. method	Full-matrix least-squares on F^2	
Data/restraints/parameters: parameters	1686/0/91	3724/1/236
F^2 Goodness-of-fit	1.275	1.086
R indices:		
final [$I > 2\sigma(I)$]	0.0475	0.0434
wR_2	0.1480	0.1227
all data	0.0513	0.0473
wR_2	0.1537	0.1352
Largest diff. peak and hole (eÅ^{-3})	0.298 / -0.134	0.479 / -0.223

7.9 Kurtz and Perry powder method

The SHG efficiency was measured for **g5** and **g6** using the K-P powder method described in the section 4.4.1. The results obtained with this method are presented in terms of the SHG efficiency of Urea, but due the instability of the system is required to perform the measurement of the SHG efficiency of Urea, an usual standard.

7.10 Computational methods

The calculations of microscopic optical properties with the oriented gas model using HF and DFT was carried out with GAMESS US package [45]. The DFT calculations were performed with the GGA functional BLYP [46; 47], the correlation-corrected functionals, LYP [47] with HF exchange and GGA correlation and the hybrid functionals as B3LYP [48] and BHHLYP [49]. The basis set used in all calculations throughout this thesis was the 6-311++G**. The results were obtained using the relative positions and geometries of the ions as obtained from X-ray diffraction. First the static α and β tensorial components were calculated, then, from the microscopic optical properties we calculate the unit cell NLO properties per molecule, b_{IJK}, (using the β tensor and introducing the crystal symmetry of the structure of the salt). Lastly, the macroscopic optical properties are calculated using the Eq. 6.13 and Eq. 6.14 to yield the coefficients d_{IJK} (applying either the L-L or the W-B local field factors described in section 6.3.2).

Chapter 8

Phenylguanidine salt

The phenylguanidine is studied in this thesis because of its potential to form salts which may be interesting for nonlinear optics. However, the phenylguanidine unlike the guanidine is not a purely octupolar molecule. This property of the phenylguanidinium cation can be proved by calculating the dipolar, $\beta_{J=1}$, and octupolar component, $\beta_{J=3}$, explained in section 2.4.2. The calculations are show a scalar invariants of the vector of 89.05au and a scalar invariants of the septor of 221.18au. Therefore, $\rho = 2.48$ and this result demonstrates the weak octupolar character of the phenylguanidinium cation. The phenylguanidinium cation is

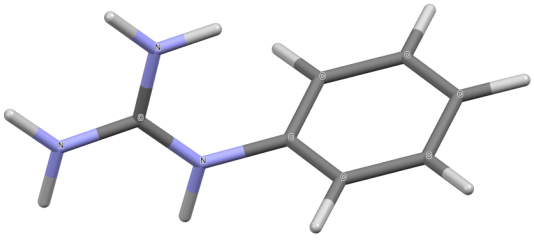

Figure 8.1: The phenylguanidinium cation after geometry optimization.

composed by a guanidinium group and a phenyl group and these are bonded by a N(guan)-C(phenyl) bond. Rotation around this single bond make the molecule flexible and different conformations may be found in the solid-state.

Some phenylguanidine salts have been studied by others like bis(phenylguanidinium) squarate [50] and bis(phenylguanidinium) carbonate monohydrate [51]. In this thesis a new salts are presented with phenylguanidinium cation.

8.1 Phenylguanidinium trifluoroacetate

The crystal structure of the salt phenylguanidinium trifluoroacetate (**pg1**) (see Fig. 8.2) is orthorhombic with the noncentrosymmetric space group $P2_12_12_1$.

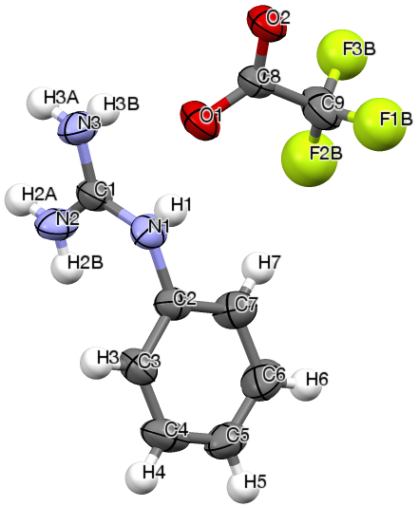

Figure 8.2: Asymmetric unit of phenylguanidinium trifluoroacetate, **pg1**. Displacement ellipsoids are drawn at the 50% probability level. For clarity, only the major disorder component is shown.

In the phenylguanidinium cation the torsion angle C1−N1−C2−C3 is 80.7(2)°. The -CF_3 group of the anion is rotationally disordered and the disorder was modeled over two sites with occupancies 0.517(12) and 0.483(12).

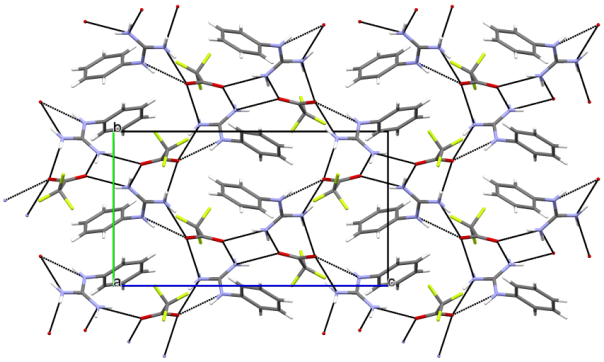

Figure 8.3: The packing of **pg1**, viewed down the *a* axis. Dashed lines denote hydrogen bonds. For clarity, only the major disorder component is shown.

The structure is stabilized by a network of N−H$\cdots$O hydrogen bonds between the anions and cations (Fig. 8.3, Table 8.1). All the hydrogen-bonding capability of the guanidinium group is used with each cation being linked to three anions. The only first-order hydrogen-bond motifs are noncyclic dimers with graph-set

Table 8.1: Hydrogen-bonding geometry (Å,°) of phenylguanidinium trifluoroacetate.

D−H$\cdots A$	D−H	H$\cdots A$	$D\cdots A$	D−H$\cdots A$
N1−H1$\cdots$O1	0.86	2.11	2.913(5)	155.5
N2−H2B$\cdots$O2^{i}	0.86	2.15	2.972(5)	161.1
N2−H2A$\cdots$O2^{ii}	0.86	2.10	2.932(5)	161.4
N3−H3A$\cdots$O1^{i}	0.86	2.18	2.982(5)	155.0
N3−H3B$\cdots$O1	0.86	2.25	3.013(6)	147.8

symmetry codes $i: -x+1/2, -y+1, z-1/2$;
$iii: -x, y+1/2, -z+1/2$.

$D_1^1(2)$. At the second level, there are chains with the graph-sets $C_2^2(8)$ and $C_2^1(6)$ and rings of descriptor $R_2^2(8)$ and $R_2^1(6)$ formed by anion/cation pairs.

The structure of **pg1** is remarkably similar to the structure of the salt phenylguanidinium chlorodifluoroacetate [52] as can be seen in a whole-lattice overlay of the two structures (see Fig. 8.4). The two salts crystalize in the same space group with similar unit cell parameters (**pg1**:a=7.5390(2)Å, b=9.1464(2)Å, c=16.2872(4)Å, V=1123.08(5)Å^3; phenylguanidinium chlorodifluoroacetate: a= 7.5239(1)Å, b=9.5722(2)Å, c=16.2316(3)Å, V=1169.00(4)Å^3)

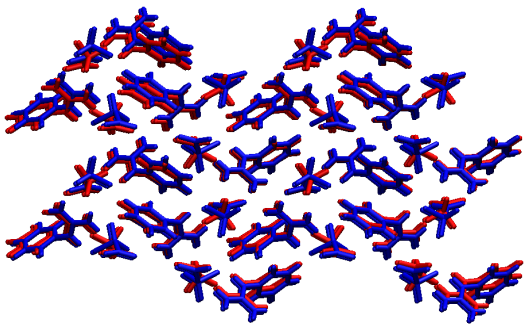

Figure 8.4: Whole-lattice overlay for the structures of phenylguanidinium chlorodifluoroacetate (blue) and **pg1** (red) viewed along the a axis (Software used for visualization: VMD, version 1.9.1, January 29, 2012 [1].

8.2 NLO properties of phenylguanidine salt

The crystal structure of the compounds phenylguanidinium trifluoroacetate and phenylguanidinium chlorodifluoroacetate **pg2** belongs to the Orthorhombic system with a noncentrosymmetric space group $P2_12_12_1$ and the crystals class is 222. With this crystal symmetries the second-order susceptibility tensor is of the form:

$$\begin{pmatrix} 0 & 0 & 0 & d_{14} & 0 & 0 \\ 0 & 0 & 0 & 0 & d_{25} & 0 \\ 0 & 0 & 0 & 0 & 0 & d_{36} \end{pmatrix} \tag{8.1}$$

Adding Kleinman permutation symmetry (in the section 2.3.3) we conclude that all components are equal, so the susceptibility depend only on the component d_{14} or, in other form, on d_{XYZ}.

8.2.1 Experimental Kurtz and Perry powder results

The SHG efficiency of the **pg1** and **pg2** were evaluated using the experimental Kurtz and Perry powder method.

The result were null in spite of the noncentrosymmetric molecular arrangement. Nevertheless, HF and DFT calculations were performed hoping to better understand the null response.

8.2.2 Computational nonlinear optical properties

The computational NLO calculations were performed for the phenylguanidine salt previously described (**pg1** salt), to get the molecular components of the hiperpolarizability tensor, β_{ijk}, and from this the macroscopic NLO coefficients, d_{IJK} and the angular average of the NLO susceptibility, $\langle d^{2\omega} \rangle$.

The same methodology applied in the guanidine salts in section 7.7.2, is implemented in the phenylguanidine salts. So let's begin by the analysis of elements of the molecular hiperpolarizability tensor, βijk, obtained from two different methods, HF and DFT with several functionals: there is a better agreement between the HF methods and DFT with LYP functional.

Table 8.2: The β_{ijk} components of the isolated molecule of phenylguanidinium trifluoroacetate, **pg1**, calculated HF method and DFT methods.

	pg1	
	β_{XXY}	β_{ZZZ}
HF	-78.7	172.5
LYP	-77.4	167.2
BHHLYP	-93.5	283.4
B3LYP	-115.0	870.8
BLYP	-182.1	9943.8

The values calculated using DFT-LYP were then used for the calculation of the macroscopic values.

The angular average of the NLO susceptibility obtained applying the W-B factors are 0.40 pm/V and the SHG efficiencies are 0.17 (**pg1**). However, the experimental result obtained with Kurtz and Perry powder method, in section 8.2.1, is zero and this discrepancy between experimental and computational methods can be justified by the low crystallinity of the material (that compromised the experimental result).

8.3 Experimental and computational methods

8.3.1 Single crystal X-ray diffraction

The determination of the phenylguanidine structure was carried out through of diffraction measurements performed with a $MoK\alpha$ radiation on a Bruker APEX II diffractometer [44]. All necessary corrections were applied in the collected (like Lorenz and polarization corrections) and the structures were solved with application of the direct methods and implementation of the refinement of the F^2s by full-matrix least-squares using SHELXS-97 and SHELXL-97 programs [21]. For non Hydrogen atoms in the structure anisotropic displacement parameters were applied, on the other hand the hydrogen atoms were placed at calculated positions and only were applied isotropic parameters.

The details of the crystal structure, the data collected and treatment applied are showed in the Table 8.3.

Table 8.3: The crystal details of the structure refinement and the data collected of the noncentrosymmetric structure of the phenylguanidinium trifluoroacetate, **pg1**.

Salt	**pg1**
Emp. formula	$C_9H_{10}F_3N_3O_2$
Formula weight	249.20
Temperature (K)	293(2)
Wavelength (Å)	0.71073
Crystal system	Orthorhombic
Space group	$P2_12_12_1$
a (Å)	7.5390(2)
b (Å)	9.1464(2)
c (Å)	16.2872(4)
$\alpha(^\circ)$	90
$\beta(^\circ)$	90
$\gamma(^\circ)$	90
Volume (Å^3)	1123.08(5)
Z	4
Calc. dens.(g/cm^3)	1.474
Abs. coef. (mm^{-1})	0.138
$F(000)$	512
data collec. range	2.55-28.77°
Index ranges:	$-10 < h < 9$,
	$-12 < k < 12$,
	$-21 < l < 21$
Reflections collected/unique:	21633 / 2757
R(int)	0.0302
Completeness (θ=25.00°)	99.6%
Refin. method	Full-matrix least-squares on F^2
Data/restraints/parameters	2757/0/154
F^2 Goodness-of-fit	1.037
R indices:	
final [$I > 2\sigma(I)$]	0.0806
wR_2	0.2402
all data	0.1110
wR_2	0.2699
Largest diff. peak and hole (eÅ^{-3})	0.617 / -0.427

Chapter 9

Triphenylguanidine salt

Triphenylguanidine salts may have nonlinear optics properties, since triphenylguanidine has octupolar character and may favous crystallization in a noncentrosymmetric structure.

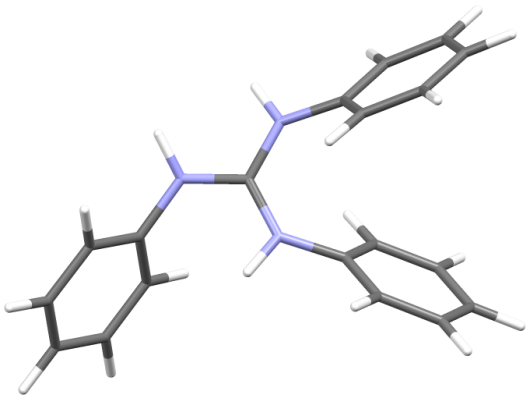

Figure 9.1: The triphenylguanidinium cation after optimization.

The octupolar character of the triphenylguanidinium cation can be calculated scalar invariants of the vector associated to dipole component is 72.25au and the scalar invariants of the septor associated to octupolar part is 435.44au. Therefore $\rho = 6.03$ that shows a octupolar character of triphenylguanidinium cation, but is obvious that this value is much lower than the value of $\rho = 3383.84$ obtained for guanidinium cation previously presented.

The *N*, *N*', *N*"-triphenylguanidinium cation is composed by guanidinium group (fragment CN_3 that presents a planar conformation). The three phenyl

groups bonded to the N atoms of the guanidinium group and are not coplanar with this plane. Each of this phenyl groups usually have different twist angles with guanidinium fragment and just as in the phenylguanidine this cation shows structural flexibility. Moreover, the triphenylguanidine as well as the guanidine and phenylguanidine have a great tendency to form many hydrogen bonds and this capability gives rise to strong crystal structures with several inter and intramolecular interaction that can be studied.

Some examples of the triphenylguanidine salts are *N*, *N*', *N*"- Triphenylguanidinium nitrate [53], *N*, *N*', *N*"- Triphenylguanidinium trifluoroacetate [54], *N*, *N*', *N*"- Triphenylguanidinium hydrogensulfate [55], and *N*, *N*', *N*"- Triphenylguanidinium bromide [56].

In the following sections, we will analyze only the nonlinear optical properties of the *N*, *N*', *N*"- Triphenylguanidinium cyanoacetate salt (see Fig. 9.2). The crystal structure of this salt was previously determined and study in other work [52].

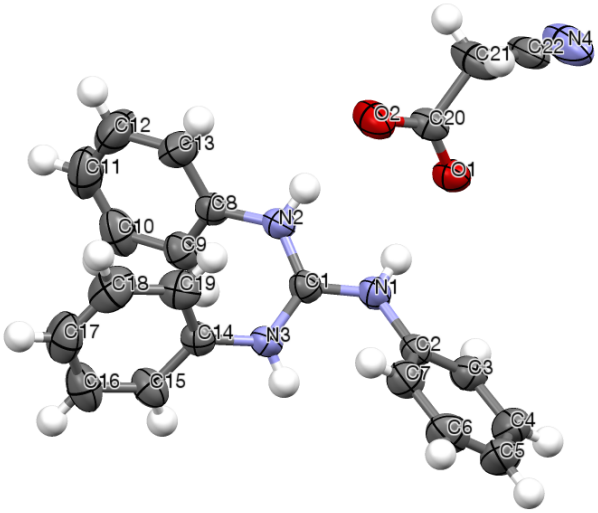

Figure 9.2: Asymmetric unit of Triphenylguanidinium cyanoacetate. Displacement ellipsoids are drawn at the 50% probability level.

9.1 NLO properties of triphenylguanidine salts

The Triphenylguanidinium cyanoacetate is a noncentrosymmetric salt that crystalize in the Orthorhombic system in a space group $P2_12_12_1$ (class 222), therefore the second-order susceptibility is given by:

$$\begin{pmatrix} 0 & 0 & 0 & d_{14} & 0 & 0 \\ 0 & 0 & 0 & 0 & d_{25} & 0 \\ 0 & 0 & 0 & 0 & 0 & d_{36} \end{pmatrix} \tag{9.1}$$

Once again the application of symmetry reduces the number of components in the matrix, however it is possible to further reduce the number of components, introducing the Kleinman permutation symmetry. In this case only the component d_14 (ord_{XYZ} in other notation).

9.1.1 Experimental Kurtz and Perry powder results

The result obtained for Triphenylguanidinium cyanoacetate from the Kurtz and Perry powder method for the SHG efficiency is 0.33 compared to the urea standard measured in the same conditions. This result is strongly affected by experimental conditions like a particle size and the conditions of the experimental setup.

9.1.2 Computational nonlinear optical properties

The computational calculations initially yields the components of the hiperpolarizability tensor, β_{ijk}, and from these we can arrive to the macroscopic NLO coefficients, d_{IJK}, like it has been done in sections 7.7.2 and 8.2.2.

Table 9.1 shows HF and DFT-LYP gives almost equal result. The elements of tensor d_{IJK} are then calculated with implementation of the Lorentz-Lorentz (L-L) and Wortmann-Bishop (W-B) models, previously explained in section 6.3.2. The results are presented in Table 9.2.

The SHG efficiency of the **tpg1** is evaluated from the results obtained using the LYP functional and applying Wortmann-Bishop local-field correction factors. From the computational result of the $\langle d^{2\omega} \rangle$ presented in Table 9.2 and comparing that value with the urea response we obtain the SHG efficiency of the 0.49 per

Table 9.1: The β_{ijk} components of the isolated molecules of triphenylguanidinium cyanoacetate ,**tpg1**, calculated using HF and DFT methods.

	% HF exchange	**tpg1**		
		β_{XXX}	β_{XXY}	β_{YYZ}
HF	100	-304.5	131.9	102.1
LYP	100	-300.9	129.9	-101.5
BHHLYP	50	-385.9	197.7	-150.5
B3LYP	20	-518.2	319.8	-221.3
BLYP	0	-518.5	320.0	-223.1

Table 9.2: Theoretical susceptibility components (pm/V) for **tpg1**, calculated from the β_{ijk} components of the isolated molecule using the LYP functional, with Lorenz-Lorentz (L-L) and Wortmann-Bishop (W-B) local-field factors.

	tpg1	
	d_{XYZ}	$\langle d \rangle$
L-L	-1.70	1.44
W-B	-1.34	1.13

Urea and was as stated above in section 9.1.1 the experimental result is 0.33. This shows a good agreement between the experimental and computational results.

9.1.3 Scalar invariants of the hiperpolarizability

The study of the octupolar character of the **tpg1** is show in Table 9.3.

Table 9.3: The values of the dipolar and octupolar components and the parameter ρ for asymmetric units of compounds **tpg1** and the corresponding anions and cations that are represented by **compound**$^-$ and **compound**$^+$, respectively.

Fragments	invariant vector	invariant septor	ρ
tpg1	393.57	478.48	1.22
tpg1$^+$	112.00	459.62	4.10
tpg1$^-$	136.65	180.81	1.32

The cation presents a octupolar behavior, but in the neutral molecule the components are similar and consequently the value of ρ is close to unity. The **tpg1** crystals has a space group $P2_12_12_1$ and the class is 222 such as referred previously and it is known that in this type of crystals the tensor,d_{ij} is compose

mainly by octupolar component of the asymmetric unit.

Chapter 10

Thiocyanuric salt

In this chapter we study the compound with thiocyanuric acid molecule in neutral and deprotonated form. This molecule is completely planar with a central cyanuric ring with hydrogen atoms in the most stable geometry were bonded to nitrogen atoms of the ring and the carbon atoms of the ring were bonded to sulfur atoms. This conformation of the thiocyanuric acid molecule present a trigonal symmetry, D_{3h}, such as the guanidinium cation. The trigonal symmetry presupposes the existence of an equilateral triangle formed by atoms of the molecule, where the symmetry elements are one 3-fold axis, 3 horizontal twofold axes, one horizontal plane and 3 vertical planes containing the horizontal axes [40].

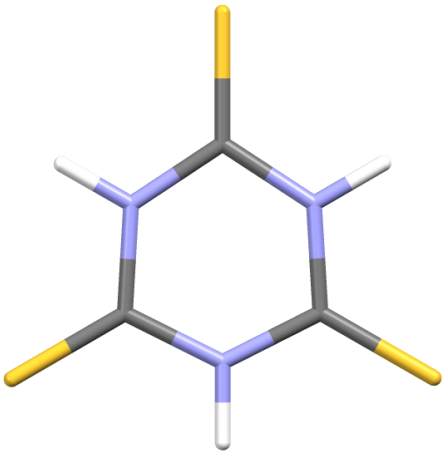

Figure 10.1: The thiocyanuric molecule after optimization.

The molecular symmetry of the thiocyanuric acid justifies the interest for NLO studies since this is a purely octupolar molecule. The octupolar behavior of the thiocyanuric molecule can be proved through the decomposition of the hiperpolarizability in the dipolar component ($\beta_{J=1}$) and octupolar component ($\beta_{J=3}$). For a optimized geometry the result for the scalar invariants of the vector associated to dipole component is 0.29au and the scalar invariants of the septor associated to octupolar part is of 1176.52au, yielding value of $\rho = 4083.21$ (strong octupolar character).

10.1 L-histidinium thiocyanurate thiocyanuric acid dihydrate

The crystal structure of the compound L-histidinium thiocyanurate thiocyanuric acid dihydrate (**thio1**) belongs to the monoclinic system with the noncentrosymmetric space group $P2_1$. The asymmetric unit consists of one L-histidinium cation, one neutral molecule of thiocyanuric acid (or trimercaptotriazine), one thiocyanurate anion and two water molecules (see Fig. 10.2).

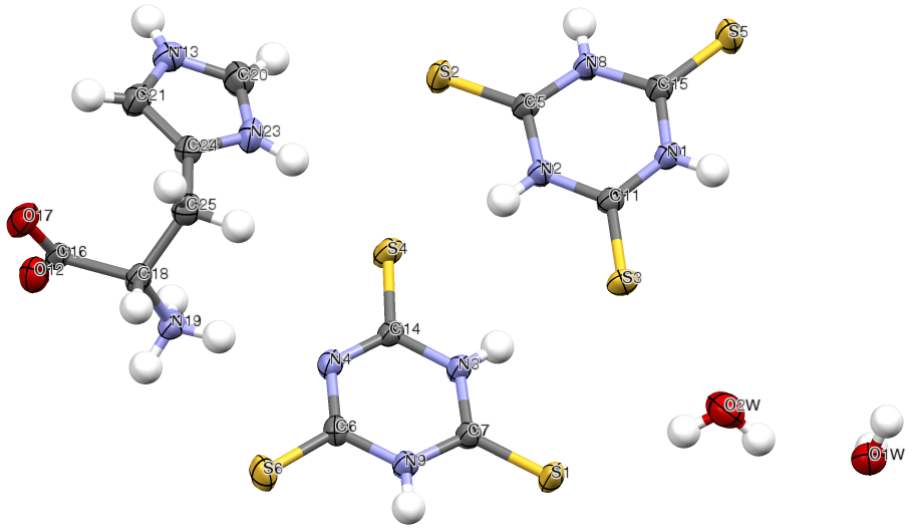

Figure 10.2: Asymmetric unit of L-histidinium thiocyanurate thiocyanuric acid dihydrate. Displacement ellipsoids are drawn at the 50% probability level.

The L-histidinium cation is in the zwitterionic form, with protonated and pos-

itively charged α-amino and imidazolium groups and a deprotonated and negatively charged α-carboxylate group. The side chain of the cation adopts a closed conformation (g^+) [57], with torsion angles ϕ^1[N1−C2−C3−C4]=71.5(3)° and ϕ^{21}[N5−C4−C3−C2]=-111.8(3)° [58].

The molecule of thiocyanuric acid is planar and has approximately the symmetry D_{3h}. This almost perfect trigonal symmetry implies that the molecular hiperpolarizability has an octupolar component ($\beta_{J=3}$) much higher than the dipolar part ($\beta_{J=1}$).

There is a large number of hydrogen bonds in this structure (see Table 10.1) forming an intricate 3D network.

Table 10.1: Hydrogen-bonding geometry (Å,°) of **thio1**.

D−H$\cdots A$	D−H	H$\cdots A$	$D\cdots A$	D−H$\cdots A$
N18−H18$\cdots$O1^{i}	0.86	2.58	3.299(3)	141.5
N18−H18$\cdots$O2^{i}	0.86	2.00	2.836(3)	162.1
N20−H20$\cdots$S2	0.86	2.35	3.1944(17)	168.8
N12−H12$\cdots$S6	0.86	2.57	3.4109(17)	166.8
N16−H16$\cdots$S3^{ii}	0.86	2.35	3.1977(17)	168.1
N14−H14$\cdots$S4^{iii}	0.86	2.56	3.4089(17)	171.8
O1W−H1A$\cdots$O1^{iv}	0.83	2.05	2.824(3)	156.0
O1W−H1B$\cdots$O2^{v}	0.93	2.10	3.030(3)	174.5
N7−H7$\cdots$O1W^{vi}	0.86	1.96	2.808(3)	167.7
C2−H2$\cdots$O1^{vii}	0.98	2.37	3.312(3)	160.4
N1−H1C$\cdots$N10	0.89	2.13	3.015(2)	179.2
N1−H1D$\cdots$O2W^{v}	0.89	1.92	2.810(3)	176.4
N1−H1E$\cdots$O2^{viii}	0.89	2.09	2.977(3)	176.1
C6−H6$\cdots$S1^{ii}	0.93	2.94	3.644(2)	133.8
C8−H8$\cdots$S5^{ix}	0.93	2.79	3.577(3)	142.6
O2W−H2A$\cdots$S3	0.85	2.56	3.398(2)	171.7
O2W−H2B$\cdots$O1W	0.85	2.13	2.906(3)	150.4
N5−H5$\cdots$S2	0.86	2.40	3.234(2)	163.0
C3−H3B$\cdots$S6^{iv}	0.97	2.81	3.491(2)	128.2

symmetry codes $i: x, y, z+1, -z+1/2; ii: x-1, y, z;$
$iii: x+1, y, z; iv: -x, y-1/2, -z; v: -x, y+1/2, -z$
$vi: x-1, y, z-1; vii: -x, y-1/2, -z-1;$
$viii: -x, y+1/2, -z-1; ix: x, y, z-1.$

The N−H$\cdots$S hydrogen bonds between the acid molecules and anions create

a two-dimensional zigzag ribbon structure with alternation of acid molecules and anions along the a axis . The cations are anchored to these ribbons by N−H$\cdots$S hydrogen bonds. N−H$\cdots$O between acid molecules and the cations link the ribbons leading to the formation of layers perpendicular to the b axis. N−H$\cdots$O hydrogen bonds between the cations and the water molecules form helical chains along the b axis and connect the layers.

10.2 NLO properties of thiocyanuric salts

The **thio1** compound crystalizes in a noncentrosymmetric structure with Monoclinic system, space group $P2_1$ with the associated class 2. Then, this crystal is a potential candidate to have a good nonlinear optical response. Through the analysis of all symmetry features is possible show the second-order susceptibility matrix of the form:

$$\begin{pmatrix} 0 & 0 & 0 & d_{14} & 0 & d_{16} \\ d_{21} & d_{22} & d_{23} & 0 & d_{25} & 0 \\ 0 & 0 & 0 & d_{34} & 0 & d_{36} \end{pmatrix} \tag{10.1}$$

Therefore, there are eight independent components with application of the symmetry, but applying the Kleinman permutation symmetry, explained in section 2.3.3, the number of the independent non zero elements of the matrix is reduced to the elements d_{YYY}, d_{YXX}, d_{YZZ} and d_{XYZ}.

10.2.1 Experimental Kurtz and Perry powder results

The Kurtz and Perry powder method is applied to evaluate the nonlinear optical response of this material yielding a SHG efficiency of 0.37 times Urea. This result shows a good optical response. The following sections are devoted to the calculation of the above value through *ab initio* methods.

10.2.2 Computational nonlinear optical properties

We have calculated the molecular hiperpolarizability tensor, βijk, of the isolated asymmetric unit of the **thio1** from several calculations using the HF and DFT method. The results of the components with higher values are presented in Table 10.2, for comparison purposes.

Table 10.2: β_{ijk} components of a cluster of molecules of L-histidinium thiocyanurate thiocyanuric acid dihydrate,**thio1**, calculated computationally with HF method and for some functionals of DFT method.

	% HF exchange	**thio1**	
		β_{XXX}	β_{XZZ}
HF	100	-111.4	268.0
LYP	100	-125.5	270.0
BHHLYP	50	-161.5	367.9
B3LYP	20	189.3	605.3
BLYP	0	1630.7	1618.7

As in the previous cases reported in this thesis, the values obtained are quite similar for HF and DFT-LYP. With the diminution of the percentage of the HF exchange, the calculated values increase by a factor of 10. Consecutive calculations are performed with DFT method and with LYP functional.

The calculations of d-matrix elements and the angular average of the NLO susceptibility were performed using the Lorentz-Lorentz (L-L) and Wortmann-Bishop (W-B) models (explain in section 6.3.2).

Table 10.3: Theoretical susceptibility components (pm/V) for **thio1**, calculated from the β_{ijk} components of the isolated molecule using the LYP functional, with Lorentz-Lorentz (L-L) and Wortmann-Bishop (W-B) local-field factors.

	thio1				
	d_{YXX}	d_{YZZ}	d_{YYY}	d_{XYZ}	$\langle d \rangle$
L-L	-0.21	0.64	-0.15	2.63	2.26
W-B	-0.65	0.12	0.02	1.96	1.71

Once again the average value $\langle d \rangle$ is large when the local field factor (essentially a correction for the difference between the applied field that would be felt by the molecule in the free space and the actual local field felt inside the material) is the

simplest Lorenz-Lorentz spherical cavity factor. When the more sophisticated Wortmann and Bishop model is used, lower values are obtained. These lower values are more concordant with the experimental ones. With the Wortmann-Bishop local-field correction factors the SHG efficiencies is 0.74 per Urea. On the other hand, the experimental result is 0.37 times Urea, such as referred in section 10.2.1. These results show some concordance between the experimental methodology using the K-P powder method and the chosen computational approach.

10.2.3 Scalar invariants of the hiperpolarizability

The calculated values of the invariant vector, sector and ρ show an huge octupolar character when in the neutral form, but such character diminishes abruptly upon deprotonation.

Table 10.4: The values of the dipolar and octupolar components and the parameter ρ for asymmetric units of compounds **thio1** and the corresponding anions and cations.

Fragments	invariant vector	invariant septor	ρ
thio1	157.69	598.05	3.79
Thiocyanuric	24.69	1139.71	46.16
Thiocyanurate	400.88	1346.02	3.36
L-histidinium	260.33	109.98	0.42

Table 10.5: The β_{ijk} components of isolated thiocyanuric acid molecule and thiocyanurate anion obtained from the calculations (LYP functional).

	Thiocyanuric acid			Thiocyanurate anion		
	X	Y	Z	X	Y	Z
XX	464.80	-38.56	324.19	-799.61	39.02	-310.90
YY	-5.34	0.65	-5.11	-0.62	-0.12	-7.62
ZZ	-456.72	41.43	-343.37	563.37	-29.10	-4.76

This is evident in table above: the elements of molecular hiperpolarizability in the neutral form satisfy the following conditions $\beta_{XXX} \approx \beta_{XZZ}$, $\beta_{ZXX} \approx \beta_{ZZZ}$, $\beta_{XYY} \approx \beta_{ZYY}$ and $\beta_{YXX} \approx \beta_{YZZ}$, but for thiocyanurate anion the dipolar

component break these relations. So the parameter ρ decrease with the loss of symmetry.

Finally, in Table 10.4 it is shown that the l-histidinium anion present a strong dipolar behavior since the ρ parameter is lower than unity, on the other hand the asymmetric unit with the conjugation of all molecules has an overall octupolar character.

10.3 Experimental and computational methods

10.3.1 Single crystal X-ray diffraction

The crystal structure of **thio1** was determined using the X-ray data collected on a Bruker APEX II single crystal diffractometer, at the room temperature with $MoK\alpha$ radiation. The structure was solved by direct methods as implemented in SHELXS-97 and refined by full-matrix least-squares using SHELXS-97. The refinement was done allowing the non H-atoms to freely refine with anisotropic displacement parameters. The H-atoms were constrained to ride on their "parent atoms" with isotropic displacement parameters. the Table 10.6.

Table 10.6: The crystal details of the structure refinement and the data collected of the noncentrosymmetric structure of the L-histidinium thiocyanurate thiocyanuric acid dihydrate, **thio1**.

Salt	**thio1**
Emp. formula	$C_{12}H_{19}N_9O_4S_6$
Formula weight	545.72
Temperature (K)	293(2)
Wavelength (Å)	0.71073
Crystal system	Monoclinic
Space group	$P2_1$
a (Å)	11.3096(2)
b (Å)	6.94250(10)
c (Å)	14.2779(3)
$\alpha(^\circ)$	90
$\beta(^\circ)$	98.9193(9)
$\gamma(^\circ)$	90
Volume (Å^3)	1107.50(3)
Z	2
Calc. dens.(g/cm^3)	1.636
Abs. coef. (mm^{-1})	0.659
$F(000)$	564
data collec. range	1.44-28.32°
Index ranges:	$-15 < h < 15$,
	$-9 < k < 9$,
	$-18 < l < 19$
Reflections collected/unique:	28225 / 5501
R(int)	0.0183
Completeness (θ=25.00°)	99.9%
Refin. method	
Full-matrix least-squares on F^2	
Data/restraints/parameters	5501/0/281
F^2 Goodness-of-fit	1.036
R indices:	
final [$I > 2\sigma(I)$]	0.0239
wR_2	0.0656
all data	0.0263
wR_2	0.0674
Largest diff. peak and hole (eÅ^{-3})	0.273 / -0.197

Chapter 11

Charge density of triphenylguanidine salts

In this chapter we will study the charge density distribution of some triphenylguanidine crystals using the results of the X-ray diffraction experiments at low temperature. The charge density distribution of the triphenylguanidine molecule in the neutral and cationic form is obtained from the implementation of the multipole refinement. An important part of this study is carried out by analyzing the topology of the charge density taking into account the main interactions in each system.

The triphenylguanidine (**tpg**) has three electron donor atoms with two amino groups, $-NH$ and one imine group $= N$. The nitrogen atoms of the guanidine fragment, CN_3 with Y-conjugation, shows strong donor ability that changes with the organic substituents and for crystal environment. Its H-banding ability may be explored, in charge density distributions with especial attention to the inter and intra-molecular interactions [59]. The study of electron density is not restricted to the guanidine fragment, is may also be interesting to analyze the behavior of the charge density distribution in the three aromatic rings of the **tpg**.

The first structural study was performed in 1988 [60] for a **tpg** crystal with orthorhombic symmetry. Later on, it was discovered and studied a new polymorph of the **tpg** that crystallizes in a monoclinic phase [61]. The **tpg** molecule can be easily protonated and in this form shows a great ability to form ionic crystals with

many acids like in the salts: *N*, *N*', *N*"- Triphenylguanidinium chloride [62], *N*, *N*', *N*"- Triphenylguanidinium bromide [63], *N*, *N*', *N*"- Triphenylguanidinium nitrate [64], *N*, *N*', *N*"- Triphenylguanidinium hydrogensulfate [65], *N*, *N*', *N*"- Triphenylguanidinium 5-nitro-2, 4-dioxo-1, 2, 3, 4-tetrahydropyrimidin-1-ide [66], and others.

Of these set of ionic crystals the *N*, *N*', *N*"-Triphenylguanidinium trifluoroacetate, **tpgtfa**, was chosen. In the **tpgtfa** crystal we will study the interaction within the triphenylguanidinium cation and of the trifluoroacetate anion, and the interaction between these ions. In the following section we will discuss the crystal structure of the **tpg** and **tpgtfa** and the principal differences between structures obtained at room temperature and low temperature. A previous structural study was reported on ref [67].

11.1 Molecular structures

The determination of the charge density distribution is only possible if it is known beforehand the molecular structure of the crystals and the symmetries in each crystal. The structures of **tpg** and **tpgtfa** are determined in the literature at room temperature [61; 67], but at low temperatures the structure suffer some variations that can be quite important for the correct application of multipole refinement. The monoclinic polymorph of **tpg** is defined with a centrosymmetric space group $P2_1/c$. In the crystal chains are formed parallel to the c axis through weak hydrogen bonds with one of the amino groups and the imine group nitrogen atom (Fig. 11.1, Table 11.1). The guanidine CN_3 fragment, in the **tpg** molecule, is a planar group but the C_{aryl} atoms are not coplanar with such fragment.

Table 11.1: Hydrogen-bonding geometry (Å,°) of monoclinic polymorph of **tpg** at temperature $30K$.

D−H$\cdots A$	D−H	H$\cdots A$	$D\cdots A$	D−H$\cdots A$
N1−H1$\cdots$N3^i	0.88	2.14	3.003(2)	165.7
C3−H3$\cdots$N3	0.95	2.51	3.027(2)	114.5

symmetry codes $i : x, -y + 1/2, z + 1/2$.

The parameters of the crystal structure at low temperature presents a quite

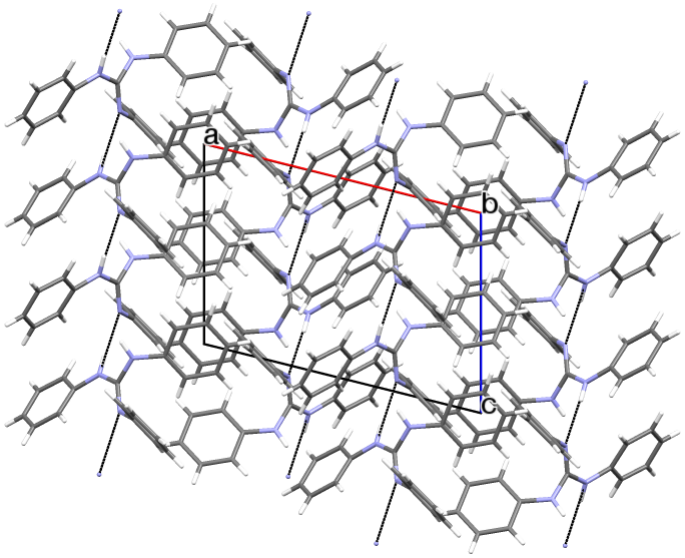

Figure 11.1: Packing diagram of the monoclinic polymorph with the H-bonds drawn as dashed lines. H atoms not involved in hydrogen bonding have been omitted for clarity.

evident variation. Generally, the cell parameters of the network have a tendency to decrease at low temperature, mainly due to the decrease in thermal vibration of the atoms of the structure. The comparison of the unit cell parameters is showed in the Table 11.2.

Table 11.2: The unit cell parameters (Å) of the monoclinic polymorph of **tpg** at the room temperature and at low temperature ($30K$).

	Low temperature	Room temperature
a	12.4789(11)	12.4060(4)
b	14.2304(14)	15.1653(6)
c	8.7425(8)	8.7028(3)

The analysis of the unit cell axes shows that the axes a and c remain fairly constant and the axis b has a great decrease, approximately 0.9Å. This variation in unit cell parameters proves the great anisotropy in the loss of cell volume with temperature. So, this uneven compression in the structure leads to uneven changes in the bond lengths. We can compare the various lengths at different temperatures using two-dimensional fingerprint plots [68; 69] of the **tpg**. This

plots are obtained from the surface of Hirshfeld [70; 71] , calculating the internal distance to the surface, d_i and the distance external , d_e, which measure the distance from the surface for the atoms of the neighboring molecules . The 2D-fingerprint plots are obtained using the software CrystalExplorer, version 3.1 [72] and are presented in the Fig. 11.2.

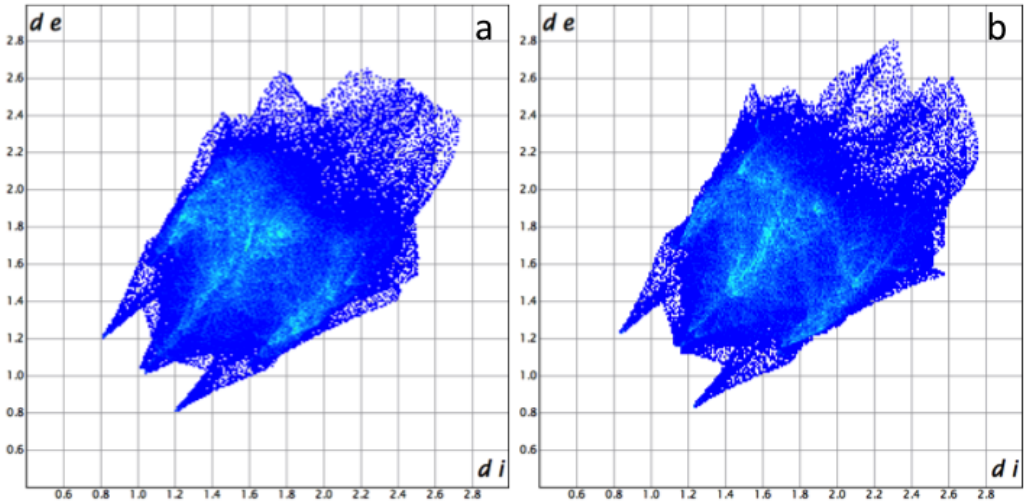

Figure 11.2: Two-dimensional fingerprint plots of the monoclinic phase of the **tpg** at low temperature (a) and at room temperature(b).

These finger print plots show the obvious reduction of the bond lengths in the low temperature structure. We can see this since all the fingerprint is shifted to lower values of d_i and d_e. One of the main differences is associated to the central hump in the region with d_i and d_e of about 1.0Å that is more pronounced in low temperature structure. The other differences are presents in profiles of the long range interactions for larger values of d_i and d_e defined by interactions between H$\cdots$H and C$\cdots$H.

The *N*, *N*', *N*"-Triphenylguanidinium trifluoroacetate, **tpgtfa**, which corresponds to an ionic crystal composed by one cation of triphenylguanidinium and one anion of trifluoroacetate, is shown in Fig. 11.3. This structure crystalize in a monoclinic form with the centrosymmetric space group $P2_1/c$.

These anion is a very strong carboxylic acid due to the charge transference of the F atoms for the C atom. Therefore, the structures with this anion show

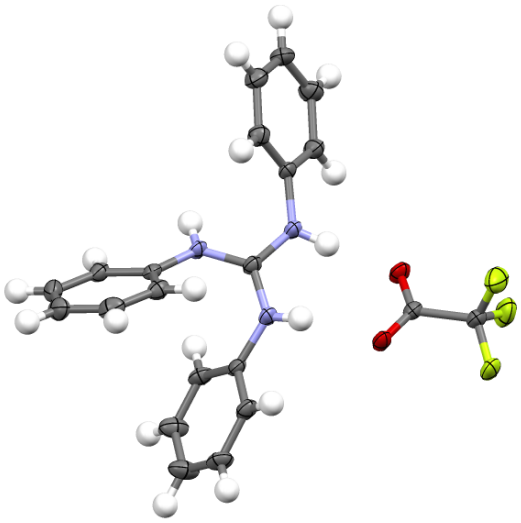

Figure 11.3: Asymmetric unit of **tpgtfa** at low temperature (120k). Displacement ellipsoids are drawn at the 50% probability level.

a tendency to form crystals with phase transitions and superstructures. In this ionic crystals, at room temperature, the CF_3 group presents a rotational disorder. Theoretical calculations have shown that the rotation energy barrier of the disordered group is low [67].

Furthermore, this crystal also presents superstructures formed by chains parallel to the c axis assembled from hydrogen bonds between amino groups of the triphenylguanidinium (Fig. 11.4) and the O atoms of the carboxylic group of trifluoroacetate (the set of the hydrogen bonds of this structure at low temperature are presented in the Table 11.3).

Table 11.3: Hydrogen-bonding geometry (Å,°) of **tpgtfa** at the temperature of 120k.

D−H$\cdots A$	D−H	H$\cdots A$	$D\cdots A$	D−HA
N1−H1$\cdots$O1	0.88	1.87	2.7509(18)	178.5
N2−H2$\cdots$O2^i	0.88	1.97	2.8305(17)	164.4
N2−H2$\cdots$F1	0.88	2.55	3.0206(17)	114.0
N3−H3$\cdots$O2^i	0.88	2.01	2.8040(18)	150.0

symmetry codes $i : x, -y + 1/2, z - 1/2$.

The parameters of unit cell of the **tpgtfa** at low temperature shows a variation, that is displayed in Table 11.4.

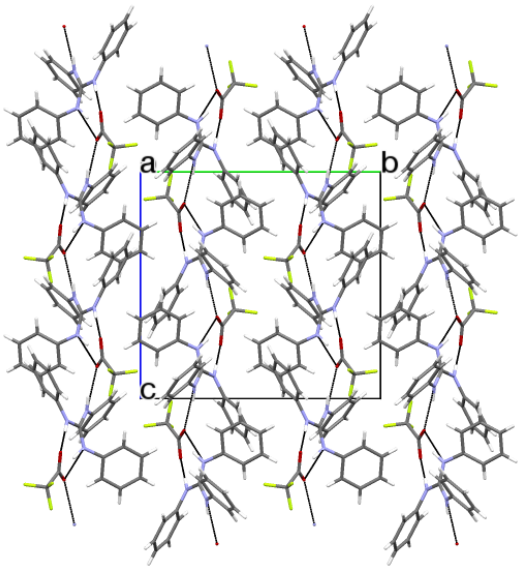

Figure 11.4: Packing diagram of the **tpgtfa** at low temperature with the H-bonds drawn as dashed lines.

Table 11.4: The unit cell parameters (Å) of the **tpgtfa** at the room temperature and at low temperature ($120K$).

	Low temperature	Room temperature
a	9.9447(6)	9.9905(8)
b	14.5037(9)	14.9348(13)
c	14.1147(9)	14.1194(10)

Datermination of the unit cell axes shows that the greater decrease is in b axis (of about 0.4Å). On the other hand the c axis remains approximately constant with a small decrease of 0.005Å and the a axis undergoes a very small decrease of approximately 0.05Å. This variation on the unit cell parameters proves the anisotropy in the loss of volume with temperature.

The variations of the bond lengths are analyzed again using the two-dimensional fingerprint plots through the same strategy previously used for **tpg**. These plots are presented in the Fig. 11.5 for the structures at room temperature and at low temperature and show the obvious reduction of the bond lengths in the low temperature structure. This change corresponds to a translation of the plot points to lower values of d_i and d_e. Furthermore, the analysis of shorter interactions

with lower values of d_i and d_e shows a set of peaks associated to the several interactions. The central peak of the H$\cdots$H interactions with values of d_i and d_e about 1.1Å for two temperatures has different profiles. At low temperature, there are higher concentration of points in this peak making it broadest.The other two symmetrical peaks more pronounced with values of d_i = 0.7Å and d_e between 1.1 and 1.0Å for structure at low temperature are defined by interactions between O$\cdots$H. These peaks have the same profile, but the low temperature have a more concentration of points and is more "compact". The interaction C$\cdots$H is associated to the smaller peak, with values of d_i and d_e about 1.1Å and 1.6Å , respectively. These peaks are better defined at low temperature (having a thin peak profile), while at room temperature they are more similar to a hump. The other important difference is in the region of the lighter color with values of d_i and d_e of approximately 1.5Å for both, due the interaction between the F atoms and all the others. This region, at room temperature, corresponds to an undefined, but at low temperature we can distinguish three peaks. This difference is explained by the disappearance of the disorder in the F atoms group.

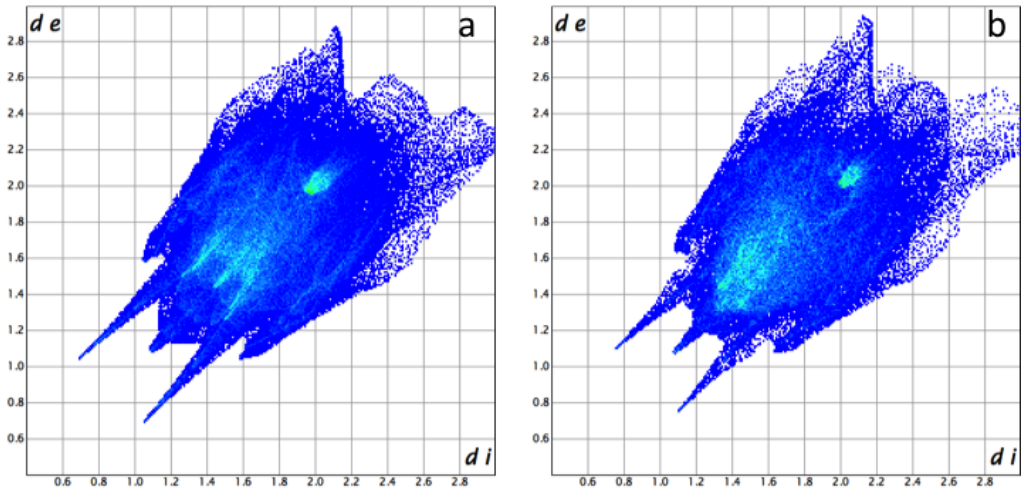

Figure 11.5: Two-dimensional fingerprint plots of the **tpgtfa** at low temperature (a) and at room temperature (b).

The structures presented in this chapter were previously solved using direct methods implemented in SHELXS-97 program and refined on F^2s by full-matrix least-squares with SHELXL-97 program [21]. These data were obtained from

Table 11.5: The crystal details of the structure refinement and the data collected at low temperature of the Triphenylguanidine, **tpg**, and *N*, *N*', *N*"-Triphenylguanidinium trifluoroacetate, **tpgtfa**.

Salt	**tpg**	**tpgtfa**
Emp. formula	$C_{19}H_{17}N_3$	$C_{21}H_{18}F_3N_3O_2$
Formula weight	287.35	401.38
Temperature (K)	30(2)	120(2)
Wavelength (Å)	0.71073	0.71073
Crystal system	Monoclinic	Monoclinic
Space group	$P2_1/c$	$P2_1/c$
a (Å)	12.4789(11)	9.9447(6)
b (Å)	14.2304(14)	14.5037(9)
c (Å)	8.7425(8)	14.1147(9)
$\alpha(^\circ)$	90	90
$\beta(^\circ)$	104.003(6)	104.159(4)
$\gamma(^\circ)$	90	90
Volume (Å^3)	1506.4(2)	1974.0(2)
Z	4	4
Calc. dens.(g/cm^3)	1.267	1.351
Abs. coef. (mm^{-1})	0.076	0.108
Extinction coef.	-	-
$F(000)$	608	832
data collec. range	1.682-27.912°	2.046-27.915°
Index ranges:	$-14 < h < 16$, $-18 < k < 17$, $-11 < l < 10$	$-13 < h < 13$, $-19 < k < 19$, $-18 < l < 18$
Reflections collected/unique:	10897 / 3459	33884 / 4717
R(int)	0.0659	0.0595
Completeness (θ=25.00°)	98.9%	100%
Refin. method Full-matrix least-squares on F^2		
Data/restraints/parameters	3459/0/199	4717/0/262
F^2 Goodness-of-fit	1.027	1.020
R indices:		
final [$I > 2\sigma(I)$]	0.0566	0.0452
wR_2	0.1166	0.0991
all data	0.1037	0.0815
wR_2	0.1345	0.1141
Largest diff. peak and hole (eÅ^{-3})	0.494 / -0.513	0.485 / -0.338

the experimental X-ray diffraction performed with a fourcircle diffractometers with k geometry resorting to a Bruker-Nonius Kappa Apex II. The APEX II diffractometer uses the radiation Mo Kα with a wavelength $\lambda = 0.71073$ Å and the detection is performed using a Charge-Coupled Device (CCD) with 4096×4096 pixels, each pixel with a dimension 15μm$\times 15\mu$m. For charge density studies, it is necessary to use X-ray diffraction data collected at low temperature that were measured using the N-HeliX from Oxford Cryosystems with a dual flow nitrogen and helium cooler. It allows experiments with the APEX II diffractometer with sample temperatures between 28-300K. Parameters of the data collection and crystal structure presented in Table 11.5.

11.2 Multipole refinement strategy

The multipole refinement is implemented using the program XD2006 [73] with the structures presented in the preceding section. The structures of **tpg** and **tpgtfa** at low temperature were solved using the SHELXL program and these results allow us to begin the multipolar refinement explained in chapter 5. We begin by remaking the IAM refinement using the XD program as a first approximation to the charge density of the molecules and this procedure enables us to refine positions, thermal displacement parameters and scale factor.

Then, the multipolar refinement is implemented starting with the definition of sets of atoms in structure with the same k parameter and the chemical equivalents. The multipoles are applied in stages and according with the local symmetries of each atom in the molecules. In the next sections we will present in detail the strategy applied to each of the studied structures.

11.2.1 tpg strategy

The strategy applied in the **tpg** crystal has as first objective the description of the chemical equivalents in the structure to reduce the number of independent parameters. So, the atoms, assumed as equivalent, should be associated to the same chemical environment, only taking into account the nearest neighbors. Thus, in the guanidine fragment two chemical constraints are applied in the two amino groups:

$$\begin{aligned} N(1) &= N(2) \\ H(1) &= H(2) \end{aligned} \tag{11.1}$$

In the phenyl groups the C atoms are considered chemically equivalent, except the *ipso* C atom bonded to N atoms. The definition of these equivalences is equal for the three phenyl groups. All Hydrogens of these rings are considered as

chemical equivalents.

$$C(3) = C(4) = C(5) = C(6) = C(7) \tag{11.2}$$
$$C(9) = C(10) = C(11) = C(12) = C(13)$$
$$C(15) = C(16) = C(17) = C(18) = C(19)$$

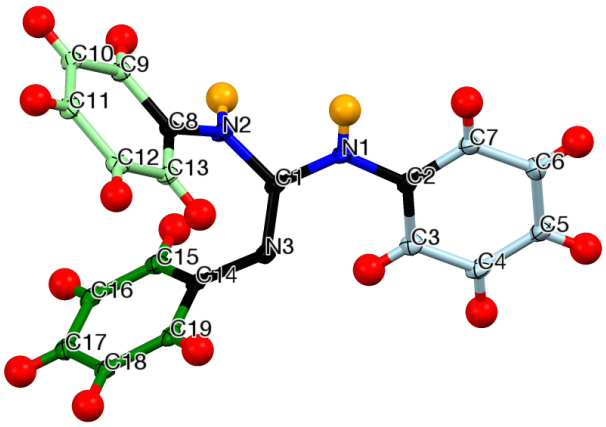

Figure 11.6: The atoms of the **tpg** molecule with each color representing the group of chemical equivalent atoms. The atoms with black color correspond to the atoms without chemical equivalents.

The atoms in a multipole refinement are associated with the expansion and contraction parameters k and k'. The number of parameters can be reduced by defining sets of atoms with the same values of the k and k' parameters. The sets of k defined for the **tpg** structure are:

N(1) and N(2)	k set 1
N(3)	k set 2
C(1)	k set 3
C(2), C(8) and C(14)	k sets 4 ,6 and 8
C(3) – C(7)	k set 5
C(9) – C(13)	k set 7
C(15) – C(19)	k set 9
H(1) and H(2)	k set 10
Other Hs	k set 11

The local symmetries are applied in the atoms of the **tpg** molecule taking into account the atom and its closest neighbors. So, in the central C atom of the guanidine fragment and in the three N atoms it was applied the $mm2$ symmetry. In the C atoms of the phenyl groups the m symmetry or planar symmetry was applied . The local symmetries are an important part of the multipole refinement because they restrict the number of multipole functions that we can refine and so the number of parameters is reduced even further.

Then, before the application of the IAM and starting from these results, κ parameters are applied and several chemical equivalences are imposed such as described previously and all non-hydrogen atoms are refined together with P_V and κ. After this refinement, the local symmetries are introduced and with them are defined the sets of P_{lm} functions that we will refine. Together with these parameters the κ' parameters are introduced using the theoretical values from the multipole refinements of theoretical structure factors [74] (this parameter is fixed during the refinement). Then the positional and thermal parameters are refined along with P_V and P_{lm} for all non-hydrogen atoms. Lastly, all parameters are refined with exception for the κ' parameter and the final results of the multipolar refinement are obtained.

11.2.1.1 Refinement results

The analysis of the multipolar refinement is an important indicator of the quality of the model. The R-factor shows how good is the adjustment of the model applied to the data and is presented in Table 11.6.

Table 11.6: The statistics of the fitting applied in the multipole refinement of **tpg**.

Model	R	R_ω	GOF	$N_{data}/N_{parameters}$
Spherical refinement (in XD)	0.070	0.055	1.309	148.81
MM, with dipoles	0.067	0.052	1.250	30.79
MM, with quadrupoles	0.066	0.051	1.224	28.69
MM, with octupoles	0.062	0.048	1.159	26.75
MM, with hexadecapoles	0.062	0.048	1.157	24.72

The results obtained show the decrease of the R-factor with introduction of

the aspherical model, so it is verified that the R-factor decrease by increasing the multipolar level of the functions. On the other hand, the Goodness of Fit decreases along the refinement tending to 1. Finally, the ratio of data to the number of parameters in refinement shows the increase of parameters that allows a better adjustment of the model to the experimental data, which is verified with the decrease of the R-factor.

After the multipole refinement we can analyze the residual density maps of the guanidine fragment and the phenyl fragment presented in Fig. 11.7.

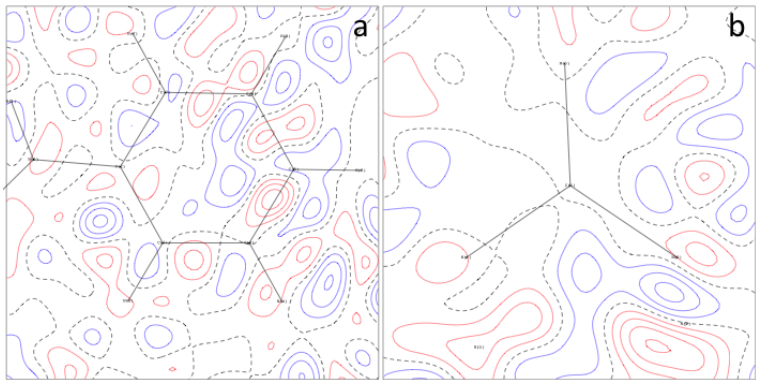

Figure 11.7: The residual density maps after multipole refinement in a **tpg** phenyl ring (a) and in the guanidine fragment (b). The red and blue solid contour lines represent the positive and negative contours, respectively, and the black dashed contours represent the lines with zero residual density. Step width is $0.1e\text{Å}^{-3}$.

In these maps, residual density is distributed randomly, such as expected, between -0.344 and $0.415e\text{Å}^{-3}$ showing that the model applied is good for the description of the structure. Furthermore, the analysis of the DMSDAs (Differences of Mean-Squares Displacement Amplitudes) after the multipole refinement show that these are much lower than those obtained with spherical refinement, the highest amplitude is $7.0 \cdot 10^{-3}\text{Å}^2$ associated to the N(1) atom of the guanidine fragment.

11.2.2 tpgtfa strategy

The same strategy used in the **tpg** structure was implemented in the **tpgtfa**. So, two chemical constraints were applied in the fragment of guanidine taking into

account the difference between the triphenylguanidine molecule and the triphenylguanidinium cation:

$$N(1) = N(2) = N(3) \qquad (11.3)$$
$$H(1) = H(2) = H(3)$$

The three phenyl rings exhibit the same conformation in the two compounds, therefore the same chemical equivalents were applied in the two compounds. Similarly, all H atoms of the rings were considered as the same chemical equivalents. Finally, in the trifluoroacetate anion were defined two more chemical equivalents:

$$O(1) = O(2) \qquad (11.4)$$
$$F(1) = F(2) = F(3)$$

All chemical equivalents are summarized, in a more easily understandable form, in Fig. 11.8.

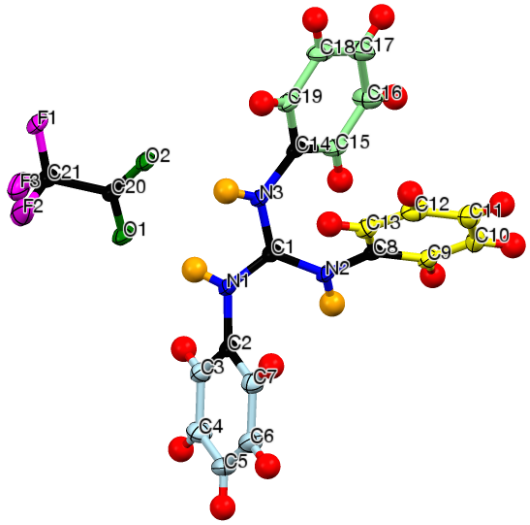

Figure 11.8: The atoms of the **tpgtfa** with the same color represent a group of chemical equivalents atoms. The atoms with black color correspond to the atoms without chemical equivalents.

The atoms are associated to the expansion parameters k and k'. So, the sets of k defined for the **tpgtfa** structure are:

F(1), F(2) and F(3)	k set 1
O(1) and O(2)	k set 2
N(1), N(2) and N(3)	k set 3
C(1)	k set 4
C(2), C(8) and C(14)	k sets 5 ,7 and 9
C(3) – C(7)	k set 6
C(9) – C(13)	k set 8
C(15) – C(19)	k set 10
C(21) and C(22)	k set 11 and 12
H(1) and H(2) and H(3)	k set 13
Other Hs	k set 14

The local symmetries were applied to the atoms of **tpgtfa** in the same way as in the **tpg**, with the exception of the central C atom of the guanidinium fragment. In this C atom the $3m$ symmetry is applied, to which are associated three planes defining its neighboring atoms. Furthermore, in the trifluoroacetate anion the local symmetries are applied initially to the F atoms by imposing the planar symmetry m and the same is applied to the O atoms. On the other hand, in the C atom bonded to the F atoms the $3m$ local symmetry is defined and finally, for the C atom of the carboxylic group, the $mm2$ symmetry is applied. The sequence used to introduce the parameters in the refinement and the parameters that are refined in the **tpgtfa** is the same used in **tpg** and was described in section 11.2.1.

11.2.2.1 Refinement results

The analysis of the multipole refinement applied in the **tpgtfa** structure is an important indicator of the quality of the model described in the previous section. The first results analysed are the statistics results that shows the adjustment of the model applied to the data and are presented in Table 11.7.

The results presented in Table 11.7 show the decrease of the R-factor with introduction of the aspherical model. Furthermore, the R-factor decreases with increasing multipolar level of functions. On the other hand the Goodness of Fit shows the decreases along the refinement tending to 1. Lastly, the ratio of data to refinement parameters shows the increase in parameters and hence the increase in the complexity of the refinement model and in TGPTFA this ratio is much smaller than in **tpg**.

Table 11.7: The statistics of the fitting applied in the multipole refinement of **tpgtfa**.

Model	R	R_ω	GOF	$N_{data}/N_{parameters}$
Spherical refinement (in XD)	0.070	0.055	1.309	848.42
MM, with dipoles	0.058	0.041	1.324	73.53
MM, with quadrupoles	0.057	0.040	1.283	69.37
MM, with octupoles	0.055	0.038	1.231	65.26
MM, with hexadecapoles	0.055	0.038	1.230	61.62

After the multipole refinement we can analyze the residual density maps of the guanidinium fragment, of one phenyl fragment in the triphenylguanidinium cation and also the carboxylate group and the plane of F atoms of the anion presented in Fig. 11.9.

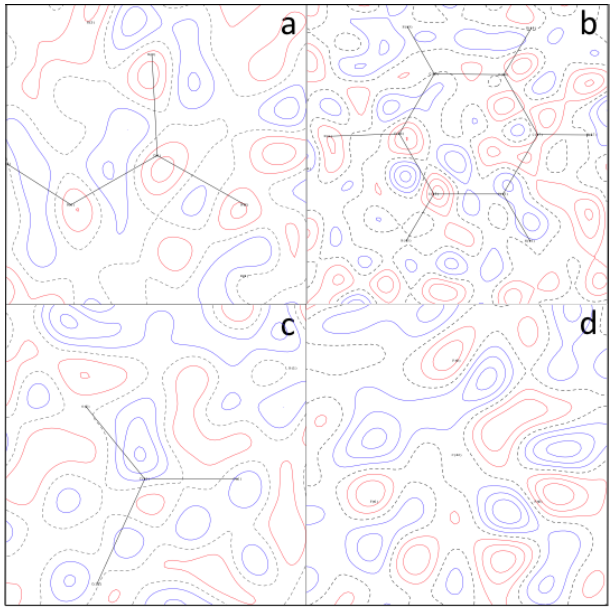

Figure 11.9: The residual density maps after multipole refinement in the **tpgtfa** guanidinium fragment (a), one phenyl ring (b), the carboxylate group (c) and the plane of F atoms (d). The red and blue solid contours lines represent the positive and negative contours respectively and the black dashed contours represent the lines with zero residual density. Step width is $0.1e\text{Å}^{-3}$.

In this residual density maps of the **tpgtfa** we can see that the residues are distributed randomly as expected and the residual density is between -0.399

and $0.439e\text{Å}^{-3}$ showing that the model applied is good for the description of the **tpgtfa** structure. The analysis of the DMSDAs, after the multipole refinement, shows that these are much lower than the ones obtained with spherical refinement such as in the multipole refinement of **tpg**. The highest DMSDAs is $4.3 \cdot 10^{-3}\text{Å}^2$, associated to the N(3) atom of the guanidinium fragment.

11.3 Discussion of charge density properties

The properties of the charge density can be studied from the results obtained with the application of the multipole refinement and in this way we can analyze the deformation density, the electrostatic potential, the features of the critical points and other properties described in section 3.4. In the following sections we will analyze and compare the results of the two structures studied and the experimental results of the properties are compared with theoretical results.

These theoretical results are obtained using optimized geometries of the **tpg** and **tpgtfa** and calculating the wave functions of the structures using the software package GAMESS US [45]. The analysis of these wave functions and calculation of properties was performed with the software package Multiwfn version 3.3.7 [75; 76].

11.3.1 Deformation of the charge density

The deformation density shows the difference between densities obtained from the multipolar model and the conventional spherical model. It is expected that the deformation density will show a non-spherical component of the charge density. So it is predictable to see the concentration of charge density along the bonds, the lone-pairs and other interactions in structures. In the **tpg** crystal we study the static deformation density of the experimental and theoretical results of the guanidine fragment and phenyl rings. These results are presented in Fig. 11.10.

The static deformation density shows the concentration of electron density along the bonds, which is neglected in the conventional spherical model and, on the other hand, it is verified the depletion of the electronic density in the core of the atoms. So, in the aspherical density the charge is "taken" from the

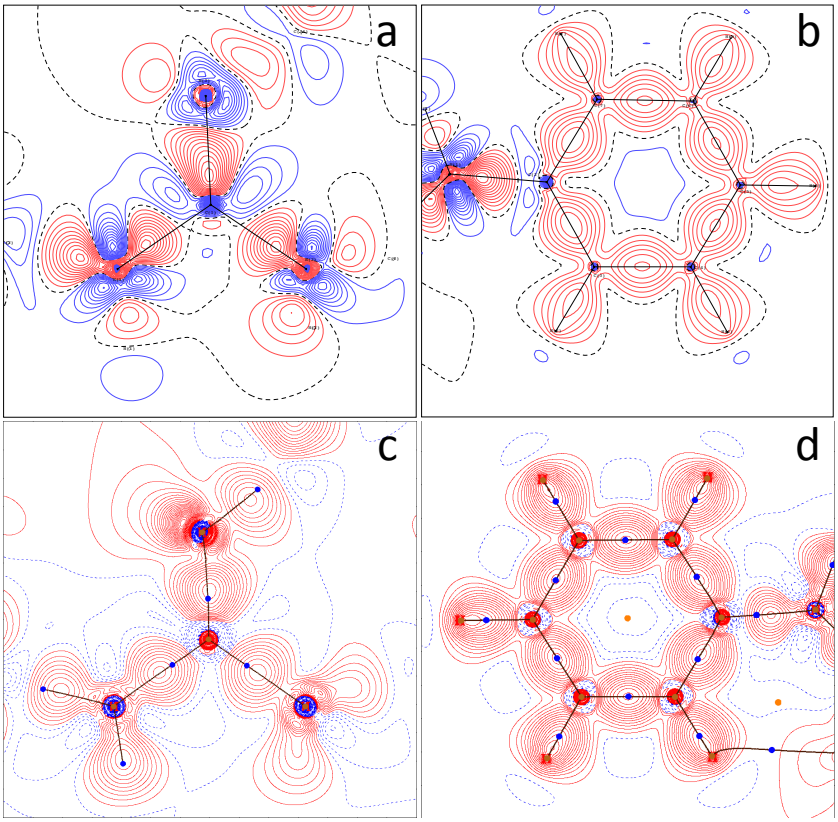

Figure 11.10: Contour plots of the static deformation density obtained from the multipole refinement for the guanidine (a)and phenyl fragments(b), respectively and the plots of the theoretical static deformation of the same fragments(c)and (d). The red and blue solid contours lines represent the positive and negative contours, respectively, and the black dashed contours represent the lines with zero residual density. Step width is $0.1e\text{Å}^{-3}$.

core to the regions of the interactions. In the multipole charge density of the guanidine fragment it is evident the trigonal symmetry in the regions with positive deformation density in the central C atom. Furthermore, the deformation density shows that the interaction with the N atom of the imine group is stronger than the interactions with the N atoms of the amino groups. The other important feature in the deformation density is that the bond $N-ipsoC$ shows a strong interaction, where the deformation closer to the N atom is strongly positive and closer to the C atom is slightly negative due to the electronegativity of the N atoms. In the phenyl fragment the multipole static deformation density shows a charge density

in the bonds between the C atoms of the ring, showing the delocalization of the electron density. In the figure 11.10 (d) there is one more critical point due to the Poincaré-Hopf theorem (see Eq. 3.10).

Comparing the theoretical and experimental deformation densities it is evident that the two results have the same behavior. However, the deformation density in the theoretical results is larger than the one in experimental results. This difference is justified by the optimization of the geometry correspondent to an ideal case (at a temperature of 0K) and so the density is more localized.

The static deformation density for the **tpgtfa** structure is obtained in the same way as performed for the **tpg** structure and is presented in Fig 11.11. In the guanidinium fragment of the **tpgtfa** the deformation around the C atom shows a trigonal symmetry and it is evident the similarity between the three $C-N$ bonds. The great difference between the fragment of the guanidine in the two structures is the substitution of the imine group in the **tpg** by an amino group in the **tpgtfa**. In the phenyl ring, the deformation is similar to the same **tpg** group, due to the great stability of this group and so the results show a great deformation density along the $C-C$ and $C-H$ bonds of the rings of the cation.

The carboxylate group shows the expected $mm2$ symmetry and the strong interaction in the bonds $C-O$ with high concentrations of deformation density along these bonds. Furthermore, we can also see the evidence of hydrogen bonds between carboxylate group of the anion and the guanidinium fragment of the cation with a slight charge concentration in the region between the ions in the theoretical results and the depletion in the same region of the experimental results. The deformation around the O atoms shows the characteristic lone-pair. In the anion the deformation of the $C-C$ bond shows a greater interaction between these atoms and this is justified by the charge transferred between the two electronegative groups of this anion. The comparison of the deformation density obtained with multipole refinement and the theoretical results show a good consistence and this proves the good description of the carboxylate group.

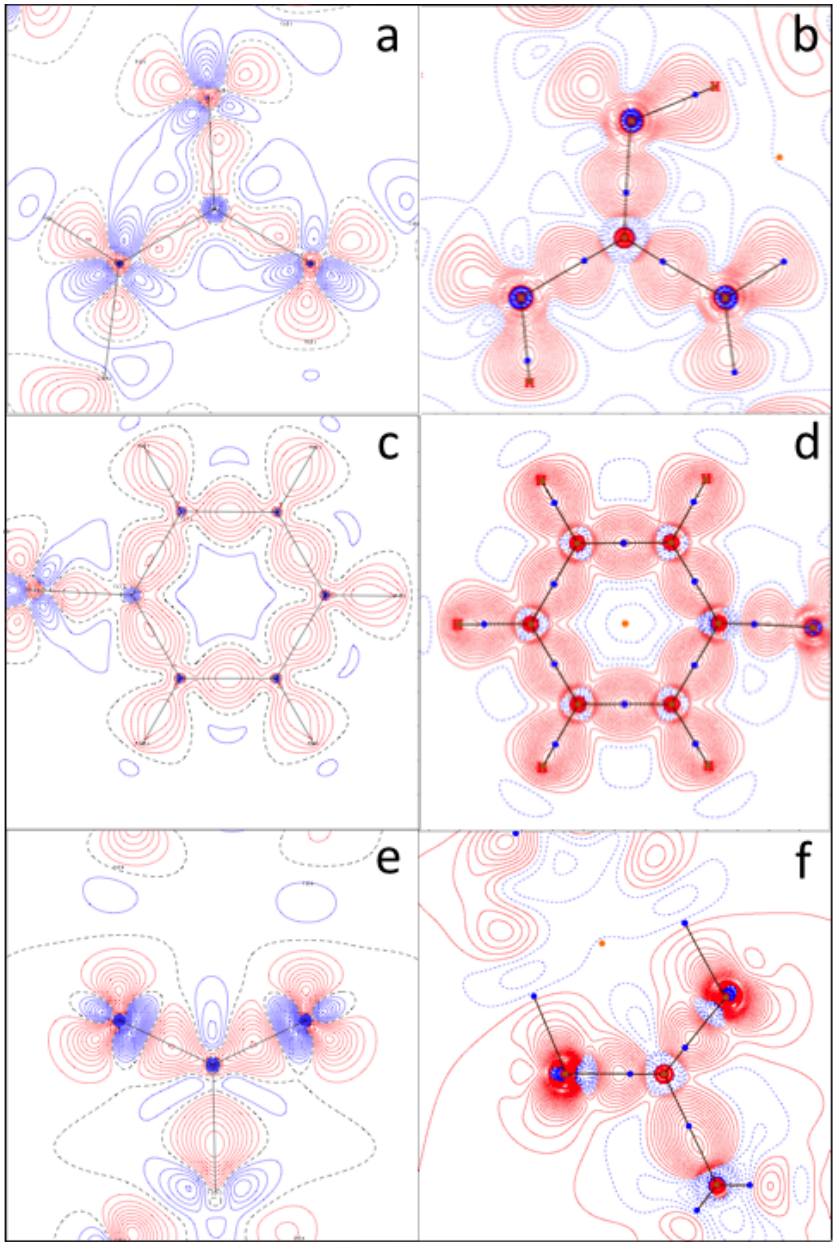

Figure 11.11: Experimental and theoretical contour plots of the static deformation density. In the (a) and (b) plots are presented the multipole and theoretical static deformation densities of the guanidine fragment, respectively and in the same way the (c) and (d) plots present the densities for a phenyl fragment and the (e) and (f) plots are for the carboxylate group. The red and blue solid contours lines represents the positive and negative contours respectively and the black dashed contours represent the lines with zero residual density. Stepwidth is $0.1e\text{Å}^{-3}$.

11.3.2 Electrostatic potential

The electrostatic potential is an important characteristic of molecular structures and explain the interactions between the molecules along crystals such as described in section 3.4.2. These properties of the structures can be determined from the charge density distribution of the **tpg** and **tpgtfa** that was obtained from the multipole refinement.

The atomic positions obtained from the multipole refinement are used for the calculation of the point distribution of the positive electrostatic potential and the electron density distribution is treated as a continuous distribution of negative charge. The results of the electrostatic potential of **tpg** are shown in a isosurface of the charge density, with the value of the electrostatic potential at each point on the surface color coded.

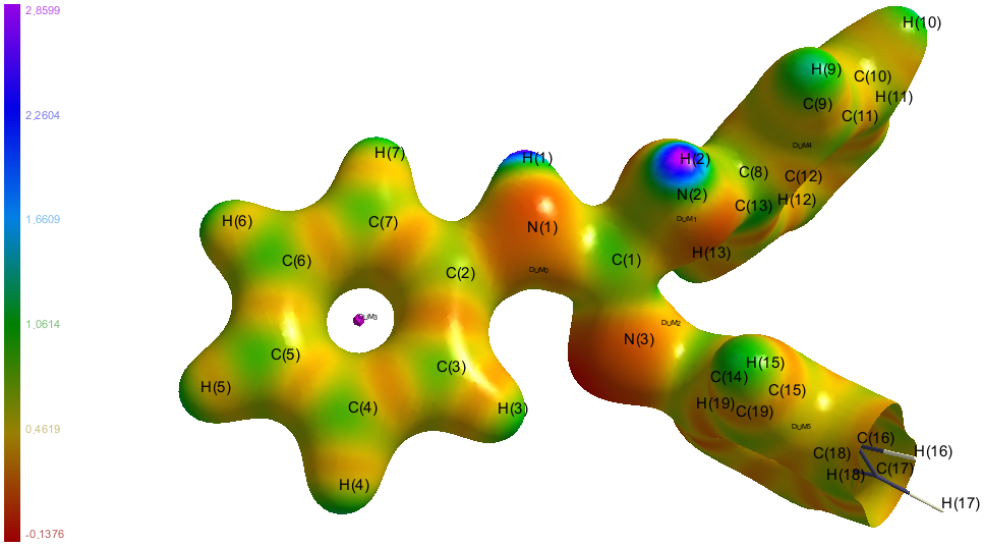

Figure 11.12: The isosurface of the **tpg** charge density at $0.5e\text{Å}^{-3}$, with the value of the electrostatic potential in $e\text{Å}^{-1}$ at each point on the surface color coded.

The isosurface shows that electrostatic potential is very low in all the rings, indicating that the two components of the electrostatic potential cancel each other out in the phenyl groups. However when we analyze the fragment of guanidine it is evident the great variation of the electrostatic potential along the isosurface. In the two amino groups $(-NH)$ in the hydrogen region it is obtained a value of $2.9e\text{Å}^{-1}$ which reveals that the electrostatic potential in this region is dominated

by the distribution of the positive charge associated to the nucleus. In contrast with this region, we see in the imine group (= N) a negative electrostatic potential of about $-0.13e\text{Å}^{-1}$. This shows a slight preponderance of potential electrostatic component associated to the electron density. These two regions with minimum and maximum of the electrostatic potential, will form chains along the crystal characteristic of this structure.

In the same manner the electrostatic potential of the **tpgtfa** is analyzed using the isosurface such as in **tpg** and the results of this treatment are presented in the Fig. 11.13.

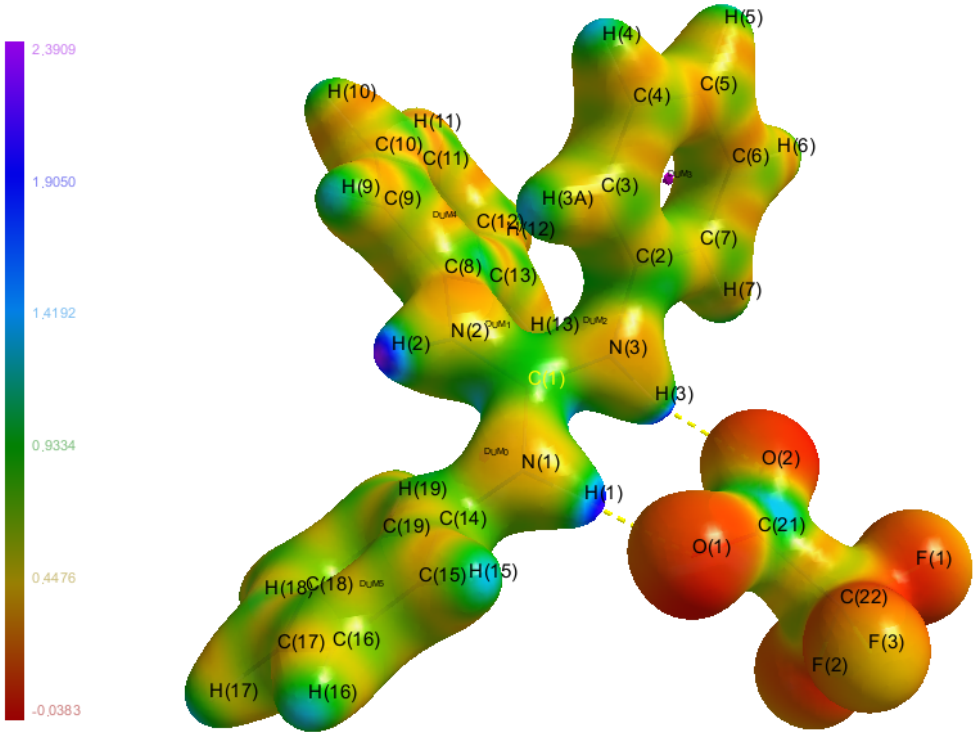

Figure 11.13: The isosurface of the **tpgtfa** charge density at $0.5e\text{Å}^{-3}$, with the value of the electrostatic potential in $e\text{Å}^{-1}$ at each point on the surface colour coded.

The triphenylguanidine molecule shows a similar behavior in **tpg** and **tpgtfa** with an important difference due to the protonation of the N3 atom in the **tpgtfa** structure. Thus, the triphenylguanidinium cation has three regions with negative electrostatic potential of about $2.4e\text{Å}^{-1}$ close to the H atoms of the guanidinium

fragment. In the trifluoroacetate anion the electrostatic potential is more interesting in the regions close to the O atoms. These two atoms participates in three hydrogen bonds with the triphenylguanidinium cation and have a positive electrostatic potential, but very close to zero.

The electrostatic potentials studied are important to understand the interactions between asymmetric units in each crystal and it is crucial in the stability of the crystal lattices. So the electrostatic interactions between asymmetry units described leads to the formation of chains in the two structures.

11.3.3 Laplacian of the charge density

The Laplacian of the charge density, shows the regions with concentration or depletion of the charge from the analysis of the sign of the Laplacian. This way, the regions with negative laplacian are related to concentration of the charge and for positive regions are associated to the depletion of charge. We will present the contour plots of the Laplacian of the charge density for principal fragments of this two structures. In the **tpg** we focused in the Laplacian of the guanidine fragment and phenyl groups obtained from the experimental and theoretical result presented in the Fig. 11.14.

These maps of the Laplacian of the guanidine fragment show regions of concentration of charge mainly in the bonding regions between atoms. Especially in the N atom of the imine group it is found a large region of charge concentration that allows to prove the existence of a non-bonding lone-pair that corresponds to a peak at the Laplacian function outside the core atom and usually defined as valence shell charge concentration (VSCC). The other VSCCs in this guanidine fragment are related to the bonds and in these cases the VSCC is observed close to each atom on the bonding vector. On the other hand, the more evident regions of the depletion of the charge density is around the core of atoms. These regions appear due to displacement of the charge density from the core of the atoms to the bonds between the atoms. The phenyl group shows again concentration regions along the bonds with VSCCs associated with the bonds and the regions of depletion around the cores of C atoms.

The analysis of all results presented in Fig 11.14 shows a good agreement with

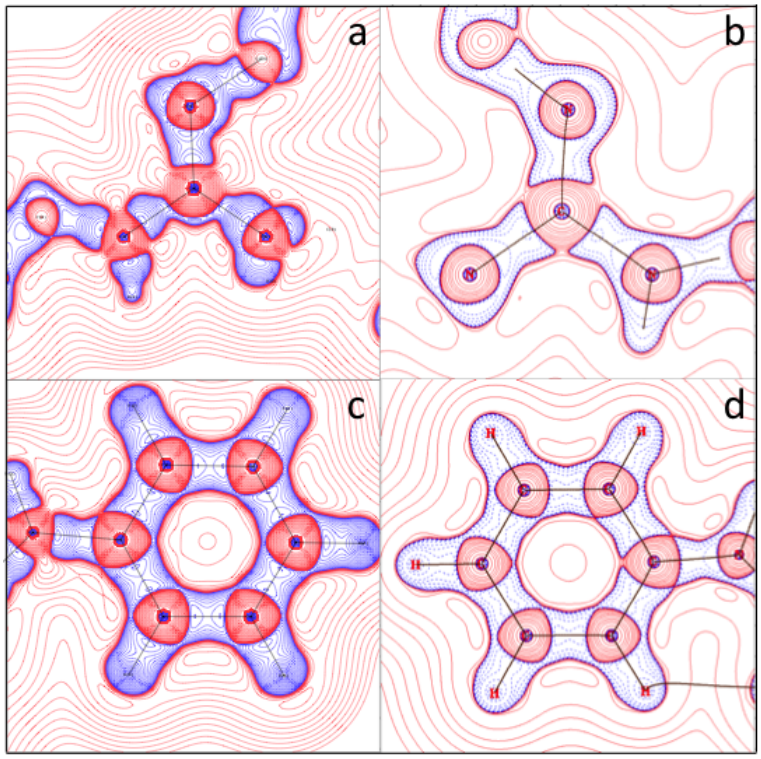

Figure 11.14: The contour plots of the Laplacian of the charge density of the **tpg** structure. The results for the guanidine fragment are presented in the (a) and (b) plots from multipole charge density and theoretical calculations, respectively. Similarly the results of the phenyl fragments are (c) and (d) plots from multipole charge density and theoretical calculations, respectively. The red and blue solid contours lines represents the depletion and concentration of the charge density and are represented with geometric progression.

experimental results obtained from the multipole refinement and with theoretical results obtained from optimized geometry.

The same treatment was applied in the **tpgtfa** structure and the results of the Laplacian of the charge density are presented in Fig.11.15. In all results obtained for **tpgtfa** it is verified the same charge density behavior with charge concentration regions along the bonds and depletion regions located around the atoms cores.

The guanidine fragment in this crystal presents a big difference compared to the same fragment in **tpg** due to the N atom being protonated in **tpgtfa** and

consequently the non-bonding lone-pair VSCC will form the bond with the extra H atom in this structure.

The Laplacian of the carboxylate group shows the existence of three VSCCs in the O atoms. One of them corresponds to a non-bonding lone-pair VSCC, the other is associated to the bond of O atoms with the C atom of the carboxylate group. The last VSCC of the two O atoms allows the formation of hydrogen bonds between triphenylguanidinium and trifluoroacetate ions. In the carboxylate group the experimental and theoretical plots of the Laplacian show a small difference over the hydrogen bonds.

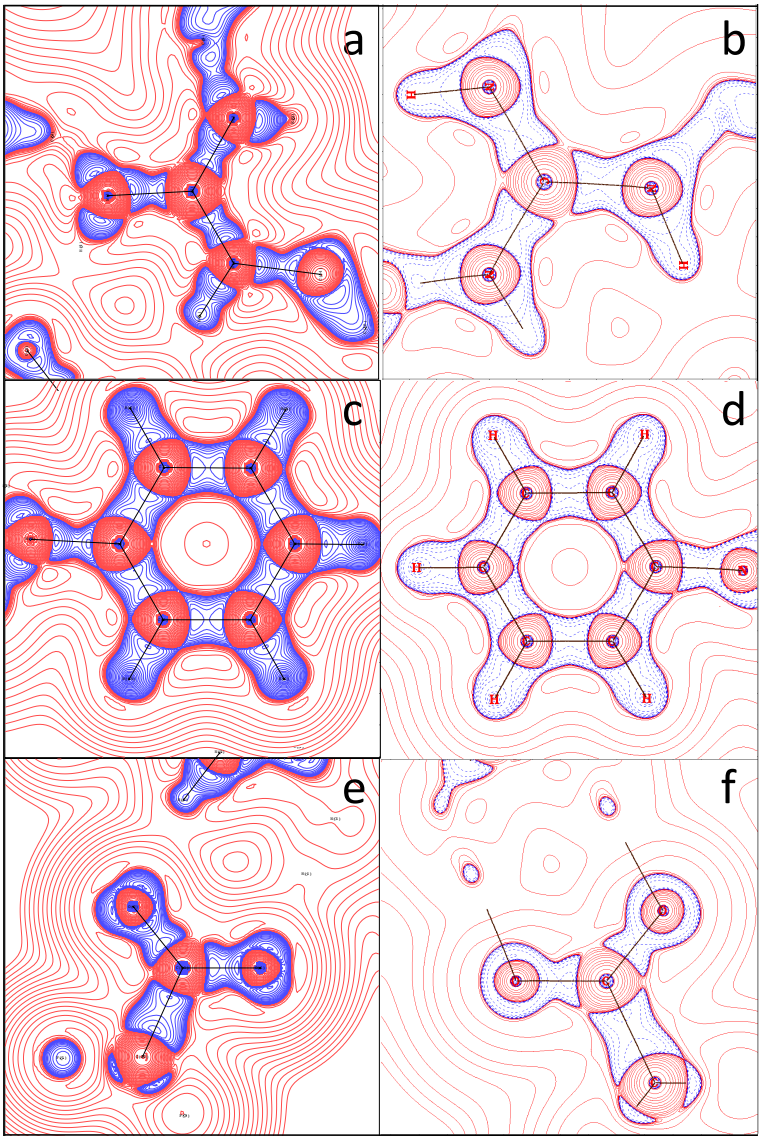

Figure 11.15: The contour plots of the Laplacian of the charge density of the **tpgtfa** structure. The results for the guanidinium fragment are presented in the (a) and (b) plots from multipole charge density and theoretical calculations, respectively. Similarly the results of the phenyl fragments are presented in the (c) and (d) plots and carboxylate group (e) and (f). The red and blue solid contours lines represents the depletion and concentration of the charge density and are represented with geometric progression.

In the middle of these hydrogen bonds, the experimental results show a very small depletion, but the theoretical plot for the same region shows a small VSCC, which indicates a concentration of charge between the two ions of the asymmetric unit of **tpgtfa**.

11.3.4 Topology of the charge density

The topology of the charge density distribution can only be performed with the determination of the atomic basins and allows us to obtain all the critical points (CP) and bond paths (BP). Such as explained in previous sections the CPs are determined from the expression 3.7, that depends on the gradient of the charge density, thus in this section it is important to study the gradient density plots.

The results of **tpg** are presented in Fig. 11.16 and shows the CPs of the charge density and the type of these. Furthermore these plots also allow us to visualize the atomic basins defined by the zero flux surfaces and BPs.

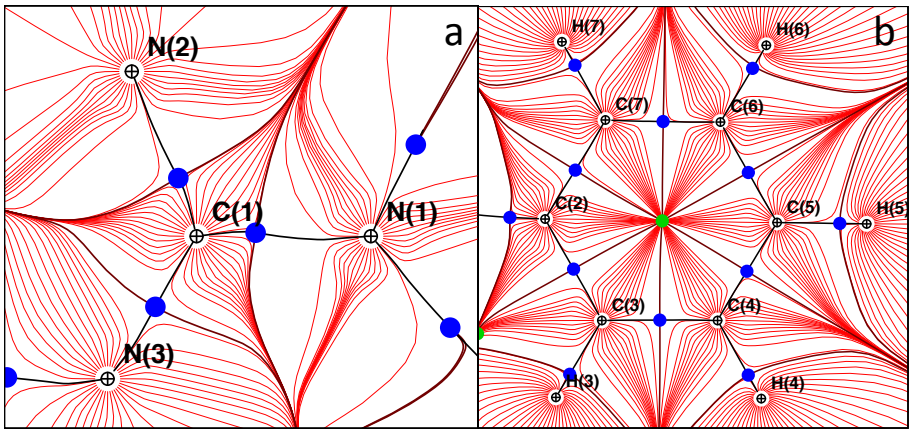

Figure 11.16: The plots of the gradient trajectories of the charge density for different fragments of the **tpg** structure. The result for the guanidine fragment is presented in the (a) plot and the result of the phenyl fragment is presented in the (b) plot. The red lines denote the gradient trajectories of the electron density, the bond paths and the lines of the zero flux surfaces in this plane are represented in black. The points flagged with a cross are the NCP, the blue points are the BPC, and the green points are the RCP.

The gradient trajectories of the charge density plots of the **tpg** show the set of trajectory lines within the atomic basin converging in the NCP such as explained

in section 3.5.2. This trajectory lines never cross and define the zero flux surface in this plane of atoms represented by a line. The zero flux line in these plots are intersected by the BP and in this intersection it is found the BCP.

In the guanidine fragment plot we can see the three BCP associated to the N−C bonds, however the difference between the atomic basins of the N atoms is pronounced, with a different distribution of the trajectory lines in the N3 basin. Besides, the basin of the central C atom has a triangular shape conditioned by the N atoms around, as it was predictable. The three phenyl group shows the same result in the plots of the gradient trajectories and it is easy to verify that all C atoms have very similar atomic basins generating a great symmetry with a very small difference in the C2 atom because this is bonded with a N atom instead of an H atom. In this group apart from the various BCP and BP, it is found an RCP that has been also determined in the center of the ring and that shows the local minimum of ρ in a phenyl plane and a maximum along the axis normal to this plane.

The gradient trajectory plots of the **tpgtfa** structure are performed in the same way and are presented in Fig 11.17.

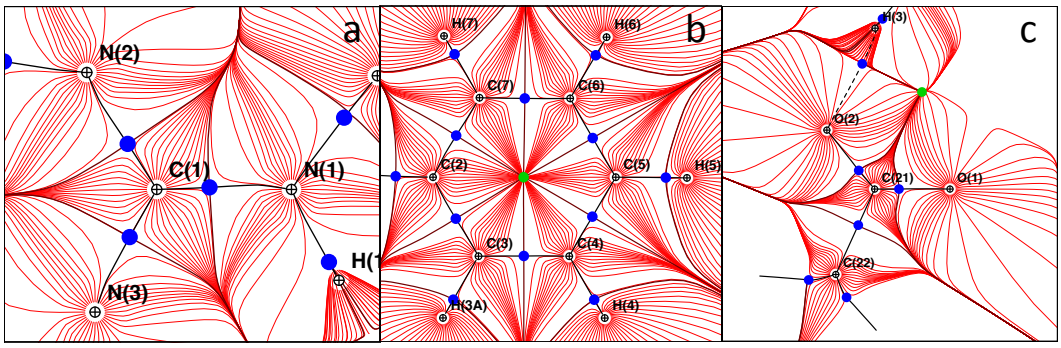

Figure 11.17: The plots of the gradient trajectories of the charge density for different fragments of the **tpgtfa** structure. The result for the guanidinium fragment is presented in the (a) plot, the results of the phenyl fragment is presented in (b) and the carboxylate group are in the (c) plot. The red lines denote the gradient trajectories of the electron density, the bond paths and the lines of the zero flux surfaces in this plane are presented in black. The points flagged with a cross are the NCP, the blue points are the BPC, and the green points are the RCP.

The guanidinium fragment in the **tpgtfa** shows a similar result to the obtained

in **tpg** with a difference between the N3 atoms in the two structures. In this structure the N3 atom shows the same distribution of the gradient trajectories as the other N atoms contrary to what happened in **tpg**. Thus, we can say that in **tpgtfa** the guanidinium fragment presents a real trigonal symmetry because in this structure the N3 atom is protonated. Comparing the results of the two structures it is obvious the similarity of the phenyl rings, displaying the same topological structures (same number of BCP and one RCP in the center of the ring).

The Fig. 11.17 (c) shows the gradient trajectories in the carboxylate group. The C21 atom has a small basin because this is strongly conditioned by the basins of the O atoms and C22 atom. On the other hand the O atoms presents large basins that are bonded with C22 atom. Furthermore, the O atoms also form hydrogen bonds between anion and cation, but in the plot the H3 atom has a strange behavior, this atom is not in the carboxylate group plan and likewise the H1 atom does not appear in this plot. Finally, between two hydrogen bonds there is a RCP. This critical point shows up due to the pseudo ring formed by two O−C bonds of the carboxylate group, the two N−C bonds of the guanidinium fragment and the hydrogen bond between molecules.

The study of the gradient allows to obtain the atomic basins, CP and BP, of the charge density structures. So we are now able to analyze in following sections the several properties of the charge density from this topological entities.

11.3.4.1 Discussion of the BCPs properties

In this section we discuss the properties of the BCPs in the structures and with this information we analyze the type of the bonds. The differences between the two compounds are analyzed mainly in the guanidine fragment that is similar in the two structures. Then we focus in the BCP associated to the several bonds between central C atom and the three N atoms of the guanidine fragment .

The results of the **tpg** show an important difference between the values of the N3−C1 bond. The bond path length of this bond is slightly shorter than the other two which may indicate a stronger bond. The results for these bonds in **tpg** gives a great difference in the $\rho(r_{BCP})$ with the similar values for bonds with

Table 11.8: The topological properties of the BCP of the main bond of the guanidine fragment of the two crystals studied. The distances $d(A-B)$, $d(A-BCP)$ and $d(BCP-B)$ are presented in Å, the charge density and Laplacian of the same are presented in eÅ^{-3} and eÅ^{-5}, respectively.

Bond	$d(A-B)$	$d(A-BCP)$	$d(BCP-B)$	$\rho(r_{BCP})$	$\nabla^2\rho(r_{BCP})$
			tpg		
N1−C1	1.3617	0.9000	0.4618	1.856	-1.933
N2−C1	1.3852	0.9089	0.4763	1.822	-4.444
N3−C1	1.3136	0.6746	0.6390	2.865	-30.408
			tpgtfa		
N1−C1	1.3253	0.8065	0.5187	2.072	-13.961
N2−C1	1.3415	0.8095	0.5320	2.023	-13.016
N3−C1	1.3527	0.8130	0.5397	1.994	-12.613

N1 and N2, but the value of the bond with N3 is larger than the other and this proves again that this bond is much stronger than the other two. Finally, the Laplacian of the charge density is negative in the three bonds which shows the concentration of charge in the BCP, however the values are substantially different and it is important to refer the large value of the bond N3−C1 which shows an higher charge concentration on this bond.

In the results of the **tpgtfa** it is evident the similarity between the values of all properties in the three BCP. The results show that the BCPs are closer to the central C atom. Besides, the values of the $\rho(r_{BCP})$ and $\nabla^2\rho(r_{BCP})$ shows great interaction between atoms and concentration of charge in the BCP. The comparison of the two structures show great differences and proves that different types of bonds are involved in the guanidine fragments. In the **tpg** this fragment is composed by two single bonds and one double bond, on the other hand the **tpgtfa** has three delocalized bonds with the same character.

The other fragment that can be compared between both structures are the phenyl rings analyzing the C atoms and taking into account their positions in the ring. These results are presented in the Table 11.9.

The results show concordance between all values proving the stability of these groups in the two structures.

The analysis of the positions of the BCP in the C−C bonds shows that they are at the same distance of two C atoms, maintaining these distances approximately

Table 11.9: The topological properties of the BCP of each C−C bonds of one phenyl ring of the two crystals studied. The distances $d(A-B)$, $d(A-BCP)$ and $d(BCP-B)$ are presented in Å, the charge density and Laplacian of the same are presented in eÅ^{-3} and eÅ^{-5}, respectively.

Bond	$d(A-B)$	$d(A-BCP)$	$d(BCP-B)$	$\rho(r_{BCP})$	$\nabla^2\rho(r_{BCP})$
			tpg		
C2−C3	1.4066	0.6975	0.7091	2.144	-21.226
C3−C4	1.3990	0.7011	0.6979	2.098	-19.824
C4−C5	1.3865	0.6929	0.6935	2.129	-20.791
C5−C6	1.3950	0.6977	0.6973	2.106	-20.140
C6−C7	1.3908	0.6936	0.6972	2.122	-20.455
C2−C7	1.4027	0.6955	0.7073	2.156	-21.500
			tpgtfa		
C2−C3	1.3860	0.7191	0.6670	2.101	-19.771
C3−C4	1.3814	0.6895	0.6919	2.105	-21.018
C4−C5	1.3933	0.6964	0.6969	2.078	-20.111
C5−C6	1.3842	0.6919	0.6923	2.103	-20.795
C6−C7	1.3802	0.6919	0.6882	2.109	-21.116
C2−C7	1.3996	0.7241	0.6755	2.065	-18.753

constant. The charge density in the BCP is approximately 2.1eÅ^{-3} and the Laplacian of the charge density around the $-20e$Å^{-5} is in agreement with charge density studies that include phenyl rings [20].

In the **tpgtfa** structure it is necessary to study the BCPs of the anion presented in the Table 11.10.

Table 11.10: The topological properties of the BCPs of the anion and the hydrogen bonds in the **tpgtfa** crystal. The distances $d(A-B)$, $d(A-BCP)$ and $d(BCP-B)$ are presented in Å, the charge density and Laplacian of the same are presented in eÅ^{-3} and eÅ^{-5}, respectively.

Bond	$d(A-B)$	$d(A-BCP)$	$d(BCP-B)$	$\rho(r_{BCP})$	$\nabla^2\rho(r_{BCP})$
O1−C21	1.2364	0.8371	0.3993	2.833	-14.803
O2−C21	1.2458	0.8437	0.4021	2.806	-17.447
C21−C22	1.5439	0.6526	0.8913	1.885	-22.397
O1$\cdots$H1	1.7179	1.1707	0.5472	0.221	4.419
O2$\cdots$H3	1.9001	1.2351	0.6651	0.171	2.904

The bond between the two C atoms shows a distance slightly greater than

expected, and it is verified further that the critical point is closest to the C21 atom which shows a shift of the charge to the carboxylate group. Furthermore, this BCP has a Laplacian more negative showing a large charge concentration.

The bonds of the carboxylate group have the same bond length and in both the BCP is nearest to the atom C21. But these two BCP show different results of the Laplacian and consequently the O2−C21 bond has a higher charge concentration. This result can be explained by the fact that O2 participates in two hydrogen bonds in the crystal structure.

The two hydrogen bonds between anion and cation have the same behavior with a much greater distance than all other bonds such as expected. Besides, in the BCP these bonds show a very low density and the Laplacian is low and positive which shows a depletion in this BCPs.

11.3.4.2 Bond path properties

Another important study is the analysis of the Laplacian and ellipticity along the bond paths. This study allows to compare the main bonds in each structure and also prove the similarities between the bonds shown in the previous section, obtained from the analysis of the BCPs.

The results obtained for the **tpg** structure from the multipole refinement are presented in Fig. 11.18 for different groups that make up the **tpg**.

The results obtained for the Laplacian in the guanidine fragment bonds show the complete concordance between bonds formed by N1 and N2 atoms with the central C atom. These two bonds show a great minimum in the N basin that indicates the charge concentration in this region of the bonds. The Laplacian of the bonds of N1 and N2 atoms with the C atoms of the rings shows the same profile as the above bonds. The bond formed by N3 atom with the central C atom shows a higher symmetry in the charge concentration with a minimum in the C basin. The other bond with N3 and C atom of the ring shows a similar profile with a deviation for the N basin and a lower charge concentration.

The ellipticity in the bonds of the guanidine fragments gives a measure of the distortion of the electron density from the cylindrical symmetry, σ in the BP. In the N basin it is obvious the existence of the peak in ellipticity in all bonds due

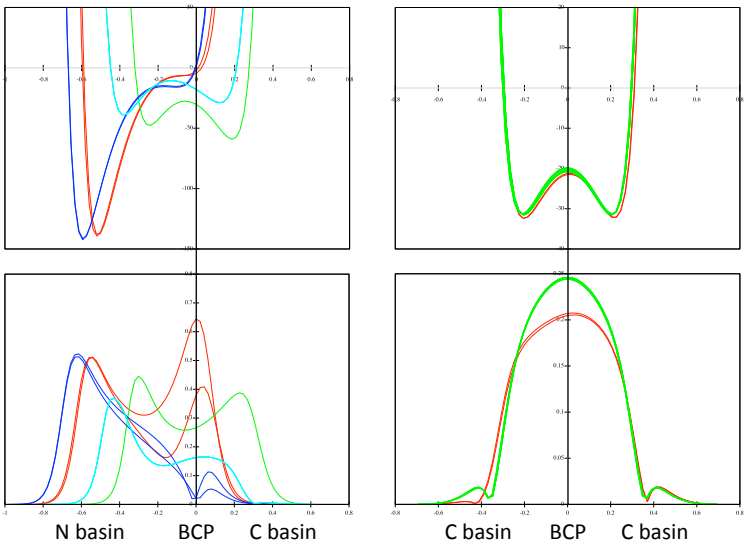

Figure 11.18: The properties along the BPs of the most interesting bonds of the **tpg** structure. On the top it is presented the Laplacian in $e\text{Å}^{-5}$ and bellow we have the ellipticity. The results along the BP in the guanidine fragment are presented on the left side where the bonds N1−C1 and N2−C1 are in red, the bond N3−C1 is in green, the bonds N1−C2 and N2−C8 are in blue and the bond N3−C14 is in light blue. The phenyl group is presented on the right side and the bonds C2−C3 and C2−C7 are in red and the other bonds between C atoms are in green.

to the transfer of electron density to the bond. However, the bonds N1−C1 and N2−C1 have a large ellipticity only in the N basin and in BCP, but in C basin the ellipticity decreases to very low values. This shows the distortion of charge density in the bonds close to the N atoms. For the bond N3−C1 the ellipticity has a large value around the BCP and this gives a proof of the π character of this bond. The bonds of N atoms with C ring atoms shows a lower value of the ellipticty in the BCP and in the C basin, with the exception of bond N3-C14 which has an ellipticity of the 0.16. The peak in N3 basin shows the transfer of lone-pair density to the bonds N3−C14 and N3−C1.

The phenyl group has a similar behavior over all the bonds, thus the Laplacian gives a large concentration of charge around the BCP, but the bonds with C ring atoms bonded with guanidine fragment have a lower value of ellipticity. However these results of the ellipticity in the phenyl ring demonstrate the well-

known π-character along the phenyl ring.

The same study is performed in the **tpgtfa** to complement the knowledge of this structure and to check for possible differences with the **tpg** structure. Thus, the results are presented in Fig. 11.19.

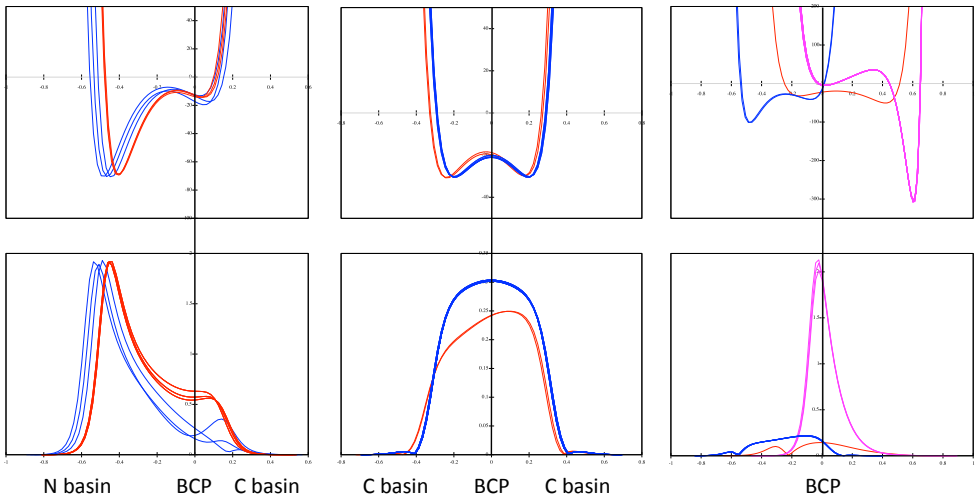

Figure 11.19: The properties along the BP of the most interesting bonds of the **tpgtfa** structure. On the top it is presented the Laplacian in eÅ^{-5} and bellow we have the ellipticity. The results along the BP in the guanidine fragment are presented on the left side where the bonds N1−C1, N2−C1 and N3−C1 are in red, the bonds N1−C14, N2−C8 and N3−C2 are in blue. The phenyl group is presented in middle and the bonds C2−C3 and C2−C7 are in red and the other bonds between C atoms are in blue. The anion is presented on the right side and the bonds O1−C21 are in blue, the bond between C atoms (C21−C22) is in red and the three bonds with C22 and F atoms are in pink.

The bonds with N atoms shows a great concordance in Laplacian with a minimum in the same region of the N basin which again indicates a large charge concentration. Furthermore the ellipticity of the same bonds shows in same region of the charge concentration a large value of ellipticity that decrease in the BCP, but for bonds with the central atom the ellipticity in the BCP is approximately 0.5 that indicates the large distortion of the electron density in the N basin and in BCP. In the phenyl rings it is verified the same profile that was obtained in **tpg** and this is because, as mentioned, these groups have a great stability only

disturbed in the C atom bonded with N atom of the guanidine.

The results for the anion shows in the bond with C atoms the large concentration of the charge around the BCP with a slight deviation to the C22 atom, besides the ellipticity of this bond shows one ellipticity always very close to zero. On the other hand the bonds between the C22 atom and F atoms shows a large concentration of the charge in the F basins such as expected because of their characteristics. The ellipticity of this three bonds has a large values and this is explained with a trigonal symmetry in C22 atom and the electronic repulsion between this regions of charge concentration and F atoms. The other important group is the carboxylic that shows the same profile of the Laplacian along the C−O bonds with a high charge concentration on the O basins such as expected in this bonds. In the ellipticity the result along the BP shows a distortion on the O basins because the transfer of electron density from the characteristic lone-pair to this bonds.

The anion and cation are linked by hydrogen bonds between O atoms of the carboxylic group and the two N atoms of the guanidine fragment. The properties of these two hydrogen bonds are presented in Fig. 11.20.

In the O basins of the hydrogen bonds it is verified the great charge concentration and large ellipticity. This indicates a distortion of the electron density of the O atoms. Around the BCP the Laplacian is close to 0 and the ellipticity is very low. In the H basins it is verified a large charge concentration of charge because the H atoms, however in the ellipticity are evident the differences. In bond O1$\cdots$H1 the ellipticity is almost zero and constant, but the bond O2$\cdots$H3 has a great peak and this shows a large distortion in the bond. This difference is explained by analyzing the planes formed by the O atoms and each N atom bonded to H atom. So, in the plan defined by O1, O2 and N1 the H1 is contained in that plan, therefore the ellipticity is almost zero. But in the plan formed by O1, O2 and N3 the H3 is out of this plan and consequently the ellipticity shows a large peak because the distortion of the electron density.

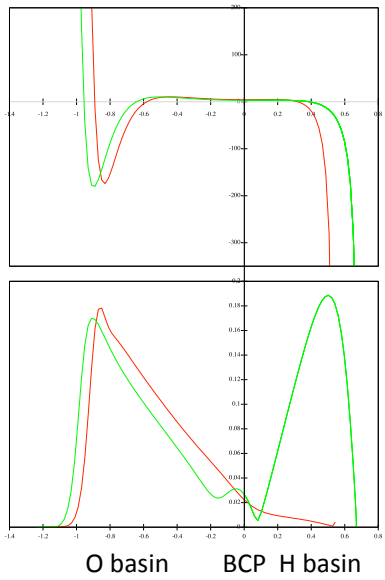

Figure 11.20: The properties along the BP of the hydrogen bonds between triphenylguanidinium cation and trifluoroacetate anion. On the top it is presented the Laplacian in $e\text{Å}^{-5}$ and bellow we have the ellipticity along the BPs. The hydrogen bond O1$\cdots$H1 are in red and the O2$\cdots$H3 are in green.

11.3.5 Net charges and higher moments

The net charges from the integration over the topological basins in the two compounds are presented in Table 11.11.

In **tpg** the N atoms in the guanidine fragments always have negative charges, which is in agreement to what is expected for electronegative atoms. The scrutiny of the values obtained from the integration of basins shows that in **tpg** all atoms have values very close, between -1.2428 and -1.4099au, but in **tpgtfa** the N atoms of the amino group have a greater charge than the N atoms of **tpg** and the N atom of the imine group presents the lowest charge of all the N atoms in this two structures.

The central C atom has positive charge because the N atoms introduces a polarization in C atom. In the same way the C atoms of the rings linked to the guanidine fragment(C2, C8 and C13) presents positive charge, but this is considerably lower than the central C.

The rings in these structures show a great coherence between themselves, in

Table 11.11: Charges from the integration over the atomic basins in **tpg** and **tpgtfa**

Atom	Charge(au)	Atom	Charge(au)
tpg		**tpgtfa**	
C(1)	1.4324	C(1)	1.4205
N(1)	-1.9423	N(1)	-1.2956
N(2)	-1.8391	N(2)	-1.4099
N(3)	-1.0082	N(3)	-1.2428
C(2)	0.7019	C(2)	0.3965
C(3)	-0.2042	C(3)	-0.1570
C(4)	-0.1286	C(4)	-0.2544
C(5)	-0.1295	C(5)	-0.2520
C(6)	-0.1291	C(6)	-0.2500
C(7)	-0.2068	C(7)	-0.1626
–	–	O(1)	-1.4240
–	–	O(2)	-1.4205
–	–	C(21)	2.5632
–	–	C(22)	1.1884

the first carbons of the rings the charge is positive as would be expected, and all other C atoms exhibit a negative charge. Making a more detailed analysis of the value of the charges along the ring it is possible to find a trend showing the charge of the C atoms becoming increasingly more negative with the increase of the distance to the atom N such as is showed in Fig 11.21. The only ring that does not have this behavior is the ring connected to the N1 atom that has the higher negative charge of all N atoms.

In the anion of the **tpgtfa** the charges are dominated by electronegative atoms and in Table 11.11 it is showed the negative charge of the O atoms of the carboxylate group, having approximately the same charge. The three F atoms also have negative charge with an average value of -0.541au. Consequently, the C atoms between these two negative groups have positive charge. The polarization introduced by the electronegativity of the O atoms polarize the C atom of the carboxylate group withdrawing electrons from it's basin, leading to a large positive charge of 2.5632 for this carbon atom.

Finally the H atoms can be divided in two groups, the H atoms of the guanidine fragments in the two molecules that have an average charge of the 0.7025au

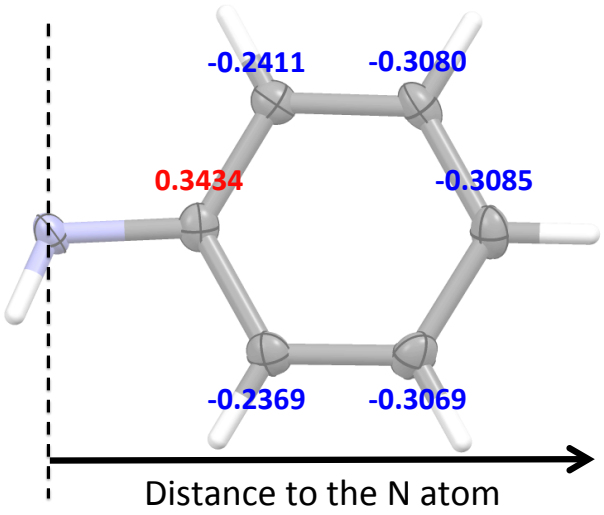

Figure 11.21: The charge of the C atoms of the ring in atomic units with the distance to the atom N.

and the H atoms of the rings that shows lower values of charge with an average charge of the 0.2042au.

Chapter 12

Conclusions

This thesis shows several results of the nonlinear optical experimental and computational studies applied to various new compounds with high octupolar character such as guanidine derivatives and thiocyanuric acid. The characterization of the structures was performed using single crystal X-ray diffraction; the nonlinear optical response was evaluated using the Kurtz-Perry method and several computational methods.

Structural determination and the respective study of six new guanidine salts was aclomplished. Two new structures of guanidine salts, that crystallize in a noncentrosymmetric group, were found. These two crystals were evaluated with the Kurtz-Perry method showing SHG reasonable results. Interestingly, although the computational results are usually higher than the experimental values, we calculate for **g5** a smaller value than the value obtained experimentally, which indicates that some effects in this structure were discarded in computational calculations.On the other hand the computational result of the **g6** is approximately double the experimental value(as it is usual).

In this work, it was demonstrated the loss of much of the octupolar character of the phenylguanidine in relation to guanidine molecule. Two phenylguanidine salts were studied (one with structural determination). The nonlinear optical responses were measured showing that the SHG efficiency for these compounds is null.

The third guanidine derivative used was triphenylguanidine that exibits a large octupolar character (such as guanidine). The Kurtz-Perry method was used for

study of its nonlinear optical properties. This study reveals a modest result for the SHG efficiency that is in concordance with the computational results.

In all computational results it was verified a concordance in the behavior of the highest components of the hiperpolarizability, increasing to unrealistic values when functionals with less exchange of HF. This behavior allows us to conclude that the description of the electron density along the calculations with less exchange of HF leads to bad computational results. The SHG efficiency was calculated for each material using two different local field corrections. The anisotropic Lorenz-Lorentz local field factors in all structures presents substantially worse results than those obtained with approach by Wortmann and Bishop (extension of the Onsager's reaction field model). Finally all computational results of the SHG efficiency, with exception of the **g5**, are larger than those obtained experimentally. The possible justification for this discrepancy can be the low crystallinity of some materials and the losses of beam intensity in the experimental set up.

This work also focused on the comprehension of the charge density due to its strong influence in the nonlinear optical response. For the study of the TPG and TPGTFA structures it was applied the multipole refinement to experimental data. The results obtained show a good description of the charge density when are compared with theoretical results of the deformation and laplacian of the density (and when analyzed the results of the residual density).

The results of the properties of the charge density and the topology analyses were used for comparison of the triphenylguanidine molecule and triphenylguanidinium cation in the two structures. In these structures there is a large similarity in all properties of the charge density in the rings groups, on the other hand the most of the differences are associated to the guanidine fragment. The properties obtained show a different interaction between atoms in guanidine fragment with protonation of the one N atom in TPGTFA and in this conformation the three N atoms has the same type of properties. The equivalent atom in TPG is deprotonated and the properties are differ completely of all other N atoms presenting a electrostatic potential with a positive sign while the others have a negative electrostatic potential. Furthermore the Laplacian of the two guanidine fragments shows different regions of the concentration and depletion of charge around equiv-

alent N atoms. The topological analyses proves that these differences between these fragments are related with the N3−C1 bond of the TPG. This bond shows a high π character (a double bond) as seen in BCP and BP properties. On the other hand the results in the TPGTFA show that all N−C bond are single bonds with a large delocalization in the guanidine fragment.

Finally in the trifluoroacetate anion the study focused on the carboxylic group and it was checked that the two O atoms have the same properties. This was verified from analysis of BCP, BP and charge values obtained from the integration of the each atom along atomic basins. It was further reinforced by the fact the length of C−O bonds are practically the same in the anion.

In coclusion, this dissertation allowed me to obtain and develop scientific knowledge in the Nonlinear Optic and Charge density studies. Furthermore it gave me the possibility of understand and apply several experimental techniques and data treatments such as single crystal X-ray diffraction and consequent determination of the crystal structures, Kurtz-Perry method and subsequent analysis necessary to obtain the nonlinear optical response. Furthermore this work gave me a large set of computational skills with use of several programs such as GAMESS (US), Mathematica®, SHELXS- 97 and SHELXL-97 mainly in the determination of the structure and nonlinear optical properties. The multipole refinement and charge density analyzes made use of the XD program and Multiwfn version 3.3.7, besides other already mentioned. This work has great importance in my formation and search for knowledge to better understand the world around us.

Bibliography

[1] W. Humphrey, A. Dalke, and K. Schulten. *J. Mol. Graph.*, 14:33–38, 1996. xv, 81

[2] D. S. Chemla and J. Zyss, editors. *Nonlinear Optical Properties of Organic Molecules and Crystals*, volume 1. Academic Press, Orlando, FL, 1987. 1, 2

[3] J. Zyss. *J. Chem. Phys.*, 98:6583, 1993. 2, 19, 21

[4] V. Le Floc'h, S. Brasselet, J. Zyss, J.-F. Roch, B. R. Cho, S. H. Lee, S. J. Jeon, M. Cho, K. S. Min, and M. P. Suh. *Adv. Mater.*, 17:196, 2005. 2

[5] R. F. W. Bader, editor. *Atoms in Molecules: a Quantum Theory.*, volume 1. Oxford: Clarendon Press, Oxford Science Publications, 2007. 5, 27, 34

[6] J. Kerr. *Phil. Mag.*, 50:337, 1875. 7

[7] P. A. Franken, A. E. Hill, C. W. Peters, and G. Weinreich. *Phys. Rev. Lett.*, 7:118, 1961. 7

[8] T. H. Maiman. *Nature*, 187:493, 1960. 7

[9] P. N. Butcher. *Nonlinear Optical Phenomena.* Ohio State University, 1965. 16

[10] R. W. Boyd. *Nonlinear Optics.* Academic Press, Burlington, MA, third edition, 2008. 16

[11] J.E. Midwinter F. Zernike. *Applied Nonlinear Optics.* Wiley, New York, 1973. 16

[12] Mark G. Kuzyk. *Phys. Rev. Lett.*, 85:1218–1221, 2000. 18

[13] J. L. Oudar and D. S. Chemla. *J. Chem. Phys.*, 66:2664, 1977. 19

[14] J. Zyss. *Nonl. Opt.*, 1:3, 1991. 19

[15] J. L. Brédas, F. Meyers, B. M. Pierce, and J. Zyss. *J. Am. Chem. Soc.*, 114:4928, 1992. 19

[16] M. Joffre, D. Yaron, J. Silbey, and J. Zyss. *J. Chem. Phys.*, 97:5607, 1992. 19

[17] W. H. Bragg and W. L. Bragg. *Proc. R. Soc. Lond.*, A88:428, 1913. 23

[18] P. Debye. *Ann. Phys.*, 46:809, 1915. 23

[19] P. Coppens, editor. *X-Ray Charge Densities and Chemical Bonding*. Oxford University Press, Oxford and New York, 1997. 34

[20] Tibor S. Koritsanszky and Philip Coppens. *Chem. Rev.*, 101:1583–1627, 2001. 34, 128

[21] G. M. Sheldrick. *Acta Crystallogr. Sect. A*, 64:112, 2008. 42, 75, 83, 105

[22] S. K. Kurtz and T. T. Perry. *J. Appl. Phys.*, 39:3798, 1968. 42, 73

[23] J. F. Nicoud and R. J. Twieg. *Nonlinear Optical Properties of Organic Molecules and Crystals*, volume 2, page 251. Academic Press, Orlando, FL, 1987. 42

[24] R. F. Stewart. *J. Chem. Phys..*, 51:4569, 1915. 45

[25] N.K. Hansen and P. Coppens. *Acta Crystallogr*, A34:909, 1978. 45

[26] E. Clementi and D. L. Raimondi. *J. Chem. Phys.*, 38:2686, 1963. 50

[27] P. Hohenberg and W. Kohn. *Phys. Rev.*, 136:B864, 1964. 54

[28] W. Kohn and L. J. Sham. *Phys. Rev.*, 140:A1133, 1965. 54

[29] M. W. Schmidt, K. K. Baldridge, J. A. Boatz, S. T. Elbert, M. S. Gordon, J. H. Jensen, S. Koseki, N. Matsunaga, K. A. Nguyen, S. Su, T. L. Windus, M. Dupuis, and J. A. Montgomery. *J. Comput. Chem.*, 14:1347, 1993. 56

[30] J. Zyss and J. L. Oudar. *Phys. Rev. A*, 26:2028, 1982. 56

[31] R. Wortmann and D. M. Bishop. *J. Chem. Phys.*, 108:1001, 1998. 57

[32] L. Onsager. *J. Am. Chem. Soc.*, 58:1486, 1936. 57

[33] P. S. P. Silva, C. Cardoso, M. R. Silva, J. A. Paixão, A. M. Beja, M. H. Garcia, and N. Lopes. *J. Phys. Chem. A*, 114:2607, 2010. 58

[34] J. Zyss, J. Pécaut, J. P. Levy, and R. Masse. *Acta Crystallogr., Sect. B*, 49:334, 1993. 59

[35] M. M. Najafpour, M. Hołyńska, and T. Lis. *Acta Crystallogr., Sect. E*, 63:o3727, 2007. 59

[36] P. S. Pereira Silva, M. Ramos Silva, J. A. Paixão, and A. Matos Beja. *Acta Crystallographica E*, 63:o2783, 2007. 59

[37] G. Smith and U. D. Wermuth. *Acta Crystallogr., Sect. E*, 66:o1946, 2010. 59

[38] V. Parthasarathi, S. Wolfrum, J. H. Noordik, P. T. Beurskens, C. H. L. Kennard, G. Smith, and E. J. O'Reilly. *Cryst. Struct. Commun.*, 11:1519, 1982. 59

[39] P. S. Pereira Silva, M. Ramos Silva, J. A. Paixão, and A. Matos Beja. *Acta Crystallographica E*, 66:o524, 2010. 59

[40] D. S. Schonland. *Molecular Symmetry.* D. Van Nostrand Company LTD, London, UK, 1965. 60, 91

[41] F. H. Allen, O. Kennard, D. G. Watson, L. Brammer, A. G. Orpen, and R. Taylor. *J. Chem. Soc. Perkin Trans. 2*, page S1, 1987. 67

[42] M. C. Etter. *Acc. Chem. Res.*, 23:120, 1990. 68

[43] Pedro S. Pereira Silva and Hasnaa El Ouazzani. *Chemical Physics*, 428:67–74, 2014. 73

[44] A. L. Spek. *APEX2 and SAINT*. Bruker AXS Inc., Madison, Wisconsin,USA, 2003. 75, 83

[45] M.W. Schmidt, K.K. Baldridge, J.A. Boatz, M.S. Gordon S.T. Elbert, J.H. Jensen, S. Koseki, N. Matsunaga, K.A. Nguyen, T.L. Windus S. Su, and J.A. Montgomery M. Dupuis. *J. Comput. Chem*, 14:1347, 1993. 78, 114

[46] A.D. Becke. *Phys. Rev. A*, 38:3098, 1988. 78

[47] R.G. Parr C. Lee, W. Yang. *Phys. Rev. B*, 37:785, 1988. 78

[48] A.D. Becke. *J. Chem. Phys.*, 98:5648, 1993. 78

[49] A.D. Becke. *J. Chem. Phys.*, 98:1372, 1993. 78

[50] T. Kolev, R. Stahl, H. Preut, P. Bleckmann, and V. Radomirska. *Z. Kristallogr. New Cryst. Struct.*, 212:415, 1997. 79

[51] T. Kolev, T. Todorov, and R. Petrova. *Acta Crystallogr., Sect. E*, 58:o111, 2002. 79

[52] P. S. Pereira da Silva. *Structural, Ab initio and Nonlinear Optical Studies of Compounds with Octupolar Molecules*. PhD thesis, Universidade de Coimbra, Coimbra, 2012. 81, 86

[53] P. S. Pereira Silva, J. A. Paixão, M. Ramos Silva, and A. Matos Beja. *Acta Crystallographica E*, 62:o3073, 2006. 86

[54] P. S. Pereira Silva, C. Cardoso, M. Ramos Silva, and J. A. Paixão. *Acta Crystallographica E*, 63:o501, 2007. 86

[55] P. S. Pereira Silva, M. Ramos Silva, J. A. Paixão, and A. Matos Beja. *Acta Crystallographica E*, 63:o2243, 2007. 86

[56] P. S. Pereira Silva, M. Ramos Silva, J. A. Paixão, and A. Matos Beja. *Acta Crystallographica E*, 63:o2524, 2007. 86

[57] J. A. Krause, P. W. Baures, and D. S. Eggleston. *Acta Crystallogr. Sect. B*, 47:506, 1991. 93

[58] IUPAC-IUB Commission on Biochemical Nomenclature. *J. Mol. Biol.*, 52:1, 1970. 93

[59] M. K. T. Tin, N. Thirupathi, G. P. A. Yap, and D. S. Richeson. *J. Chem. Soc., Dalton Trans.*, page 2947, 1999. 99

[60] A. A. Kemme, M. A. Rutkis, and J. A. Adus. *Izv. Akad. Nauk. Latw. SSR: Sec. Chem. 5*, page 595, 1988. 99

[61] P.S. Pereira Silva, C. Cardoso, M. Ramos Silva, J.A. Paixão, A. Matos Beja, and F. Nogueira. *Journal of Molecular Structure*, 888:92, 2008. 99, 100

[62] C. Cardoso, P.S. Pereira Silva, M. Ramos Silva, A. Matos Beja, J.A. Paixão, F. Nogueira, and A.J.F.N. Sobral. *Journal of Molecular Structure*, 878:169, 2008. 100

[63] P.S. Pereira Silva, M. Ramos Silva, J.A. Paixão, and A. Matos Beja. *Acta Crystallographica Section E*, 63:o2524–o2526, 2007. 100

[64] P.S. Pereira Silva, J.A. Paixão, M. Ramos Silva, and A. Matos Beja. *Acta Crystallographica Section E*, 62:o3073–o3075, 2006. 100

[65] P.S. Pereira Silva, M. Ramos Silva, J.A. Paixão, and A. Matos Beja. *Acta Crystallographica Section E*, 63:o2243–o2245, 2007. 100

[66] P.S. Pereira Silva, Sérgio R. Domingos, M. Ramos Silva, J.A. Paixão, and A. Matos Beja. *Acta Crystallographica Section E*, 64:o1082–o1083, 2008. 100

[67] P.S. Pereira Silva, C. Cardoso, M. Ramos Silva, and J.A. Paixao. *Acta Crystallographica Section E*, 63:501–503, 2007. 100, 103

[68] J. J. McKinnon, M. A. Spackman, and A. S. Mitchell. *Acta Crystallogr., Sect. B*, 60:627, 2004. 101

[69] M. A. Spackman and D. Jayatilaka. *CrystEngComm.*, 11:19, 2009. 101

[70] M. A. Spackman and P. G. Byrom. *Chem. Phys. Lett.*, 267:215, 1997. 102

[71] J. J. McKinnon, A. S. Mitchell, and M. A. Spackman. *Chem.-Eur. J.*, 4:2136, 1998. 102

[72] S. K. Wolff, D. J. Grimwood, J. J. McKinnon, D. Jayatilaka, and M. A. Spackman. *CrystalExplorer 2.1.* University of Western Australia, Perth, Australia, 2007. 102

[73] T. Koritsanszky, P. Macchi, C. Gatti, L. Farrugia, P. R. Mallison, A. Volkov, and T. Richter, editors. *XD2006: A computer program package for multipole re- finement and analysis of charge densities from diffraction data.* 2006. 107

[74] Anatoliy Volkov, Yuriy A. Abramov, and Philip Coppens. *Acta Crystallogr., Sect. A*, 57:272–282, 2001. 109

[75] TIan Lu and Feiwu Chen. *J. Comp. Chem.*, 33:580–592, 2012. 114

[76] TIan Lu and Feiwu Chen. *J. Mol. Graph. Model.*, 38:314–323, 2012. 114